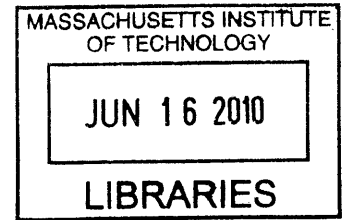# Hybrid Bio-templated Catalysts

by

Brian Neltner

B.S. Physics
B.S. Materials Science and Engineering
Massachusetts Institute of Technology, 2005

Submitted to the Department of Materials Science and Engineering
in partial fulfillment of the requirements for the degree of

Doctor of Philosophy in Materials Science and Engineering

at the

ARCHIVES

MASSACHUSETTS INSTITUTE OF TECHNOLOGY

June 2010

© Massachusetts Institute of Technology 2010. All rights reserved.

Author ....
Department of Materials Science and Engineering
March 18, 2010

Certified by...
Angela Belcher
Germeshausen Professor of Materials Science
and Engineering and Biological Engineering
Thesis Supervisor

Accepted by ....
Christine Ortiz
Chair, Departmental Committee on Graduate Students

Hybrid Bio-templated Catalysts

by

Brian Neltner

Submitted to the Department of Materials Science and Engineering
on March 18, 2010, in partial fulfillment of the
requirements for the degree of
Doctor of Philosophy in Materials Science and Engineering

Abstract

For decades, ethanol has been in use as a fuel for the storage of solar energy in an energy-dense, liquid form. Over the last decade the ability to reform ethanol into hydrogen gas suitable for fuel cell use has drawn interest as a way to increase the efficiency of both vehicles and standalone power generators. In this work, the M13 virus has been used as a biological scaffold and template to form hybrid Rh-Ni@CeO_2 nanowires. These composite materials have exceptionally high thermal stability, showing a greater than 8th order growth when made as isolated nanoparticles, and over 20th order growth when assembled into nanowires, compared to the expected 2nd-3rd order behavior.

The individual CeO_2 nanoparticles forming the wires are the smallest synthesized to date (1.3 nm), and over 20% of all oxygen sites were shown to be vacant, suggesting a very fast oxygen diffusion rate and highly active redox support enhancement. A chemical reactor was built to test the activity of the hybrid Rh-Ni@CeO_2 nanowires for the catalysis of ethanol into hydrogen gas in comparison to equivalent nanoparticle samples. Both nanowire and nanoparticle catalysts formed using these techniques showed excellent performance at only 300°C, and nanowires showed significantly improved resistance to deactivation over time on-stream. This study suggests that the use of biotemplating in the production of catalysts is a promising route to significant gains over traditional catalyst manufacture methods.

Thesis Supervisor: Angela Belcher
Title: Germeshausen Professor of Materials Science
and Engineering and Biological Engineering

Acknowledgments

With great thanks to:

- Angela Belcher

- Francesco Stellaci

- Steven Leeb

- Tom Neltner

- Janet Fox

- Steven Neltner

- Alex Xu

- Brian Peddie

- Will Doenlen

- Keith Durand

- Mark Allen

- Andrew Magyar

- Scott Speakman

- Anthony Garratt-Reed

- Dong Soo Yun

- Jennifer Hsieh

- David Gray

- Debadyuti Ghosh

- Andrew Peterson

- Jeremy Mason

- Chris Schuh

- Juan Holgado

Contents

List of Figures

13

14

18

List of Tables

Chapter 1

Introduction

Hydrogen fuel cells generate power by chemically converting hydrogen and oxygen into water. This process does not produce power through the use of a heat engine, so the maximum efficiency can exceed that of a Carnot heat engine. [5] Although hydrogen has a mass energy density of 141.8 MJ/kg, the volumetric energy density is only 0.0116 kJ/mL for uncompressed hydrogen, and only 11.4 kJ/mL for hydrogen compressed to 100 MPa (not including the weight and volume of the tank required to maintain such a high pressure). By comparison, ethanol has an energy density of 29.7 MJ/kg, but has a volumetric energy density of 23.4 kJ/mL at atmospheric pressure. [6] By catalytically reforming ethanol into hydrogen gas, the benefits of having a high energy density fuel can be combined with the benefits of using hydrogen fuel cells to produce energy more efficiently, resulting in a significantly more practical way to incorporate fuel cells into existing systems.

The catalytic oxidative steam reforming of ethanol-water mixtures saw a major breakthrough in 2004, when the complete conversion of ethanol over rhodium-ceria ($Rh@CeO_2$) catalysts was observed at 650°C. [1] Since then, the conversion of ethanol into hydrogen gas over ceria (CeO_2) has been widely investigated, and makes a good prototypical reaction to study the effects of biotemplating on catalytic performance. [1,2,7–26]

If the hydrogen produced over such catalysts has a low concentration of carbon monoxide, it can be used in fuel cells. Further, if the catalysts can be made to operate at low temperature and for a long period of time without degradation, it offers an opportunity for substantial advances in the portability and flexibility of fuel cells. The use of a CeO_2 catalyst supporting rhodium and nickel metal can be used to efficiently turn ethanol or many other hydrocarbon fuels into hydrogen in the presence of water via steam reforming, enabling the avoidance of the "chicken and the egg" problem of simultaneously transitioning to a new fuel while also transitioning to an entire new fleet of vehicles.

By using this system, once could use ordinary gasoline in their vehicle, and later on substite

non-annhydrous ethanol or hydrogen without needing to purchase a new car, essentially making all fuels interchangeable and allowing market pressures to have more control in dictating the fuels used commercially.

1.1 Catalytic Conversion to Hydrogen

Following the work of Deluga *et al.*, we can see that ethanol, air, and water can be catalytically reformed to produce carbon dioxide and hydrogen gas [1]. Stoichiometrically, this reaction is given by

$$C_2H_5OH + 2H_2O + 1/2O_2 \rightarrow 2CO_2 + 5H_2 \tag{1.1}$$
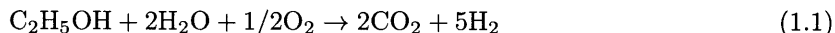
The overall reaction can be broken down into three parts,

$$C_2H_5OH + 1/2O_2 \quad \rightarrow \quad 2CO + 3H_2 \tag{1.2}$$

$$C_2H_5OH + H_2O \quad \rightarrow \quad 2CO + 4H_2 \tag{1.3}$$

$$CO + H_2O \quad \rightarrow \quad CO_2 + H_2 \tag{1.4}$$
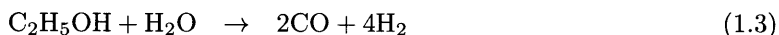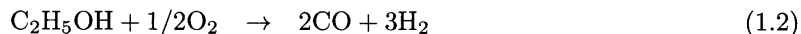
Reaction 1.2 is the partial oxidation of ethanol, and is endothermic with $\Delta H_R \sim +20$ kJ/mol. Reaction 1.3 is steam reforming, and is strongly endothermic with $\Delta H_R \sim +260$ kJ/mol. Finally, reaction 1.4 is the water-gas shift reaction in which water oxidizes carbon monoxide and releases energy with $\Delta H_R \sim -40$ kJ/mol, as shown in Figure 1-1.

Overall, one ethanol molecule undergoes partial oxidation and the water-gas shift reaction further oxidizes the CO byproduct to produce more hydrogen while eliminating an undesirable byproduct. A quick analysis suggests that the net enthalpy change would be near -60 kJ/mol, and the reported net enthalpy change is -50 kJ/mol [1]. Other estimates have put the total enthalpy of reaction at -68 kJ/mol [7]. Because the net enthalpy change is negative, the reaction overall is expected to be exothermic. Overall, some of the energy in the original source fuels is lost, but in exchange no external heat needs to be applied in steady-state to maintain the reaction, a key condition for allowing autothermal operation.

Deluga found that Rh/CeO$_2$ on a ceramic foam resulted in a greater than 100% selectivity to hydrogen in a 25 wt% solution of ethanol in water due to the water additionally contributing hydrogen to the output gas. This occurred at at a C/O ratio of ≈ 0.7. By adding a second stage of Pt/CeO$_2$ to encourage the water-gas shift reaction, they were further able to increase the selectivity to 130%. The experiment saw no buildup of carbon or other materials that could result in the deactivation of the catalyst. Due to the high cost of both Rh and Pt, preventing the deactivation of the catalyst is critical.

Unfortunately, although the hydrogen selectivity is impressive, a substantial CO remainder still

$$2\ CO_2 + 2\ C_2H_5OH + 4\ H_2O$$

$C_6H_{12}O_6 + 4\ H_2O$ $\quad$ $\Delta H° = +20$ $\quad$ $\Delta H° = -140$ $\quad$ $6\ CO_2 + 10\ H_2$

$\Delta G° = -210$ $\quad$ $\Delta G° = -330$

O_2

$\Delta H° = +2540$ $\quad$ $6\ O_2$ $\qquad\qquad$ $5\ O_2$
$\Delta G° = +2830$

photosynthesis $\qquad$ sugar $\qquad\qquad$ $\Delta H° = -2420$ $\qquad$ reformed
hν $\qquad\qquad$ fuel $\qquad\qquad$ $\Delta G° = -2290$ $\qquad$ ethanol
$\qquad\qquad\qquad$ cell $\qquad\qquad\qquad\qquad\qquad\qquad$ fuel
$\qquad\qquad\qquad\qquad\qquad\qquad\qquad\qquad\qquad\qquad\qquad$ cell

$6\ CO_2 + 10\ H_2O$ $\qquad\qquad\qquad$ $6\ CO_2 + 10\ H_2O$
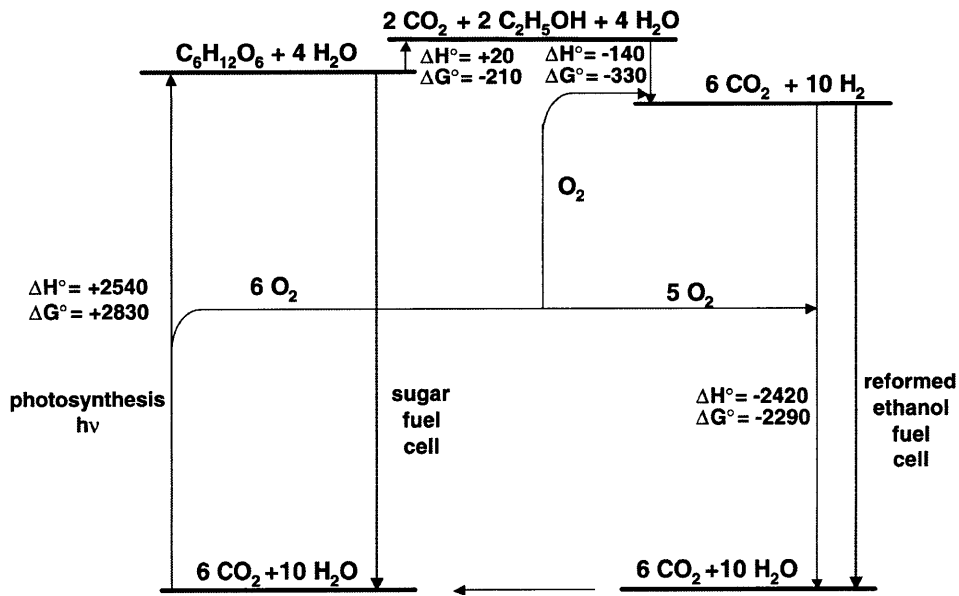
Figure 1-1: The conversion energies converting carbon dioxide and water from the air into glucose using photosynthesis, converting to ethanol, and then reconverting into hydrogen and carbon dioxide through the use of a catalyst. (Reproduced with Permission) [1]

exists, with $H_2/CO \approx 10/1$. CO will poison a PEM fuel cell following this reactor, so the amount of CO present in the system must be reduced to essentially zero before coming into contact with that sort of fuel cell. However, this problem does not apply to solid oxide fuel cells. Additionally, the optimal temperature for the system Deluga presents is 650°C, which is higher than is practical for a portable system such as would be desired for use in a vehicle.

1.2 Viability of Feedstocks

It is important to address the viability of ethanol as an energy source. Although the following is not to be considered a rigorous analysis of these concerns, particularly because all values are derived from other sources, it does provide a general idea as to the high-level issues surrounding the use of ethanol as an energy source.

1.2.1 Corn Ethanol

A very serious concern with biofuels is that by growing crops to produce fuel, we grow fewer crops to address the nutritional needs of the world population. In the case of corn based ethanol:

1. Current yields of around 328 gallons per acre. [27]

2. Current transportation energy use of 26.5 quads. [28]

3. Ethanol energy content of 29.67 kJ/gm. [6]

4. Ethanol density is 0.7893 gm/cm^3. [6]

5. The energy balance of corn ethanol is approximately 1.3:1. [29]

From this fairly well established baseline data, it is straightforward to calculate the amount of cropland that is required to use ethanol to replace our fossil fuel usage. First, to meet our total transportation need requires 26.5 quads (approximately $26.5 \cdot 10^{15}$ kJ) of energy, which, if met entirely by ethanol, is equal to $89.3 \cdot 10^{15}$ gm of ethanol. At a density of .7893 gm/cm^3, this works out to around $300 \cdot 10^9$ gallons of ethanol.

From there, it is straightforward to convert to acres of land usage — at 328 gallons/acre, we can produce that $300 \cdot 10^9$ gallons of ethanol using 911 million acres of farm land.

Unfortunately, this isn't the end of the story. Non-cellulosic corn-based ethanol has an energy content of just 1.3 times the energy put into it, mostly in the form of oil. So, while using those 911 million acres of farm land allows us to produce enough ethanol to replace our gasoline as a transport fuel, we will need over 75% of our current transportation fuel usage in order to grow that much corn. Thus, if we want to have a "closed system" where ethanol from corn is used also to grow more ethanol, we need to grow 75% more ethanol than we would think based on a pure productivity calculation. Taking additionally into account the corn required to grow that additional 75% ends up working out to an exponential decay function, the area of which is given by

$$T = \sum_{x=0}^{\infty} (1/1.3)^x \tag{1.5}$$

which, using the rules for summing infinite series, gives

$$T = \frac{1}{1 - 1/1.3} \tag{1.6}$$

or T, the total ethanol required, is 4 times the amount needed if a closed system is not enforced.

Thus, with an energy basis of 1.3:1 (which many argue is an overestimate [27]), we would need on the order of 3.6 billion acres of cropland. For comparison, the total current agricultural land in the US amounts to 450 million acres. This is clearly a huge feasibility problem in the case of corn based ethanol, as the plan inherently requires over 3 billion acres of cropland outside the country be used to produce ethanol for the US. It hardly reduces the dependence on foreign sources of fuel, and given that the US is one of the most productive countries in the world for agriculture, is unlikely to ever be plausibly produced by other countries for our use.

Additionally, by converting so much land to fuel production, the cropland remaining for food is very limited — competition is inevitable, with affluent nations purchasing food to turn it into fuel

while poor nations are unable to provide nutrition to their citizens. There are already food riots starting all over the world, and pursuing ethanol based on corn will result in disaster.

1.2.2 Cellulosic Ethanol

Cellulosic ethanol has the potential to avoid these issues by using a larger amount of the plant (around 50% as compared to just the sugar-containing seeds), and the energy balance of cellulosic ethanol could be as high as 36:1. [29] Using equation 1.5 gives us a new equation for this energy balance of

$$T = \frac{1}{1 - 1/37} \tag{1.7}$$

which is approximately unity. This means that with corn ethanol, the energy output of one hectare of plants will be enough to operate 36 more hectares of plants — within short order, petroleum feedstocks could be entirely eliminated.

However, due to the massive size of even just transportation energy use in the United States, and the low overall energy density of biomass, we would still need more than 900 million acres of farmland to produce that amount of cellulosic ethanol using corn as a feedstock, compared to the 450 million acres of farmland currently existing in the United States. This is clearly a situation where while cellulosic ethanol from corn is a great partial solution to providing a feedstock for energy use, it is physically impossible to grow enough corn in the United States to ever replace even our transportation energy needs.

1.2.3 Gigantus Miscanthus

Another crop which has shown a great deal of attention in recent years is Gigantus Miscanthus. It has a net calorific value, on a dry basis, of 17 MJ/kg, and typical yields are about 14 tons/hectare, with a water content of about 30%. This means that the 26.5 quads (approximately $26.5 \cdot 10^{15}$ kJ) of transportation energy used in the United States could be grown on about 450 million acres in the case of cellulosic ethanol, assuming the 36:1 EROEI for cellulosic ethanol will still apply.

Gigantus Miscanthus has the added advantage over corn as an ethanol feedstock of being viable on so-called "marginal land" — land where either the nutrient content, salinity, or pH is inappropriate for terrestrial crop growth. It requires substantially lower soil quality and nutrient addition than corn crops, and so although the 450 million acres of land required to grow enough of it to talk about replacing our transportation fuel energy is still a huge amount, it does not necessarily displace agricultural crops. The crops can be grown on land with little or no fertiliser, and does not require extensive maintenance to survive. This opens up the other 1800 million acres of land in the United States as potential space for producing energy crops.

1.2.4 Algae

Algae-based biodiesel has the potential to produce over 14000 gallons of biodiesel per acre of land. [30]
Additionally, algae can be easily grown in a growth media composed primarily of seawater. [30–33]
Finally, because the algae is grown in liquid, typically inside either a raceway or photobioreactor,
the algae can readily be grown on marginal land (or even in the ocean).

The energy content of biodiesel is typically around 33 MJ/L, so to produce the 26.5 quads of
transportation energy required in the U.S. will require $803 \cdot 10^9$ L, or $212 \cdot 10^9$ gallons of biodiesel.
Thus, using the best current scenario of 14000 gallons per acre for algae based biodiesel, it is possible
to completely meet the transportation needs of the United States using 15 million acres of land, none
of which needs to be farmland.

The energy balance of algae is less well established than for ethanol, as the total balance will
depend in large part on the specific technologies chosen for the production. However, if we assume
that algae based biodiesel is the same as for corn-based ethanol, we end up requiring 60 million
acres of marginal land to give the United States a completely self-contained transportation fuel
infrastructure.

Unfortunately, due to the technological difficulty in extracting biomass from liquid in the form
on one- or few-celled organisms, and the massive costs of drying them before processing, algae based
fuels currently require a very high levels of technology to operate in comparison to growing terrestrial
crops — in many cases, full time engineers are required on staff to ensure the plant is functional.
Overall, although algae is by far the best solution for producing energy in terms of energy and
land area, it requires very expensive equipment, and very expensive staff to maintain, making it
economically infeasible for the time being.

1.2.5 Improvements to Feasibility caused by Catalysts

In each of the cases of ethanol production above, the final product is annhydrous ethanol compatible
with mixing with hydrocarbon fuels. However, by using the proposed catalysts to convert ethanol
into hydrogen gas for use in a fuel cell, water is no longer a problem, and in fact the desired fuel
is less than 25 wt% ethanol in water, so the energy used in removing water will be substantially
reduced. Further, combustion in vehicles has an efficiency of about 20% compared with up to 60%
for a fuel cell.

Due to this decreased requirement on distillation and purification, the energy inputs to producing
the ethanol may be reduced by $\sim 90\%$, meaning that even corn based ethanol might have an EROEI
as high as 13:1 and cellulosic ethanol may have an EROEI of 300:1 or more. However, these numbers
are extrapolations based on the total energy inputs, and it is expected that the actual values would be
substantially lower (but still better than the current values for annhydrous ethanol) due to increased

transportation costs.

1.3 Mechanism

1.3.1 Ethanol Decomposition

The mechanism for decomposition of ethanol has been carefully studied [34–36]. Following Yee *et al.*, ethanol will bind dissociatively over CeO_2 supported metal by H- transfer from the -OH group to form an ethoxide species [35]. Subsequently, over Pt/CeO_2 and Pd/CeO_2, the ethoxides are dehydrogenated to acetaldehyde and eventually form benzene. However, Rh instead causes decomposition via methyl transfer, and decomposes into adsorbed carbon, hydrogen, and oxygen species.

Pt/CeO_2 and Pd/CeO_2 cause the formation of acetaldehyde and benzene, while Rh/CeO_2 is more active towards carbon-carbon bond dissociation, which produces adsorbed CO. This pathway is readily accessible over Rh/CeO_2, so virtually no benzene or acetaldehyde is seen in temperature programmed desorption studies.

The dominant adsorption reaction is

$$CH_3CH_2OH_{(g)} + O_{(surface)} \rightarrow CH_3CH_2O_{(ads)} + OH_{(ads)} \tag{1.8}$$
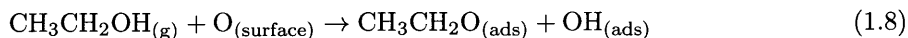
in which a hydrogen transfer takes place between the ethanol and a surface oxygen in the lattice, producing an absorbed ethoxide.

Subsequently, on Pt/CeO_2 and Pd/CeO_2, the ethoxide goes through an H-ligand migration, dehydrogenating the ethoxide while forming an adsorbed hydrogen on the catalyst surface. When the olefin is subsequently released, acetaldehyde is produced as a major product.

$$CH_3CH_2O_{(ads)} \rightarrow CH_3CHO_{(ads)} + H_{(abs)} \tag{1.9}$$
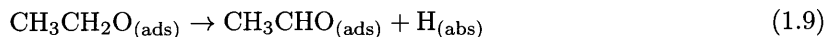
However, on Rh/CeO_2, instead of hydrogen transfer, transferring an entire methyl group to the surface becomes possible due to the reduced energy barrier to carbon-carbon bond cleavage. Thus, the ethoxide instead most likely forms a five-member oxametallacycle species connected at both ends to the catalytic surface. IR data shows that the intermediate stage then decomposes via carbon-carbon bond cleavage

$$CH_3CH_2O_{(ads)} \rightarrow CH_{3(ads)} + CH_2O_{(ads)} \tag{1.10}$$

27
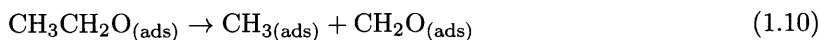
and the resulting adsorbed species subsequently dissociate

$$CH_2O_{(ads)} \quad \rightarrow \quad CO + 2H_{(ads)} \tag{1.11}$$

$$CH_{3(ads)} + H_{(ads)} \quad \rightarrow \quad CH_4 \tag{1.12}$$
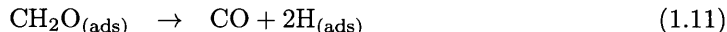
the end result of which is the production of CO and methane.

The methane will be inert in a fuel cell and CO is a PEM fuel cell poison, so this result is undesirable. However, Rh is also an active promoter of the water-gas shift reaction, as is the much less expensive Ni [36]. Thus, either Rh by itself, or Rh in combination with Ni will be able to further react to produce

$$CH_4 + H_2O \rightarrow CO + 2H_2 \tag{1.13}$$

via steam reforming, and also produce

$$CO + H_2O \rightarrow CO_2 + H_2 \tag{1.14}$$

via the water-gas shift reaction.

Wheeler *et al.* found that the most effective metal for CO conversion was Ni with an 82% selectivity ($\sim$70% for Rh), while producing $\sim$7% methane for Rh and $\sim$5% for Ni [36].

1.3.2 Ceria Support

CeO_2's enhancement of the catalytic efficiency of the previously discussed metal catalysts is well established, but the mechanism by which CeO_2 actually assists in the catalytic process is still being investigated. Currently, the dominant theory is that due to CeO_2's fluorite structure, oxygen atoms are easily able to diffuse through the crystal, allowing it to both donate and absorb oxygen readily as needed. Thus, the activity of CeO_2 in assisting catalysis is heavily dependent upon the type, size, and distribution of oxygen vacancies in the crystal [37,38].

In CeO_2, reduction results in a valence change Ce^{4+} to Ce^{3+} of two Ce atoms, producing a seeming continuum of oxygen-deficient non-stoichiometric oxides which organize into highly ordered fluorite-related superstructures of CeO_x with $1.714 < x < 2$. These vacancies result in an extraordinary efficiency for reversible oxygen release. This also allows for the formation of more stable states of catalytically active metals adsorbed on the surface, and are crucial for the binding of catalytically active species to ceria [38].

For example, the high activity of Au/CeO_2 catalyst for the water-gas shift reaction is dependent upon the presence of a highly dispersed, ionic Au species that is stable only in the presence of such an oxygen defect [39]. In fact, in the case of Au/CeO_2, a cluster of only 4-6 Au atoms at an oxygen vacancy site is sufficient to catalyze the water-gas shift reaction [40]. The ceria oxygen vacancy

critical for the stability of the ionic Au species; metallic Au is essentially inactive in comparison.

Following the work of Liu *et al.*, computer simulation has suggested that Au binding to the most stable CeO_2 {111} type planes prefer to sit in an oxygen vacancy site on a reduced surface, while on a stoichiometric CeO_2 {111} surface the Au prefers to bind to surface lattice oxygen [40]. The adsorption energies calculated were 1.86 eV for the {111} plane at an oxygen vacancy versus 1.26 eV for the {111} stoichiometric lattice oxygen site. Upon calculation of the electron densities, it was also found that the Au bound to an oxygen vacancy was strongly negatively charged (-0.58 q) versus positive (+0.35 q) for the stoichiometric lattice oxygen site.

The most critical result from the simulation of CeO_2's interaction with Au is that of the CO binding energy. CO is frequently a poison for metal catalysts because of the strong binding energy it exhibits. If the catalyst cannot regenerate by releasing CO, then it is no longer usable. However, in the Au/CeO_2 system, the binding energy is 2.37 eV for the stoichiometric {111} surface, but only 0.09 eV for the reduced {111} surface, showing how the negative charge induced by the Au interaction with a ceria oxygen vacancy reduces the binding energy of the CO sufficiently to allow it to be effectively catalyzed without poisoning the system. Additionally, computer simulation showed that it is critical that the ceria is in the CeO_2 phase, and not the fully reduced Ce_2O_3 phase, as gold bound to the {1111} surface of Ce_2O_3 is also positively charged and has a CO binding energy of 0.81 eV.

Liu also found that the presence of Au in an oxygen vacancy led to a substantially improved binding energy for Au binding to lattice oxygen adjacent to the vacancy, by as much as a factor of 2. Thus, an Au bound to an oxygen vacancy will nucleate the growth of small Au clusters, with positively charged gold present in the cluster. Overall, the system then can adsorb CO on the positively charged Au cluster surrounding the vacancy while the central Au atom remains active for CO catalysis and release as CO_2.

The electronic stability for this was found to be the result of oxidation by Ce in the non-stoichiometric CeO_2 lattice. As an Au atom approaches a surface lattice oxygen, it's half-occupied $6s$ orbital overlaps with the fully occupied $2p$ oxygen orbital and becomes an Au-O anti-bonding orbital. The anti-bonding electron can then be transferred to an empty Ce $4f$ state, allowing the Ce to oxidize the adsorbed Au. This explains why the fully reduced Ce_2O_3 binds so poorly to gold, as there are no electrons on the Ce available near the Fermi surface.

With this knowledge, Liu demonstrated a feasible pathway for the water-gas shift reaction on the surface. It was found that H_2O binds weakly to the surface, and that the barrier to dissociation was only 0.59 eV, leading to adsorbed OH and H species. Subsequently, the OH group can readily react with the adsorbed CO to produce an adsorbed COOH group with an energy barrier of only 0.10 eV. Next, the COOH can lose the H, releasing CO_2 with an energy barrier of 1.08 eV. Finally, two adsorbed H atoms produced this way combine to release H_2.

1.4 Material Properties

A number of significant advances in understanding the catalytic conversion of ethanol have been made since Deluga's paper in 2004. Much of this work has focused on what material is used in conjunction with CeO_2 in an effort to eliminate CO and acetaldehyde byproducts, increase efficiency, and decrease operating temperature [2,7,9,10,12,16,41]. In addition, much work has been done on ways to improve the properties of the CeO_2 co-catalyst to enhance catalysis and simplify synthesis [3,4,8,42–52].

1.4.1 Variations in catalyst materials.

The most significant improvement found is caused by the addition of a metal specifically to catalyze the water-gas shift reaction to the system — while Deluga *et al.* added a second stage of Pt/CeO_2, CO and acetaldehyde are also effectively removed by the addition of Pt or Au directly to the Rh-CeO_2 system [7,9,16,41].

Sheng *et al.* did work that suggested a Rh-Pt/CeO_2 system was required for efficient low-temperature ($\sim 400°C$) production of H_2 from ethanol [10]. They found that, as would be expected based on our understanding of the mechanism for catalysis, acetaldehydes were formed over Pt/CeO_2 and Rh/CeO_2 surfaces when unreduced while over a Rh-Pt/CeO_2 reduced surface, the ethoxides decomposed instead into CO and methane. The most interesting aspect of this work was that it was done at low temperatures (400°K), and that combining Rh and Pt reduced the barrier to reaction compared to either individually. However, this work did not utilize the water-gas shift reaction, and instead only dealt with

$$CH_3CH_2OH + 1/2O_2 \rightarrow 2H_2 + 2CO \tag{1.15}$$

the partial oxidation of ethanol to form hydrogen and carbon dioxide.

Idriss and Morrison also demonstrated that Pt-Rh/CeO_2 has promise for the oxidation of ethanol [9,16]. Idriss showed that Pt-Rh/CeO_2 at 500 °C was able to produce 17% H_2 with 12.14% CO and 11.98% CH_4, and also found that Au-Rh/CeO_2 at 400°C produced 15.09% H_2 with 15.65% CO and 14.39% CH_4. The resulting suggestion of using Rh-Pt/CeO_2 is reasonable for a pure ethanol stream in which the only mechanism is oxidation. However, by adding water to the fuel stream, it is possible to achieve substantially better performance overall by incorporating the water-gas shift reaction as Deluga and Salge did originally [1,7].

Kugai suggests a much more practical solution, which is to use a bimetallic Ni-Rh/CeO_2 catalyst [2,12]. Ni is a particularly promising candidate because its *d*-orbital is very similar in shape to that of Rh, meaning it should have the potential for similar reactions (and shouldn't produce as much acetaldehyde as Pt, Pd, Ru, and Au). Ni is also much less expensive than Rh, and is known to participate in the water-gas shift reaction. By adding Ni to a Rh based catalyst, it should be

possible to reduce the output of CO while decreasing the cost.

Overall, Kugai found that by using Ni-Rh/CeO$_2$ with a fuel stream containing ethanol, water, and oxygen, the minimum ethanol conversion temperature was reduced to around 375°C. The yield at this temperature was 2.3 mol H$_2$/mol EtOH. Simultaneously, the acetaldehyde output was nearly zero, and the CO output dropped to below 5 mol%, a substantial improvement, while H$_2$ was ~60% of the output. However, doing this lower temperature reaction over Ni-Rh resulted in an increased amount of methane — ~15% versus ~6%. Unfortunately, Ni by itself only achieved a 40% conversion of ethanol while 10% Ni - 1% Rh achieved over 92% conversion, showing that Rh is necessary for the catalyst to be effective. The overall reaction as investigated by Kugai is shown in Figure 1-2.

There is a trade-off between CO and CH$_4$ produced, which can be controled with temperature. While CH$_4$ lowers the H$_2$ output by competing for hydrogen, CO is a poison for PEM fuel cells, suggesting that the preferable solution is one where some fuel is lost, but less CO cleaning downstream is necessary before the gas is usable. The optimal ratio of Ni-Rh was shown to be ~ 5:1 for these nanoparticle systems, and oxygen in the fuel enhances ethanol reforming more effectively than water [12]. At low temperature, more CH$_4$ is produced, while at high temperatures, more CO is produced.

1.4.2 Overview of CeO$_2$ properties.

As discussed earlier, the key mechanism for CeO$_2$'s ability to enhance the catalytic abilities of many metals is governed directly by the size, type, and number of oxygen vacancy defects on the surface of the crystal [39, 40]. Thus, on a larger scale, we would expect that two primary features of the CeO$_2$ will determine it's catalytic effect.

1. The total surface area of CeO$_2$.

2. The fraction of surface sites with oxygen vacancies.

One would expect that nanocrystalline CeO$_2$ then would be highly favorable due to an inherantly high surface area to mass ratio, while a higher curvature would likely result in a higher fraction of defects on the surface. Indeed, Deshpande used XPS analysis of the $3d$ Ce states to measure the oxygen defect concentration as a function of nanocrystal size [3]. By measuring the fraction of Ce^{3+} versus Ce^{4+} (2 Ce^{3+} are formed by every oxygen vacancy [38].), an estimate of the concentration of oxygen vacancies can be made.

The results of this analysis showed that 3 nm CeO$_2$ had a concentration of 44% Ce^{3+}, 6 nm CeO$_2$ had a concentration of 29% Ce^{3+}, and 30 nm CeO$_2$ had a concentration of 17% Ce^{3+}. Although the estimate of concentration given by this analysis is likely not equivalent to the operating conditions of the catalyst (XPS is performed under room temperature vacuum, while the operating conditions will be high temperature and at least atmospheric pressure), the trend still shows that small CeO$_2$
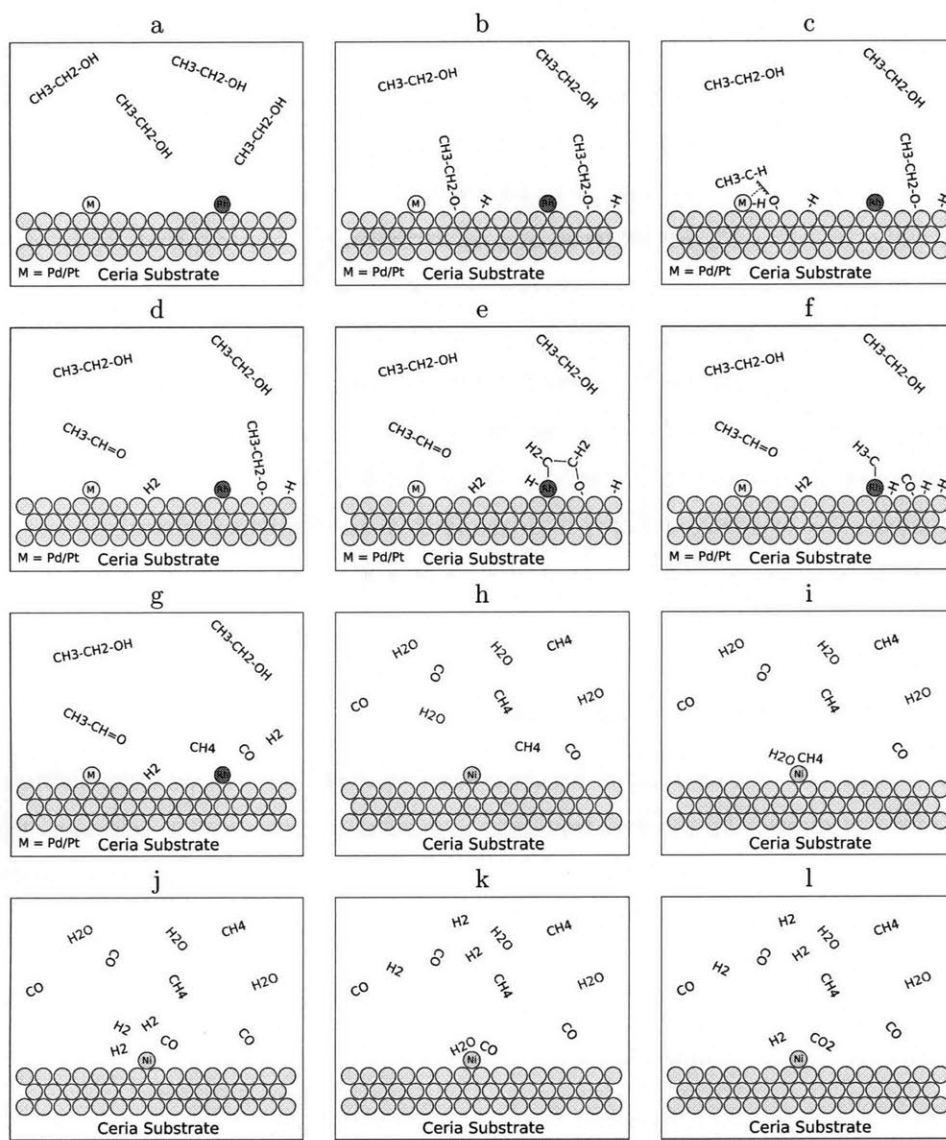
Figure 1-2: Cartoons showing the reactions taking place over M/CeO_2.. (a) Ethanol over a Pd/Pt or Rh catalyst supported on CeO_2. (b) Ethanol adsorbes on the CeO_2 surface. (c-d) Over Pd/Pt, the catalyst abstracts a hydrogen, forming formaldehyde. (e-f) Over Rh, the catalyst instead is able to form a 5-member oxymetallacycle ring, resulting in carbon-carbon bond cleavage and the formation of a methyl along with a variety of CO and H adsorbed on the surface, (g) which are subsequently released. (h-j) Nickel catalysts on the same CeO_2 surface can then bind to the methane now in solution and react with H_2O to form hydrogen and CO. (k-l) Finally, the nickel catalyst can catalyze the oxidation of the remaining CO with H_2O to form more hydrogen and carbon dioxide.
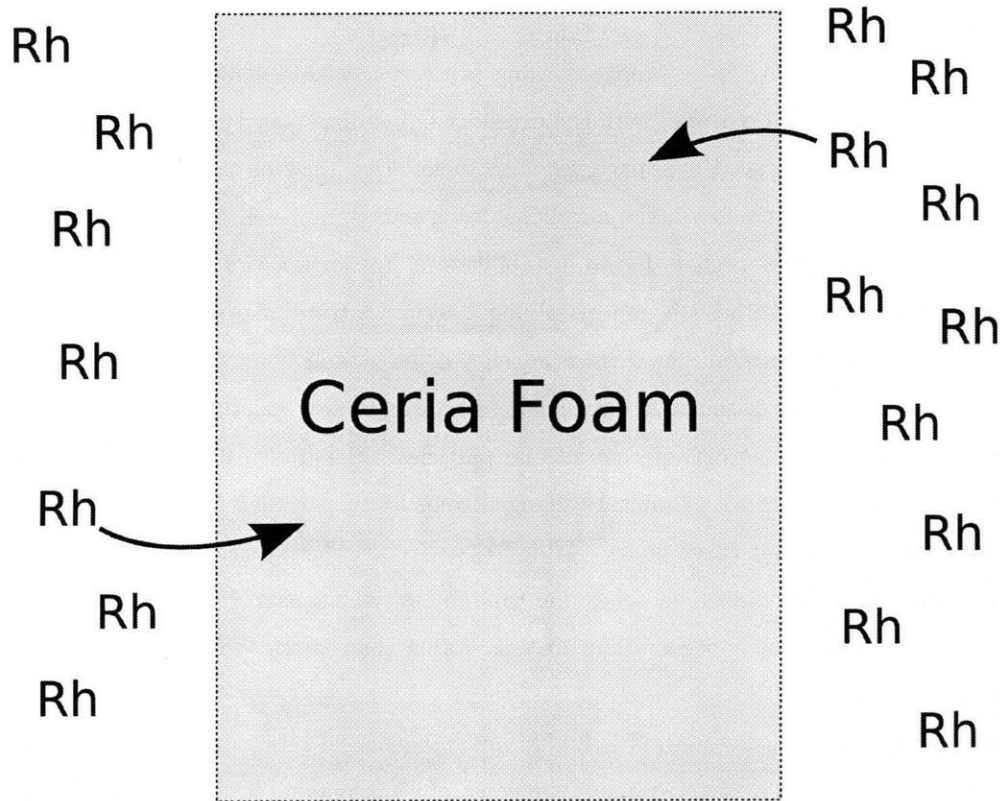
Figure 1-3: In Wet Impregnation, a Ceria foam would be exposed to a rhodium precursor such as RhCl$_3$ and subsequently calcined and oxidized at high temperature to decompose the precursor into metallic rhodium.

particles will have a substantially increased oxygen vacancy concentration compared to larger CeO$_2$ particles. Absorption near edge spectroscopy may produce more reliable measurements of the oxygen vacancy concentration [1].

Another potential problem with CeO$_2$ is it's relatively low stability to sintering. It was found that at temperature ranges near the operating conditions (500-800°C), clusters of $\sim$ 10 nm sized nanocrystals were sintered to form secondary particles [42]. However, the addition of a small fraction of La$_2$O$_3$ provides stability against CeO$_2$ sintering [39].

1.4.3 CeO$_2$ Synthesis Methods

Syntheses for CeO$_2$ nanocrystals have been under development for several decades. Some syntheses use solid-state reactions or hydrothermal syntheses [47, 48]. Many others have used homogeneous precipitation or two-phase syntheses [46, 49, 50, 52]. The most common commercial method is wet impregnation, where an existing CeO$_2$ foam is impregnated with rhodium precursors and calcined to produce nanoparticles attached to the CeO$_2$ surface as shown in Figure 1-3

This subsection will focus on precipitation type syntheses due to the compatibility with virus-

based templating.

CeO_2 nanoparticles have been prepared using a reaction within a reversed micelle [46]. This method formed quite small particles with the excellent mono-dispersity typical of such syntheses — typically $\sim$ 5 Å, and produced nanoparticles with mean sizes between 2.6 and 4.1 nm which was controllable by changing the size of the micelles in each micro-emulsion. 2.6 nm was established as the lower size limit for this method due to instabilities in smaller micelles.

The reversed micelle synthesis began by mixing a cerium nitrate micro-emulsion with an ammonium hydroxide micro-emulsion. As inverse micelles collide, their components mix, resulting in a reaction. In all cases, the initial reaction caused the initially clear solution to become translucent while gradually precipitating orange-colored fine particles. Masui also found that for low surfactant concentrations, the orange precipitate changed color to purple, then to pale purple, and finally to a light yellow over about three hours. After freeze drying, the particles became a light brown. Masui explains this color change as being due to stability, where particles formed inside a reverse micelle in a low surfactant concentration are less stable than those formed in a high surfactant concentration [46].

While the reversed micelle method is highly advantageous in terms of mono-dispersity and repeatability, the reaction is performed in non-aqueous solution, making it difficult to utilize for virus-based templating. However, an elegant, simple, and bio-compatible synthesis based on homogeneous precipitation was developed by Yamashita *et al.* [50, 52].

In this synthesis, a mixture of Ca and Ce salts are mixed in aqueous solution, pH adjusted with NaOH to form cerium hydroxide, and oxidized with H_2O_2 to produce nanocrystalline cerium dioxide. After the initial reduction of $CeCl_3$ with NaOH, nanorods of $Ce(OH)_3$ are formed. The pH is adjusted with HCl or NaOH, and oxidation is done with H_2O_2. With pH 11 during oxidation, polycrystalline rod shaped structures $\sim$ 50 nm long and $\sim$ 5-10 nm in diameter with $\sim$ 5 nm crystal domains were formed. However, with pH <7, the same oxidation process resulted in the nanorods of $Ce(OH)_3$ dissociating into spherical nanocrystals of diameter $\sim$5 nm. Finally, when the oxidizing agent was added simultaneously with the NaOH, the resulting particles were spherical, despite a pH of 11, most likely because the cerium hydroxide was not present for a long enough time to form rods before being oxidized to the stable single-crystal spherical state. Yamashita's synthesis is

1. 1M total $CaCl_2$ + $CeCl_3$ added to 100 mL H_2O.

2. 3M of NaOH added to 100 mL H_2O.

3. 25mL H_2O_2

4. All 3 solutions simultaneously added to 150 mL 40°C H_2O with stirring.

Particularly beneficial with this synthesis is that the entire reaction is done in water, which is a critical feature of any virus-compatible synthesis. Additionally, NaOH, HCl, and $CeCl_3$ are unlikely

Size	BET	Pore	EtOH	H$_2$	CO	CH$_4$	CH$_3$CHO
6.5	128	3.7	57	52	9	11	4
29.3	67	6.2	42	43	16	15	9
10.2	65	10.7	40	36	17	16	19

Table 1.1: Effect of Substrate Properties on EtOH conversion efficiency. Crystal Size (Size) is in nm, BET Surface Area (BET) is given in m^2/gm, Pore Size (Pore) is in nm along the diameter, and EtOH Conversion (EtOH) is given in total percent converted at 300°C at the optimal flow rate for each catalyst sample. The other component concentrations are given as the fraction of the stream not including ethanol or water. [2].

to be poisonous to the virus, and the pH value can be controlled to be within a bio-compatible range without degrading the quality of the product.

1.4.4   Variation of Metal/CeO$_2$ structure.

The nano/micro-structure of the Ni-Rh/CeO$_2$ system has a substantial effect on the final product quality. For example, the only active sites for catalysis are where Rh or Ni atoms are touching or very near a CeO$_2$ oxygen vacancy, so a high degree of dispersion is desirable. If the Rh and Ni were to phase separate, very few atoms would be active for catalysis compared to the total number of atoms in the structure. Additionally, if the Rh and Ce are embedded within each other, a large fraction of the active sites for reaction will be inaccessible to ethanol molecules flowing past. Finally, an overall high surface area of exposure is desirable, because even if the fraction of active sites per unit area is high, if the total area is small the reaction will take place slowly overall.

Thus, an ideal nano/micro-structure for the catalyst is one in which

1. All Rh atoms are near a CeO$_2$ oxygen vacancy.

2. All Rh atoms are also at the surface of the structure.

3. The structure itself has an extremely high surface are/volume ratio.

Of additional worry is that Rh has been shown to sinter due to local hot spots produced by the total oxidation of ethanol [7]. This introduces an additional requirement that

4. Rh atoms are physically isolated from other Rh atoms.

Kugai *et al.* tested a variety of CeO$_2$ nanocrystals under identical Rh/Ni loading (5% Ni — 1% Rh) using coimpregnation of prepared CeO$_2$ [2]. They found that out of three samples, the most effective was over a substrate of 6.5 nm CeO$_2$. Table 1.1 summarizes the results when the catalyst is operating at only 300°C. As can be seen by the improvement the 6.5 nm particles show over the 29.3 or even 10.2 nm particles, size has a substantial effect on the dispersion of Rh/Ni in the system.

It is likely that an additional size effect is also having an effect on the highly increased efficiency of 6.5 nm crystallites as compared to the 10.2 and 29.3 nm particles. As CeO$_2$ crystallite size decreases,

the fraction of Ce^{3+}, indicating oxygen vacancies present in the system, increases dramatically [3,4]. The concentration of oxygen vacancies in 6 nm CeO_2 is 15% compared to only 9% in 30 nm nanocrystals. The only active sites in the system are where an CeO_2 oxygen vacancy interacts with a metal atom, so 6 nm nanocrystals have a higher oxygen vacancy concentration to begin with, resulting in higher numbers of active sites. Other methods of catalyst formation such as co-precipitation also show that smaller nanocrystal sizes are more active for ethanol reforming [8].

Although the Ni-Rh/CeO_2 6.5 nm crystallite system converted ethanol with good specificity and very little CO production at temperatures of only 300°C, after 5 hours of operation, the ethanol conversion rate decreased significantly with an increase in CH_4 and CO produced. However, above 450°C, the ethanol conversion was stable for long times, most likely because the impurities blocking catalysis were desorbed at higher temperatures [2].

1.5   Application of Biotemplating to Catalysis

The primary issues with co-precipitation and wet impregnation alone derive from the final dispersion being random. The position of Rh and Ni with respect to CeO_2 is determined primarily by chance, with a bias towards phase separation of the Rh/Ni from the CeO_2. Mixing is improved by decreasing the size of crystallites, but there is no nano-scale control dictating the relative positions of Rh, Ni, and CeO_2.

This lack of control results in rhodium and nickel being close together, encouraging coarsening of the catalyst materials and gradual deactivation. Overall, using the particles in a 3-D matrix also results in a quantatively lower thermal stability due to the presence of available material to coarsen into in all directions. Further, the phases of the catalyst materials being used is dictated purely by homogeneous thermodynamics, meaning that only the most thermodynamically stable phases of the materials of interest are likely to appear.

By incorporating nano-scale structure with a programmed high dispersion between already small nanocrystals with high oxygen vacancy concentrations, substantial improvements to the catalytic efficiency of Rh/CeO_2 should be possible. Additionally, the assembly into nanowires instead of bulk collections of nanoparticles should be highly resistent to coarsening due to the vastly limited number of adjacent nanocrystals to coarsen into. Finally, through the use of proteins designed to encourage nucleation of desired phases, we can potentially incorporate otherwise unstable phases, or more pure phases of desired catalyst materials — for example, nucleating rhodium metal instead of rhodium oxide on the catalyst surface.
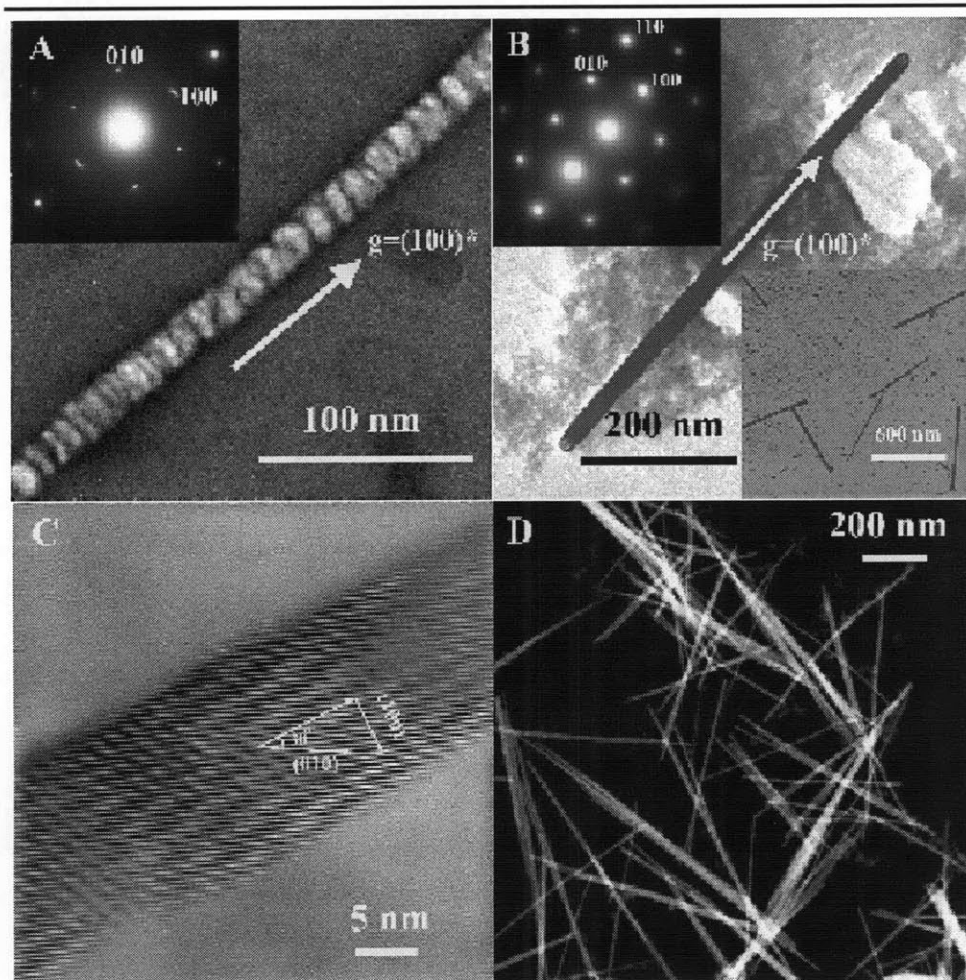
Figure 1-4: Nanowires of Co$_3$O$_4$ synthesized by Ki Tae *et al* using phage based templating, and showing the single crystalline final structure. (Reproduced with Permission) [54]

1.5.1 Virus Templating.

Ki Tae Nam *et al.* demonstrated recently that by using the M13 bacteriophage, it is possible to control with extremely high precision the assembly of nanowires of Co$_3$O$_4$ with a small percentage of a Au dopant, as shown in Figure 1-4 [53]. The M13 virus consists of $\sim$2700 major coat proteins on it's surface, and is structurally $\sim$1 μm long and 10 nm in diameter. By utilizing bioengineering techniques, it is possible to randomize the sequence of amino acids expressed on the major coat protein, allowing rapid selection for a specific genome which will result in a protein coat with binding affinity for a desired target material. Previously, this technique has been used to produce semiconductor and magnetic nanowires [54].

In this example, an M13 phage with a protein coat having an affinity for Co$_3$O$_4$ is incubated in an aqueous cobalt chloride solution for 30 minutes at room temperature. Subsequently, the solution was

reduced with NaBH$_4$ and oxidized with water to form monodisperse, crystalline Co$_3$O$_4$ nanowires composed of virus-templated $\sim$ 2-3 nm nanocrystals uniformly mineralized along the length of the virus. Further control by varying the concentration of cobalt chloride resulted in new and exotic structures, such as branchlike nanowires while lower concentrations resulted in discrete nanocrystals assembled along the virus surface.

A 12-amino acid peptide with a high binding affinity to Au was then inserted into host bacterial cells infected by the Co$_3$O$_4$ bacteriophage, resulting in a bi-functional virus constructed to express primarily Co$_3$O$_4$- specific peptides with a small number of "dopant" Au- specific peptides on the surface.

By first incubating the bi-functional virus with 5 nm Au nanocrystals and subsequently removing unbound Au with centrifugation, M13 virus with a small number of Au nanocrystals spatially separated on the major coat were made. Subsequent incubation and reduction in the presence of Co ions resulted in 5 nm Au nanocrystals spatially interspersed within the Co$_3$O$_4$ nanowires, with $\sim$2.4% Au in the final system.

1.5.2   Application of Virus Templating to M/CeO$_2$.

Ki Tae Nam *et al.* demonstrated that it is possible to use peptides in the major coat of M13 bacteriophage to give nano-scale control over the arrangement of nanocrystals in a nanowire [53]. By integrating a small number of Au nanocrystals into a Co$_3$O$_4$ nanowire, they were able to produce battery electrodes with substantially improved electrical properties.

This nano-scale structuring is ideal for improving the catalytic properties of the Rh/CeO$_2$ system. By engineering an M13 virus with a major coat specific to CeO$_2$ and a small percentage of dopant peptides specific for Rh alone, we can create spatially interspersed Rh nanocrystals in an overall CeO$_2$ nanowire. This nano-structure has all the properties of an "ideal" catalyst micro/nanostructure as discussed previously, as shown in Figure 1-5

1. All Rh atoms are near a CeO$_2$ oxygen vacancy.

2. All Rh atoms are also at the surface of the structure.

3. The structure itself has an extremely high surface are/volume ratio.

4. Rh atoms are physically isolated from other Rh atoms.

5. Templating allows for highly porous structure.

First, this nano-structured system ensures that all or nearly all Rh atoms are touching a Ce atom, causing a substantial increase in the probability that a Rh-CeO$_2$ vacancy will occur, reducing the amount of "inactive" Rh in the system. This will reduce the amount of Rh that is required for operation, decreasing the cost of the system dramatically.
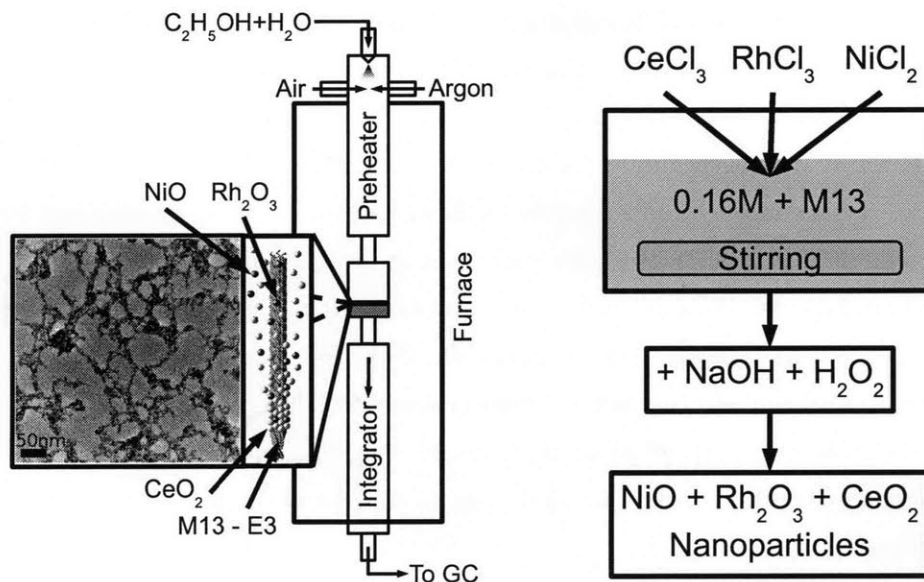
Figure 1-5: Experimental Design. Rhodium, nickel, and ceria are simultaneously nucleated on the surface of the M13 phage, forming a highly porous structure. The resulting dried powders are tested in a custom built chemical reactor to characterize the performance for hydrogen production from ethanol.

Second, the M13 virus is acting as a scaffold with only a monolayer of nanocrystals at the surface. The vast majority of Rh atoms are near or at a surface — very little Rh will be trapped inside the virus, and the only inaccessible Rh will be the half of each nanocrystal on the "underside" of the surface monolayer. This again reduces the amount of inactive Rh in the system, further decreasing the cost of the catalyst.

Third, a nanorod has an extremely high surface area to volume ratio – assuming a uniform coat of 5 nm around the virus, the result is a rod 1 μm long and 20 nm in diameter. Thus, assuming no sintering between nanorods, the surface area can be as high as 200 m^2 per cubic centimeter of material. Further, the concentration of metal salts in solution during nanocrystal growth can substantially change the structure of the final wire. For example, by using a smaller concentration of precursor than would provide a uniform coat, you further nano-structure the nanorods with dimples or potentially entirely discrete nanocrystals, increasing the total surface area even more. This suggests you could have an even higher eventual surface area, although in this particular reaction it is very likely that due to the high temperatures involved in catalyst operation, the biological scaffolding will break down. Ensuring the formation of a nanorod that is structurally stable once the virus is gone is critical. However, the final pore size distribution may have a substantial impact on the final product distribution and catalyst activity.

Fourth, although technically the final position of M-binding peptides in the surface coat is random, the discreteness that the peptides give positions along the M13 virus coat makes it very

unlikely to find large numbers of M-binding peptides adjacent to each other. There is very little thermodynamic impetus toward Rh-binding proteins phase separating on the surface from the other coat proteins, especially compared to the thermodynamic driving forces tending to combine similar nanocrystals which are not chemically immobilized on a surface. Thus, overall, while two or even three Rh nanocrystals might be adjacent, the number of adjacent Rh nanocrystals will be substantially reduced from that given by wet impregnation or co-precipitation. The result of this feature is that due to physical separation and mechanical attachment, Rh nanocrystals will not sinter together due to hot spots during catalysis. The separation should be further enhanced by the 1-D nature of a nanowire compared to the 3-D structures more typically found in nature.

The goal of this work is therefore to use bioengineering techniques to produce a biotemplated catalyst containing rhodium, nickel, and ceria, and to test the catalytic performance and stability in a custom built chemical reactor.

Chapter 2

Review of Catalyst Preparation Methods

Catalysis is a very broad field, requiring the integration of a variety of disciplines. Chemical engineering and mechanical engineering are required to understand gas diffusion, heat transport, and structural stability of a reactor and supporting equipment under potentially high pressures and temperatures. Materials Science is required to understand the nano and microstructural features of catalysts powders, as well as to fully understand the mechanisms behind deactivation such as sintering and coking. Chemistry is required to understand the actual reaction rates, reaction intermediates, the various chains that occur to produce various byproducts, and to understand the basic thermodynamics of the reactions being carried out.

This chapter will focus primarily on the Materials Science aspects of catalyst preparation, and in particular the various methods used in industry to produce industrially interesting catalysts, starting with synthesis, and ending with the various heat treatments and pelletization that may be necessary depending on the particular applications.

The format of this chapter is largely based on a single reference, the book "Catalyst Preparation Science and Engineering", a review edited by John Regalbuto. [55] This text was published in 2007, and was recommended by an industrial catalyst engineer as a text covering all of the most common current techniques used in industry. The text generally covers the wide variety of techniques being used and the typical results they produce; essentially written based off of industrial catalyst research done by chemical engineers.

As a material scientist, my perspective is rather different, and while the book does not go into a great deal of detail about the mechanisms and reasons for why particular techniques work, exploring that direction of research presents a very useful and relatively unexplored direction for materials research. This chapter is thus largely for my own benefit, as I had very few academic resources

to draw from in learning about these systems from a materials perspective, and writing this into a formal presentation allows me to make an attempt to apply materials science principles to the results from decades of industry experience.

2.1 Synthesis Routes

2.1.1 Flame Hydrolysis

This is a technique dated back to World War II whereby a vaporized metal chloride precursor which will decompose in water, such as silicon tetrachloride, is hydrolyzed in a hydrogen/oxygen flame. As the hydrogen burns and reacts with oxygen, it produces very finely dispersed water molecules in the vapor phase. The water molecules then react with the metal chloride to form the corresponding metal oxide nanoparticle along with hydrochloric acid. The scope of materials producible with this reaction is limited primarily by the availability of a precursor which decomposes upon contact with water, but includes silica, titania, alumina, and zirconia.

The primary handles by which the final properties of the material such as surface area, particle size distribution, and aggregation extent include the flame temperature, flow rate, ratio of precursor to fuel, hydrogen to oxygen ratio, and the residence time in the reactor. From a materials perspective, it is fairly easy to guess in what way these influence the final particle properties.

Properties

Typical surface areas for catalysts made in this way are 50-400 m^2/gm. As might be expected from a covalent compound so violently transformed from the vapor to the solid phase at high rates to produce nanoparticles, the nanoparticles are frequently amorphous — the individual molecules do not have time to arrange themselves into the most thermodynamically stable structure. The isoelectric points of these compounds can range from 2-9, depending widely on the extent of dehydroxylation of the final material.

For many situations, a highly acidic surface is desired. This is typically accomplished in materials synthesized via pyrolysis by subsequent heat treatment to dehydroxylate the material and expose lewis acid sites caused by oxygen defects at the surface where an aluminum atom is not fully coordinated. An alternative method for producing a highly acidic catalytic surface is to use an amine capping agent to coat the material during synthesis. This is accomplished by starting the synthesis from an alkoxide precursor and protecting with an amine while performing water-limited pyrolysis (low fuel to precursor ratio — lacking enough water to displace the protecting amine).

2.1.2 Aerogel Synthesis

A gel is generally a solid-liquid mixture formed via sol-gel chemistry, with a long-range solid secondary structure. How this solid-liquid mixture is dried determines if it is an aerogel, xerogel, or cryogel, all of which have related properties.

An Aerogel is formed when the liquid is removed from the mixture via supercritical drying. The pressure and temperature of the mixture are raised such that the liquid solvent becomes supercritical, allowing it to change phase to a vapor and exchange with the environment without any rapid volume changes which could cause damage to the microstructure of the catalyst support. Further, the liquid becomes much less viscous under these conditions, allowing for it to be extracted comparitively quickly from the mixture. Pore collapse in this situation is typically governed by the capillary gradient of pressures inside the pores.

The remaining solid then frequently maintains a high level of network connectivity without collapsing as it would if it was dried more violently, as with xerogel (drying in air), or with a cryogel (drying by freezing). This structure is highly desirable in some situations of reaction rate limited catalysts because the surface area is extremely high, and the structure is highly porous (more than 90% porosity).

Synthesis

The critical difference between a "sol" (colloidal suspension) and a "gel" (wet monolith) is that in a sol there is no long-range secondary network of solid material. An example of a colloidal solution is a suspension of gold nanoparticles in water. To form a long-range three-dimensional secondary network of solid material, a transition phase is required which increases the density of the sol to above a critical point where the amount of solid is sufficient to form a network.

This sol-gel synthesis step is also seen in phage technology; as the concentration of phage increases to a large enough extent, the addition of a small amount of metal chloride will result in the formation of a very clear gel. This does not happen below a critical concentration of phage.

After a gel is formed, the gel is dried in an autoclave to achieve supercritical drying, followed by calcination. In the case of gels formed in a water solution, the water must be exchanged with a different solvent such as ethanol in order to dry without damaging the structure of the material. This poses a problem for implementation with phage, although ethanol addition at the stage where a gel is formed may not cause any problems with the biological components at that phase of the synthesis.

Properties

Aerogels can have surface areas of 1000 m^2/gm, and otherwise exhibit similar particle sizes and pore size distributions to materials made using a sol-gel synthesis method regardless of drying method.

These aerogels can also be used as a support and are readily suited for use in heterogeneous (multi-component) catalysts systems. Any system in which a colloid solution could be made represents a good candidate for an aerogel-based heterogeneous catalyst. It is also potentially possible to use a gel method to coat a monolith with a very highly porous surface layer by careful drying.

Cogelled Catalysts

A catalyst can be synthesized simultaneously with its support by "cogelling", when both materials are created using a sol-gel method at the same time. Gels formed this way can have unique properties that make them very attractive as a catalyst.

Cogelled catalysts have three levels of ordering. First, each individual particle is formed. These individual particles then aggregate into a small cluster, and then these clusters form a pellet of mixed particles and pore. Cogellation can be used to trap a metal nanoparticle inside a microporous support particle through the use of a chemical trap such as a mercaptoethoxysilane. This can be desirable because the cogellation traps (similar to the protein templated traps) physically isolate the metal nanoparticles to prevent sintering. However, the downside to this method is that mass transport is limited by the size of the pores in the substrate. This is less of an issue with phage nanowires, but it suggests that synthesizing the metal on the surface of the phage, and subsequently coating the metal+phage wire with ceria or another cocatalyst substrate may significantly improve selectivity (only small molecules can fit through pores) and improve sintering resistance further (which is already seen using nanowires as well).

2.1.3   Producing highly mesoporous catalysts.

The ability to synthesize materials with a very well-defined and stable particle size, morphology, and mesoporosity (2-10 nm size scale) is critical for producing reliable and well-tuned catalysts. The particle size is related to dispersion, surface area, and surface speficic activity; morphology dictates structural stability, resistance to coarsening, and diffusion rates of reactants; mesoporosity dictates surface energy, how long molecules are trapped near the catalyst, and can indicate a much higher effective surface area.

In particular, a material with mesopores may be much more interesting as a catalyst than a solid material. A higher effective surface area, and potentially interesting features such as diffusion limited reaction rates, can cause improved selectivity, as is the case with zeolites (microsieve materials).

One method that can be used to produce this sort of pore distribution is by using organic functionalization during particle formation. The initial particles are formed with organic molecules such as TEOS (tetraethoxysilane) embedded into the structure at room temperature. Subsequent heat treatments drive off the organic molecules, leaving a solid with pores in it defined by the missing organic molecules.

As an illustration, imagine a silica bead. On the surface, you attach TEOS through the strong and permanent silane interactions. Subsequently, heat treatment leaves a very rough silica surface where before the surface was smooth. The size of pores can be controlled by rough correlation with the size of the organic precursors used in the synthesis.

Alternatively, a micelle can be used whereby an organic silane precursor is bound electrostatically to the micelle, producing a hollow sphere with a very well-defined mesoporosity on the surface or on the inside (or both). Synthesis via this method resulted in BET surface areas near 1000 m^2/gm with average pore diameters of 2-3 nm despite having average particle diameters of 200 nm. This particular synthesis method seems particularly adaptable to the phage nucleation techniques developed in our lab due to the electrostatic interactions with what is essentially a micelle around the phage. Further, by incorporating metal atoms into the organic molecules, heterogenous catalysts with very high dispersions can readily be produced.

2.1.4 Colloidal Catalyst Syntheses

Colloidal syntheses are very varied, and discussed extensively in other subsections of this thesis. Thus, this subsection will be fairly short. Colloidal syntheses are broadly described as syntheses wherein a solid is precipitated from a solvent-soluble precursor into a solvent-insoluble solid nanoparticle mixture.

In the case of forming catalysts, precipitation is typically desirable so that a dry material can be handled; however, in many non-catalyst cases stabilization of the colloidal suspension is necessary. The force of attraction between two particles is inversely proportional, roughly, to the square of the distance between particles. Thus, stabilization can be accomplished by the use of either a steric, or an electrostatic barrier.

Electrostatic stabilization can be thought of as a method by which the surface of the nanoparticles are all given a strong enough charge that electrostatic repulsion overwhelms van der Walls attractive forces at moderate distances, preventing them from becoming close enough to collide. At appropriate pH, an electric double layer will form on the surface of the nanoparticle. At pH close to the isoelectric point given by a zeta potential measurement, the nanoparticles will become on average neutral, and will no longer electrostatically repel each other.

Steric stabilization is when long organic molecules coat the surface of the material, presenting a surface which is exceptionally soluble in the solvent of interest. This coating makes the particle dissolve more easily in the solvent, and prevents agglomeration by physically isolating the surfaces.

Generally, metallic clusters are formed by reducing metal ions in solution with an agent such as hydrogen or sodium borohydride. The reduced metal ions become zero-valent, losing their electrostatic repulsion, and are able to nucleate nanoparticles of the neutral metallic material. If this is done in the presence of a ligand that binds to the metallic material, such as a thiol with gold, this

can simultaneously provide steric stabilization to the nanoparticle.

Microemulsions

A related method is the use of a microemulsion. In this system, micelles are used as "nanoreactors" where the inside of the micelle is hydrophilic in a hydrophobic solvent. The metal precursor is then dissolved in the hydrophilic liquid inside the micelles, creating a very small volume of isolated precursor. Another microemulsion is made, containing the reducing agent.

When these two microemulsions are mixed, as micelles collide, their contents mix, forming nanoparticles out of a very small, and quite well-defined volume of precusor. The result is an exceptionally narrow size distribution for particle sizes.

The downside of this method is that minimum particle sizes are dictated by the minimum stable micelle size, typically well over 5 nm.

Metal Complex Decomposition

Metal nanoparticles can also be formed via decomposition of unstable metal complexes such as organometallics. This can be accomplished via a variety of methods such as heating, acoustic cavitation, electric current, or light exposure. In this case, there is no chemical reaction occurring between the precursors and a reducing agent. Instead, very small nanoclusters are forming transiently, or permanently in the case of metastable precursors, due purely to decomposition.

Gas Phase Synthesis

A more extreme alternative is the direct use of metal vapor with ligands in low concentrations. By rapidly quenching the dilute metal vapor on a liquid nitrogen cooled target, the metal rapidly nucleates solid particles in a high vacuum. The resulting particles are desirable in some situations due to the extremely high purity achieved with no solvent in the system. However, the particle size distributions can be fairly large.

High-Gravity Reactive Precipitation

By spinning the reacting solution in a centrifuge and drawing off products from the end, mass transfer can be significantly increased. Due to shear fields, formation of fine droplets, and thin films formed in the centrifuge, very interesting materials can be produced. However, this is a very new, and as of yet poorly understood synthesis technique.

Electrochemical Synthesis

This synthesis method involves the use of a sacrificial anode of the metal of interest. As current flows, metal ions dissolve into the electrolyte, diffuse to the cathode due to electrostatic interactions, and

nucleate particles on the surface after being reduced by the electrons on the cathode. In this case, particle size can be controlled by manipulating the electrode distance, reaction time, temperature, polarity of the electrolyte, and current density.

2.1.5 Microwave-assisted Synthesis

Microwave radiation has a frequency of particular interest in nanoparticle synthesis. The response of a material to microwaves is dependent on the ability of a material to change local charge configuration, and the energy loss when this happens. These two variables are termed the dielectric constant, related to the polarizability of a molecule, and the dielectric loss, which is proportional to the amount of energy converted from microwave radiation to heat per cycle at a constant frequency and field strength.

Most metals are microwave reflectors, meaning that radiation is only absorbed in a very small surface layer. The thickness of the surface layer is called the "skin depth". This depth decreases as frequency increases, and as conductivity increases, meaning that microwaves penetrate less into materials which are highly conductive. This can be desirable in the case of catalyst manufacture where one may wish to limit reactions to the surface of the material. Microwave heating is also extremely efficient for this reason, as only the areas of interest are actually being heated.

An example of a microwave-assisted synthesis is in the production of nanolayer carbide and nitrides on the surface of metal catalysts. Carbides and nitrides are frequently active as catalysts and may be used as a substitute for metal catalysts in some applications. For example, Mo_2C may be used as a catalyst for the water-gas shift reaction used to convert carbon monoxide into hydrogen and carbon dioxide in the presence of water. It has also been suggested that the use of carbon-modified tungsten may be used as a catalyst in direct methanol fuel cells due to improved carbon monoxide tolerance.

In this process, approximately 5 gm of commercial metal powders with particle sizes of approximately 1μm are fluidized in a quartz tube. After about 10 s of irradiation the material surfaces become high enough to react with the nitrogen used to fluidize the powder. After a few minutes, Cr_2N begins to form, and after analysis it shows clear XRD peaks. After shorter times, Cr_2N is not visible in XRD analysis, but peaks are visible in EDS, showing the presence of the nitride compound on the surface of the particles.

Another method is to fluidize metal along with carbon black in argon. This particular synthesis method is particularly appealing from a phage catalyst standpoint. For carbide catalysts, phage display provides an interesting way to incorporate the carbon into the material — nanowires of the metal can be synthesized using standard methods, and the dried powder of highly homogenized metal or metal oxide with carbon may be transformed into a desirable carbide. Similarly, genetic engineering may be used to display a larger number of particular elements on the surface. For

instance, by engineering a phage with four cysteine amino acids displayed on p8, it may be possible to synthesize a metal sulfide on the surface of the phage via microwave heating.

2.1.6 Dendrimer-Metal Precursor Methods

An alternative colloidal synthesis method is possible using a dendrimer as a sort of nanoreactor, similiar to the use of a micelle to encapsulate a growing nanoparticle. Dendrimers are branched polymers, made of units which have one active site on one end, and two active sites on the other end such that the single active end will bond to either of the active sites on the double site side.

The result is that the polymer grows in a "tree" fashion. Steric hindrance of adjacent chains eventually cause the dendrimer to fold back on itself into a spherical single molecule. By careful selection of the side groups of the dendrimer tree, the "inside" of the dendrimer sphere can be made to attract metal ions in solution, similarly to a micelle, or to poly-electrolyte multilayers where nanoparticles are synthesized inside of the polymer.

After metal ions are complexed with the dendrimer side groups, forming a metal-dendrimer complex, reduction causes the complex to collapse, forming a nanoparticle with a fairly narrow size distribution inside of the dendrimer. The number of atoms in the nanoparticle is roughly related to the number of available complexing sites in the dendrimer, and this process is frequently not immediately destructive to the dendrimer itself.

Subsequently, the entire dendrimer-metal nanocomposite is deposited onto a porous supoprt and the dendrimer is then removed either by heat treatment or chemical means. Due to the steric hindrance of the dendrimers, individual nanoparticles are unable to come close to each other, resulting in very good dispersion on the support. However, there is no substrate trapping of the metal nanoparticles, so they can in principle be removed more easily than the case of a cogelled catalyst. Additionally, support adhesion can be enhanced for the dendrimers through the use of functionalization, although simple wet impregnation and sol-gel incorporation work as well.

A primary difficulty in dendrimer synthesis methods is that complexation must be absolutely complete, or else residual metal ions in solution will form nanoparticles outside. This will result in poor monodispersity.

The use of dendrimers can also be used to form core-shell nanoparticle structures through stepwise synthesis. After initial reduction and formation of a "core" nanoparticle, the dendrimer can be complexed with a second metal. After a second reduction step, this may result in a structure where the second metal fully coats the first metal. Formation of a bimetallic nanoparticle can also be accomplished via co-complexation (complexing the dendrimer with multiple metals), or partial displacement (substitution of a second metal for the original nanoparticle material).

Dendrimers, if left on the nanoparticle, will block access even to gas molecules due to covering of the metal sites by collapsed ligands. However, in liquid phase, the active sites may be accessible

if the dendrimer is not collapsed. The most straightforward way to remove the dendrimers is by heat treatment, typically at 400-500°C. However, this method may result in undesirable sintering or segregation of bimetallic nanoparticles. To avoid this, other methods such as chemical leaching of the dendrimer or plasma treatment can be used.

2.2 Particle Size

From knowledge of kinetics, we can guess that there are five primary rates present in the system which govern initial particle formation, initial particle growth, and particle aggregation. In the case of pyrolysis of a metal precursor, these are:

1. Rate for converting the metal precursor to the oxide in the vapor phase.
2. Nucleation rate for forming a small nanoparticle cluster of oxide in a crystalline solid phase.
3. Growth rate for adding a new unit of oxide onto the nanoparticle surface.
4. Diffusion rate of the vapor phase oxide to the surface of the particle.
5. Aggregation rate for two nanoparticles colliding and forming a larger secondary aggregate.

Of these, we can make some inferences as to the overall trends based on some assumptions about these rates. First, we can assume that the rate for converting the metal precursor to the oxide is rate limited by either the availability of water, or the precursor (i.e. that the decomposition of the precursor happens immediately upon contact with water).

At very high concentrations of metal precursor, although all the water produced by the flame is immediately consumed, the net oxide produced is small (fuel limited). At very low concentrations of metal precursor, although all the precursor is consumed, the net oxide produced is small (precursor limited). In between these two extremes, there is a region where the amount of oxide produced per unit time for a given flow rate is maximized.

Next, the nucleation rate for forming solid metal oxide nanoparticles is generally a function of what the most stable thermodynamic phase of the material is at the temperatures of interest, and the driving force to nucleation is proportional to the degree of supercooling of the material. In the case of silicon oxide, this material melts boils at roughly 2230 °C and melts at 1650 °C, while the temperature of a hydrogen/oxygen flame can be as high as 3000 °C. At temperatures above the boiling point of silicon oxide, there is no thermodynamic driving force towards nucleating nanoparticles, so the temperature used in the pyrolysis technique must be far less than the maximum for a hydrogen/oxygen flame.

Assuming that we operate beneath the melting point, and that due to there being no other surfaces that homogeneous nucleation is the dominant mechanism, moving from the vapor phase will have a very large specific driving force due to both the massive undercooling competing with the energy required to change phase twice as well as form the surface area for the nanoparticle.

49

Most likely, in the case of high melting point compounds such as silica, solid oxide nanoparticles are formed almost immediately, and the nucleation rate can be assumed to be extremely high.

The growth rate for adding a new oxide molecule to the solid nanoparticle is limited at the surface by the requirement of forming a commensurate lattice. The delay required to find the proper conformation to add a cell is the limiting factor on the growth rate in terms of reaction. However, diffusion is frequently the rate limiting step in growth. As the oxide nanoparticle forms, it depletes the area immediately around it of material, and growth is diffusion limited. In the case where nucleation is extremely fast, particles may have all formed before diffusion has a chance to occur to a meaningful degree. In this case, the nanocrystal size is typically extremely small. This can be accomplished by limiting the concentration of metal oxide in the system, as well as by operating at low temperature to encourage rapid nucleation.

In the pyrolysis system, the concentration of metal oxide on a volumetric basis is fairly low because it starts in the gas phase, and so as long as the temperature of the reaction is fairly low, nanoparticles with a size of less than 7-40 nm should be readily achievable. However, in that size regime, decreasing the availability of the oxide is the most important factor in limiting growth relative to nucleation, so operating on either side of the conversion rate curve (preferably on the excess fuel side) will produce smaller nanocrystal sizes.

Last, aggregation rate is going to be primarily a function of the probability of collision between particles. The probability of a collision when all other rates are held constant is approximately proportional to the probability of two particles occupying the same volume in the space (ignoring multiple aggregations in this simplified proportionality model). This probability rate will decrease for low concentrations of particles and for low temperatures (decreased particle RMS speed), but even more fundamentally, regardless of the probability rate the residence time will dramatically affect aggregation rate.

For a given probability rate of collision, a shorter time in the collision region means fewer collisions; thus, assuming that nanoparticle nucleation is rapid relative to aggregation rate, the smallest aggregation of particles will occur at the shortest residence time that allows nanoparticles to fully form.

For colloidal and other liquid based syntheses, there are equivalent rates governing the nucleation, growth, and aggregation kinetics. However, an additional effect can take place in solution due to diffusion from the surface of particles. By applying a mean-field approximation to the system, one can assume that at a short distance from each nanoparticle the concentration in solution is a constant sink or source. Nanoparticles with a very small size have a large curvature, resulting in a large number of uncoordinated atoms at the surface. These atoms result in an increased surface energy, and thus an increased concentration of material in the solution directly next to the particle in equilibrium. This results in a diffusion gradient which tends to result in small nanoparticles

dissolving into the mean field while larger nanoparticles absorb the material added to the solution. This effect is called Ostwald ripening. Over time, this results in the average nanoparticle size increasing as large nanoparticles grow larger and small nanoparticles disappear.

2.3 Forming Supported Catalysts

2.3.1 Surface Density

Surface density is defined generally as the ratio of active metal oxide surface area to underlying support surface area. The overall catalytic properties of a supported metal oxide is dependent largely on the surface density, typically in one of several different nanoscale structures.

An extremely common catalyst manufacturing method is impregnation. This involves wetting a solid high surface area support with a liquid containing the catalyst precursor. Subsequently, nanoparticles are formed via any of the above discussed methods, which are then loosely bound to the surface of the support, largely mechanically.

A second method of manufacture is "equilibrium adsorption" or "ion exchange", in which after a long time the metal ions in solution electrostatically or chemically bind to the surface of the support, followed by a nanoparticle synthesis step. This method generally results in a better dispersion of catalyst material on the surface.

The other primary catalyst manufacturing method is via coprecipitation, which is the technique used in this research. In this method, a solid is precipitated from a solution containing the precursors for all catalyst materials and supports, followed by precipitation, and finally washing and drying of the resulting loose powder. This manufacturing method was chosen as the method of choice for this work because it results in much better interaction between the support and any active species; ceria is necessary for the activity of rhodium and nickel, so support-catalyst interactions are critical.

In coprecipitation, the rate of addition of precipitating agent is critical. Slowely added precipitating agent results in a temporally distribution of the materials in the system, with the least soluble materials precipitated first. The final result is an inhomogeneous powder. However, rapidly added precipitating agent, as is done in this work with ceria, rhodium, and nickel, results in a much more uniform and homogeneous nanostructure.

2.3.2 Calcination

Calcination is generally the process of heat treating the catalyst material at high temperature under various atmospheres (oxidizing in the case of ceria, rhodium, nickel catalysts). This process volatilizes ligands and other non-oxide secondary phases, resulting in a clean oxide surface. It also allows for the conversion of secondary products such as $Ce(OH)_2$ into CeO_2 and likewise for $Ni(OH)_2$. Counterions

such as nitrogen, hydrogen, and carbon are frequently easily volatilized in this way, which should allow for the easy removal of the majority of the organic material of the phage.

Unfortunately, halides, phosphates, and sulfides are generally not removed in calcination. Phosphates are present in the DNA backbone of the phage, and sulfides are present in some proteins (cysteine and methionine). It is unclear if sulfides and phosphates will impact the catalytic activity of the particular ethanol reforming system proposed in this work, but they may very well promote, or act as a poison in the final catalyst. It may be necessary for any particular system to find a way to chemically leach out any residual sulfides or phosphates in the catalyst material.

Calcination is critical in opening up the micro and mesoporous structure of the catalyst material; otherwise organic compounds may block the pores and result in highly reduced active surface area available for catalysis. Calcination can also result in recrystallization of both the bulk catalyst and the surface face exposed, both of which can substantially impact catalytic activity.

2.3.3 Molecular Surface Structure

There are five different primary molecular structures which the surface of a catalyst can have:

1. Isolated — where each supported oxide is fully independent chemically.
2. Oligomer — where adjacent supported oxides have additional bonds between each other.
3. Polymer — where adjacent supported oxides both have additional bonds between them, and are bound to the same surface atoms.
4. Polymer + Nanocrystallite — where a polymerized surface has single-phase nanocrystallites of the polymer base material attached to the support through the polymerized surface.
5. Bulk Crystal — where a single additional phase is bound to the support directly through covalent bonds to surface oxygen, without a surface species in between.

Typically, isolated structures appear at very low concentrations of surface oxide. As surface oxide concentration increases, bridging M-O-M bonds are frequently formed, producing an oligomeric species. As the concentration increases further, this will eventually form a polymeric species. Under appropriate conditions, where the surface oxide concentration is too large to support in a monolayer, or the surface energy is too high and adhesion between layers is poor, a second crystalline species will form, either as a nanocrystallite or as a bulk crystal.

2.3.4 Solid-state Ion-Exchange with Zeolites

Ion exchange can be used in the solid state, as well as the liquid state to impregnate a zeolite with catalytic materials. During the ion exchange process, cations from the solution replace cations in the zeolite. Solid state ion exchange occurs when the substituting cations are sourced from a solid material, frequently forced into the structure via mechanical grinding as in a ball mill.

Solid-state ion exchange has the advantages of higher metal loadings, higher accessible exchange temperatures, elimination of solvent interactions, and reduction in necessary postprocessing such as drying and heat treatment. This sort of solid-state ion exchange should be possible to accomplish with other ionic solids beyond zeolites.

In some cases, a small amount of moisture is introduced to enhance mass transfer. Alternatively, high temperatures or direct chemical reactions can be used to drive the ion-exchange process.

2.3.5 Strong Electrostatic Adsorption

Electrostatic adsorption can be used as an alternative for dispersing material onto a support. In this technique, the surface of the support is charged via careful manipulation of pH. Materials such as alumnia, which can have very low isoelectric points (point of zero charge), at high pH are very highly negatively charged on the surface. This surface charge allows the material to readily electrostatically attract metal cations in solution. Alternatively, on a high isoelectric point material, anions can be bound very rapidly at low pH.

2.3.6 Direct Deposition and Precipitation

The method of direct deposition and precipitation is based on sol-gel and colloidal syntheses in solution to provide the final supported catalyst form. In order to cause precipitation to occur exclusively on a support surface, there must be an interaction between the metal precursor and the surface, and the concentration of the precursor concentration must be low enough to avoid precipitation in solution.

In order to avoid supersaturation of the solution locally, precipitating agent must be added very slowly to the solution. Alternatively, urea may be used as a delay-base. Urea can be mixed with the precursors, and upon heating to 60°C will hydrolyze into ammonia hydroxide and produce a gradual rise in pH.

Noble metal catalysts can also be made this way by gradual addition of a base after mixing a noble metal precursor with the support. Raising the pH is done using a base like NaOH, and subsequent aging results in metal hydroxide particles forming on the substrate.

Another method to gradually increase the concentration of a metal precursor is by dissolving in a volatile solvent and allowing the solvent to evaporate, for example with ammonia.

2.4 Controlling Catalyst Distribution in a Support

Catalyst particle distribution on a support can have a significant impact on the final properties. Catalyst may be primarily located at the surface of the support, called an "egg shell". It may also be located at a shell inside the support, called an "egg white". Catalyst located primarily at the

core of the support is called an "egg yolk" distribution. Each of these distributions has advantages and disadvantages — for example, an egg white distribution may be desirable to improve selectivity for a rapidly occurring reaction, while an egg yolk structure may be desirable in cases where one wants pore size to play a dominant role in the reaction kinetics.

Effects of Impregnation on Catalyst Distribution

Incipient wetness impregnation or dry impregnation can be used to control the catalyst distribution. By adding an amount of solvent very close to the total pore volume of the support, all of the solvent is rapidly taken up into the support. Subsequently soaking in the precursor dissolved in the same solvent results in the diffusion-limited spread of catalyst material into the support. Because diffusion of the precursor in liquid is slow when there is no flow, this can allow for the production of egg shell structures. A typical estimate of the time scale of complete diffusion into the entire pore system is on the order of 10 hours, allowing for straightforward and repeatable distributions to be produced.

Further fine-tuning of the structure can be provided by the use of a dissolution agent. In this case, a support's pores are filled with pure solvent initially. Catalyst precursor in solvent is applied to the catalyst for several hours, allowing the concentration front to reach a desired depth in the material. Finally, the support is exposed to an acid such as nitric acid. The acid either reacts with the support surface to prevent adsorption, or lowers the pH to prevent growth of catalyst particles near the surface upon drying.

The primary features which dictate the impregnation degree of coverage is dictated by the pH of the impregnating solution, point of zero charge of the support, and the chemical nature of the catalyst precursors. For example, with a highly negatively charged support surface, cations in solution will readily adsorb onto the surface. If the pH is below the point of zero charge, metal will stay in solution until dried, resulting in a flow dictated profile. However, if the pH is above the point of zero charge, the metal will deposit on the support immediately, and drying will have only a limited effect on the metal distribution.

Although the binding strength to the surface during impregnation doesn't necessarily immediately affect the catalyst distribution, it can dramatically change the modifications to the distribution upon drying by modifying the interplay between local nucleation on a surface and diffusion elsewhere in the liquid. The more strongly bound the catalyst precursor is to the surface of the support, the less tendancy there will be for it to migrate to the surface during drying.

This also lends itself well to phage technology. By using an alumina binding p3 protein with an E3 phage, it is possible to very strongly bind metal or metal oxide nanowires to the internal pores of an initially low surface area catalyst with pores large enough to accomodate several phage without becoming clogged.

Effects of Drying on Catalyst Distribution

Drying can also impact the final catalyst distribution on the support. Drying can take place by several routes — movement of liquid to the external surface, movement of water vapor to the external surface, and by movement of water adsorbed on the internal surfaces of the support.

In "constant rate drying", the evaporation rate from the external surface is slow compared to internal transport, so this rate fixes the drying rate of the entire material. Internally to the material, capillary forces rapidly transport solvent to the surface, and when the internal transport slows, the surface begins to dry. Overall, the constant rate drying region usually results in 90% of the liquid being removed.

The second stage is called the "first falling-rate period" during which the rate of drying steadily decreases in a roughly linear fashion. In this region, the rate of drying is primarily limited by the remaining wet external surface area. This can also be interpreted as being limited by the amount of solvent being internally transported to the surface being the limiting transport step. In this stage, the drying rate can be roughly estimated by taking the original drying rate and multiplying by the fraction of the surface still wetted.

The final stage is called the "second falling-rate period". During this stage, drying rate falls more gradually until the moisture content is eventually reduced to zero. This region can be interpreted as the evaporation front receding into the material from the surface. The surface is essentially entirely dry at this stage, but there is still moisture inside the support, evaporating internally and being transported as a vapor to the surface. In this phase, the drying rate is limited by the transport of water vapor to the surface, which in terms of mass is much slower than liquid transport (although volumetric transport is higher). In the case of highly porous materials such as catalyst supports, the two falling rate periods merge into one region of steadily decreasing drying rate in which drying rate fall decreases in speed as the moisture content drops.

There are three primary regions of flow which determine which mechanisms are most active. In the region of pore sizes of macroscopic dimensions (0.2-2.0 mm), capillary and gravitational forces dominate flow mechanics. This results in most of the moisture being removed during hte constant drying region. In the region of pore sizes of microscopic dimensions (2-20 μm), capillary forced dominate transport, but the pores are large enough that frictional forces are minimized. In the region of pore sizes smaller than 2 μm, capillary forces are dominating flow, but frictional forces are playing an increasingly dominant role in resistint flow. In the case of high viscosity solvents, this can significantly limit transport, but in the case of low viscosity solvents (as in the case of aerogel production), evaporation can now outpace transport to the external surface, resulting in internal evaporation.

The distribution of catalyst as a function of drying method is significant. In the case of supports where the majority of drying occurs in the constant rate region, drying is occuring exclusively on

the external surface of the support. This results in most of the dissolved precursor forming catalyst species on the external surface of the support. During the first falling-rate period, more of the dissolved catalyst will be deposited internal to the support, resulting in an increasingly uniform distribution.

Deposition at the center of the support will begin to occur in the second falling-rate period, when internal evaporation and transport of water in the vapor phase is dominating drying. In this region, the catalyst particles precipitate as the solvent dries internally, and so are deposited internally. In this period, catalyst on the surface may also back-diffuse towards the center of the support due to diffusion in the liquid phase. However, if the liquid phase is not continuous from the surface to the core, this diffusion is suppressed, and sharp egg shell structures can be formed.

At the limit of extremely slow surface evaporation, other distributions may be encountered. For example, if the rate of evaporation from the surface is slow compared to the precursor diffusion rates, the precursor may diffuse to the center of the support instead of depositing on the surface, not forming precipitated particles until reaching supersaturation at some point inside the support. This method may be used to provide a uniform distribution of catalyst in the support, or possibly even an egg yolk structure.

The temperature of drying can also be used to modify the relative strengths of the different transport mechanisms. For instance, drying at low temperature may result in a mostly evenly distributed catalyst with some increase at the surface. At moderate temperatures, heat and mass transfer rates increase, leading to higher evaporation rates, and greater inhomogeneity in the profile towards the surface. At high temperatures, diffusion becomes more active at the surface, and back-diffusion can cause a thicker egg shell on the outside of the catalyst.

Larger overall catalyst pellets experience less back-diffusion than small pellets, so if a very small particle size of support is used, the extent of the surface catalytic layer may be larger than for a larger pellet where the catalyst concentration gradients are less pronounced.

2.5   Summary

In summary, there are a great many different methods currently in use for synthesizing catalysts. Some of these, such as functionalized wet impregnation, seem exceptionally well suited to use with phage technology. Others, such as flame pyrolysis, seem fairly unlikely to be used in conjunction with phage.

Of particular interest are catalysts in which carbon, nitrogen, phosphate, or sulphur contamination is desirable. In these systems, it may be possible to produce interesting carbide, nitride, and other ceramic catalysts directly by phage templating and subsequent heat treatment. Additionally, phage binding affinity lends itself particularly well to any functional synthesis where metal com-

plexes are used to form the final catalyst. Finally, the ability to form gels of phage bound metal has already been established; solvent exchange and supercritical drying could allow for the formation of true aerogels based on phage nanowires.

Although the work done here is limited to coprecipitated powders, this is because of the very high level of sophistication already present in simply making the catalytic nanowires. After nanowires are made, and are shown to function to some extent in a fixed bed reactor, further advances such as functionally impregnated supports or aerogels may enhance the actual performance of the final catalyst by many times over again.

Chapter 3

Development of Base Materials

The first step in producing these catalysts is to fully understand and master the synthesis of the base materials — CeO_2, Rh_2O_3, and NiO. Further, the syntheses must all be biocompatible, and ideally be similar enough that they can be done simultaneously instead of being done in multiple stages.

3.1 CeO_2 Synthesis.

The first step towards this nano-structured catalyst is to prepare and characterize CeO_2 nanocrystals in order to find binding peptides. Using a modified version of the method used by Yamashita, CeO_2 nanocrystals were successfully produced, and the process has been improved in order to give nanocrystals with an average, tunable size as low as 1.2 nm as measured by XRD, and 2.2 nm as measured by TEM. [52].

The original synthesis by Yamashita called for 1 mol $CeCl_3$ in addition to $CaCl_2$. As no Ca is needed in this system, only $CeCl_3$ was used. 1 mol of $CeCl_3$ also produces an excessive amount of product, so the reaction was scaled back to use only 10 mmol of $CeCl_3$.

$CeCl_3$ is dissolved in water under stirring at $40\pm1°C$. Subsequently, a solution of H_2O_2 and NaOH was added rapidly to cause the formation of $Ce(OH)_3$ and immediate oxidation of $Ce(OH)_3$ into CeO_2 nanocrystals. As different amount of H_2O_2 are added to act as an oxidizer, an immediate and stunning color shift is seen (Fig. 3-1). As the particles dried, they became more pale, but much of the color remained (Fig. 3-2).

To characterize the change, the following reaction was developed in order to produce nanocrystals for characterization.

1. 100 mL of 100 mM $CeCl_3$ solution is stirred and allowed to equilibrate at $40\pm1°C$.

2. A volume of H_2O_2 is set aside.
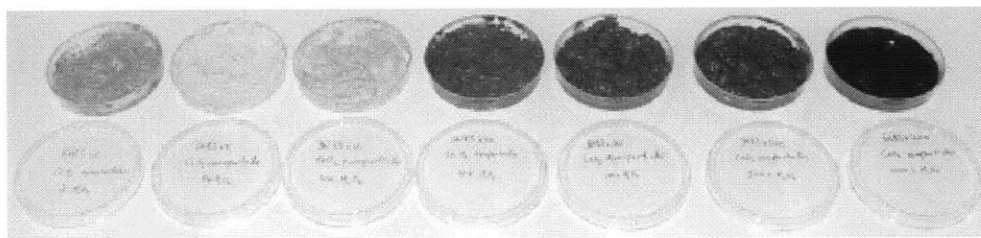
Figure 3-1: As the H_2O_2 concentration increases, the resulting nanocrystals change in color from pale yellow-blue to dark red-orange. From left to right, 0.058, 0.29, 0.58, 2.9, 5.8, 29, and 58:1 ratio of H_2O_2:$CeCl_3$

Figure 3-2: As the CeO_2 nanocrystals dried, they became lighter in color, though still much darker than reported elsewhere. From left to right, 0.058, 0.58, 5.8, and 58:1 H_2O_2:$CeCl_3$ ratio.

3. Millipore water is added to 100 mL of 300 mM NaOH solution to bring the final volume after H_2O_2 addition up to 150 mL.

4. 30 wt% H_2O_2 is added to the NaOH solution, and the new solution is added rapidly to the stirring $CeCl_3$ solution.

5. Solution is allowed to react for 60 minutes.

6. Supernatant is removed by centrifugation, precipitate is washed with millipore water to remove any remaining NaCl, and centrifuged again.

7. Supernatant is discarded and precipitate is dried in air at room temperature.

The values for each of seven samples is outlined in Table 3.1. The samples are shown after the second precipitation in order from left to right in Fig. 3-1.

Samples made with 0.058:1 and 0.29:1 H_2O_2:$CeCl_3$ ratios both were a pale blue-purple both during reaction and after precipitation, suggesting a similarity in properties to the particles synthesized in low surfactant concentrations by a reversed micelle method [46]. However, all reactions carried out with higher concentrations of H_2O_2 immediately became a yellow, orange, or red color. Upon drying, both the 0.058 and 0.29:1 H_2O_2:$CeCl_3$ samples became pale yellow and upon subsequent addition to water did not regain their blue-purple color as shown in Fig. 3-2.

The elimination of the blue-purple stage of reaction as oxidizer concentration is increased suggests that the precursor to oxidation, $Ce(OH)_3$ is causing the blue-purple color. In the case of higher oxidizer concentrations, the $Ce(OH)_3$ is mostly oxidized to form CeO_2 while samples with lower oxidizer concentrations are gradually oxidized in air as they dried. Thus, it is possible that the color changes observed by Masui were not caused by particle instabilities from low surfactant concentrations, but instead by the presence of $Ce(OH)_3$.

However, upon heat treating the particles at above 100°C in an attempt to completely dehydrate the particles of any residual hydroxyl groups, the particles all became a much more uniform pale yellow color, suggesting strongly that the color change is purely an effect of absorbed hydroxyl groups on the surface of the nanoparticles, and that the dark color present in the 58:1 H_2O_2:$CeCl_3$ nanoparticles is a result of higher surface area causing more sites for hydroxyl groups to be bound.

Overall, this suggests that with too low of a concentration of H_2O_2, the $Ce(OH)_3$ is not oxidized to start with, but that at very high concentrations of H_2O_2, the extremely high surface area caused by the ultra-fine particles (less than 2 nm) is resulting in more bound hydroxyl groups than in the mid ranges of H_2O_2 added.

The synthesis was also performed at a 100-fold reduced concentration of $CeCl_3$ to test the limits of the synthesis. Reducing the concentration of the precursor and corresponding reactants did not affect the appear to affect the properties of the output product in any substantial way.

$[H_2O_2]/[CeCl_3]$	$CeCl_3$	NaOH	30% H_2O_2	H_2O
0.058	100	100	0.05	50.0
0.29	100	100	0.25	49.8
0.58	100	100	0.50	49.5
2.9	100	100	2.50	47.5
5.8	100	100	5.00	45.0
29	100	100	25.0	25.0
58	100	100	50.0	0

Table 3.1: Sample Identifiers and volumes of each reactant in mL.

3.1.1 Nitrate Based Synthesis

It is possible that the presence of chlorine could cause modifications to the catalytic activity of the material through incorporation of chlorine into the CeO_2 matrix in the form of Ce-O-Cl. It is very unclear whether or not this is actually a problem, but to address the potential issue and provide a sample to compare directly with, the synthesis was modified to use cerium nitrate.

The synthesis is otherwise identical to the $CeCl_3$ based synthesis — $Ce(NO_3)_3$ is dissolved in water, held under stirring at room temperature, and H_2O_2 with NaOH is added rapidly during stirring. The resulting solution is identical in color to the similar synthesis made with $CeCl_3$, the powder is dried overnight at room temperature in air, and then heat treated at 200°C for several hours until the powder has become a yellow color.

3.2 Size Analysis

Each of the samples was analyzed using XRD and TEM. XRD data is shown in Fig. 3-3a. As can be seen, as the H_2O_2 concentration goes up, there is a clear trend of peak broadening indicative of nanocrystal size differences. Based on the peak broadening, samples made with a 0.058:1 H_2O_2:$CeCl_3$ ratio have an average nanocrystal size of 6.5 nm while samples made with a 58:1 H_2O_2:$CeCl_3$ ratio have an average nanocrystal size of only 2.2 nm. All samples show a clear CeO_2 fluorite structure.

Subsequently, TEM analysis was done to independently measure the average diameter of the CeO_2 nanocrystals (Fig. 3-4). As can be seen, lattice fringes are present, confirming the crystallinity of the nanocrystals (Fig. 3-5), while the average diameter of the nanocrystals calculated by measuring the maximum diameters of individual nanocrystals decreased from 6.2 for 0.058:1 H_2O_2:$CeCl_3$ down to 2.3 for 58:1 H_2O_2:$CeCl_3$, closely following the results from the XRD analysis (Fig. 3-3b). This demonstrates conclusively that an increase in H_2O_2 concentration causes a decrease in the average crystallite size while maintaining the crystallinity of the CeO_2 sample.

This new synthesis method provides an extremely straightforward and inexpensive way to produce extremely small CeO_2 nanocrystals. The minimum average nanocrystal size was $\sim$ 2.2 nm, with a small number of nanocrystals as small as 1 nm visible.
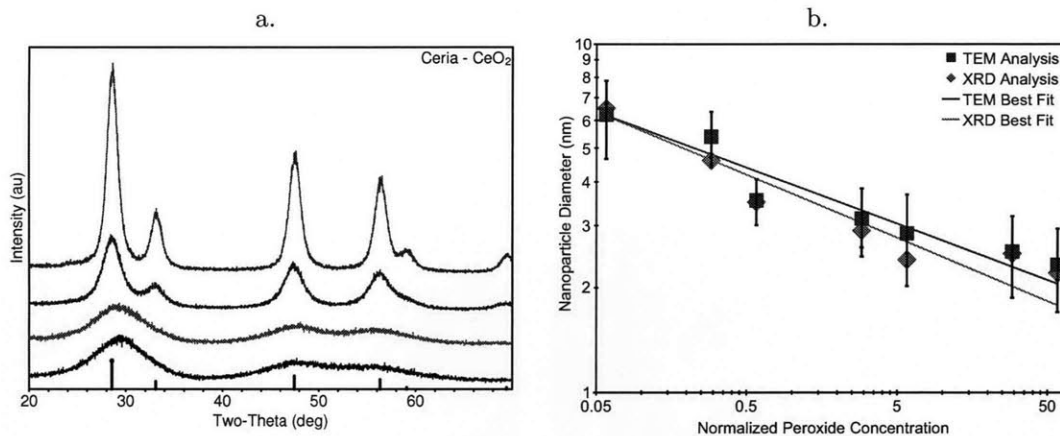
Figure 3-3: (a) Characteristic XRD spectra showing 0.058:1, 0.58:1, 5.8:1, and 58:1 H_2O_2:$CeCl_3$ during synthesis from top to bottom. (b) Sizes measured with TEM and with XRD compared and shown to have good agreement. At small crystallite sizes, the results diverge both because of the increasing inaccuracy of peak broadening to describe the ensemble size, as well as the increasing difficulty of imaging lattice fringes at small crystallite sizes.

Nanocrystal Size	XPS $V^O\%$	ANES $V^O\%$
3 nm	22%	
6 nm	15%	
6.1 nm		1.9%
7.4 nm		1.6%
10 nm		0.6%
15 nm		0.3%
30 nm	9%	
>5 μm		0%

Table 3.2: Data measuring the concentration of oxygen defects for CeO_2 crystals using XPS or ANES in literature [3, 4].

3.3 Oxygen Defect Concentration

3.3.1 Measurements from Literature

Previous work on analyzing the trends in oxygen vacancy concentration as a function of size gave the results in Table 3.2 [3, 4]. The larger numbers were calculated using X-ray photo-electron spectroscopy (XPS), while the smaller numbers were calculated using absorption near edge spectroscopy (ANES). Zhang *et al.* argue that due to the extensive time under vacuum and surface-bias from XPS analysis, the more modest values measured using ANES are more accurate than those from XPS.

Using the ANES data as a more conservative estimate, it seems that particles over 15 nm have a negligible concentration of oxygen vacancies compared to those smaller than 15 nm. 6.1 nm nanocrystals have a curvature 2.5 times greater than 15 nm nanocrystals.
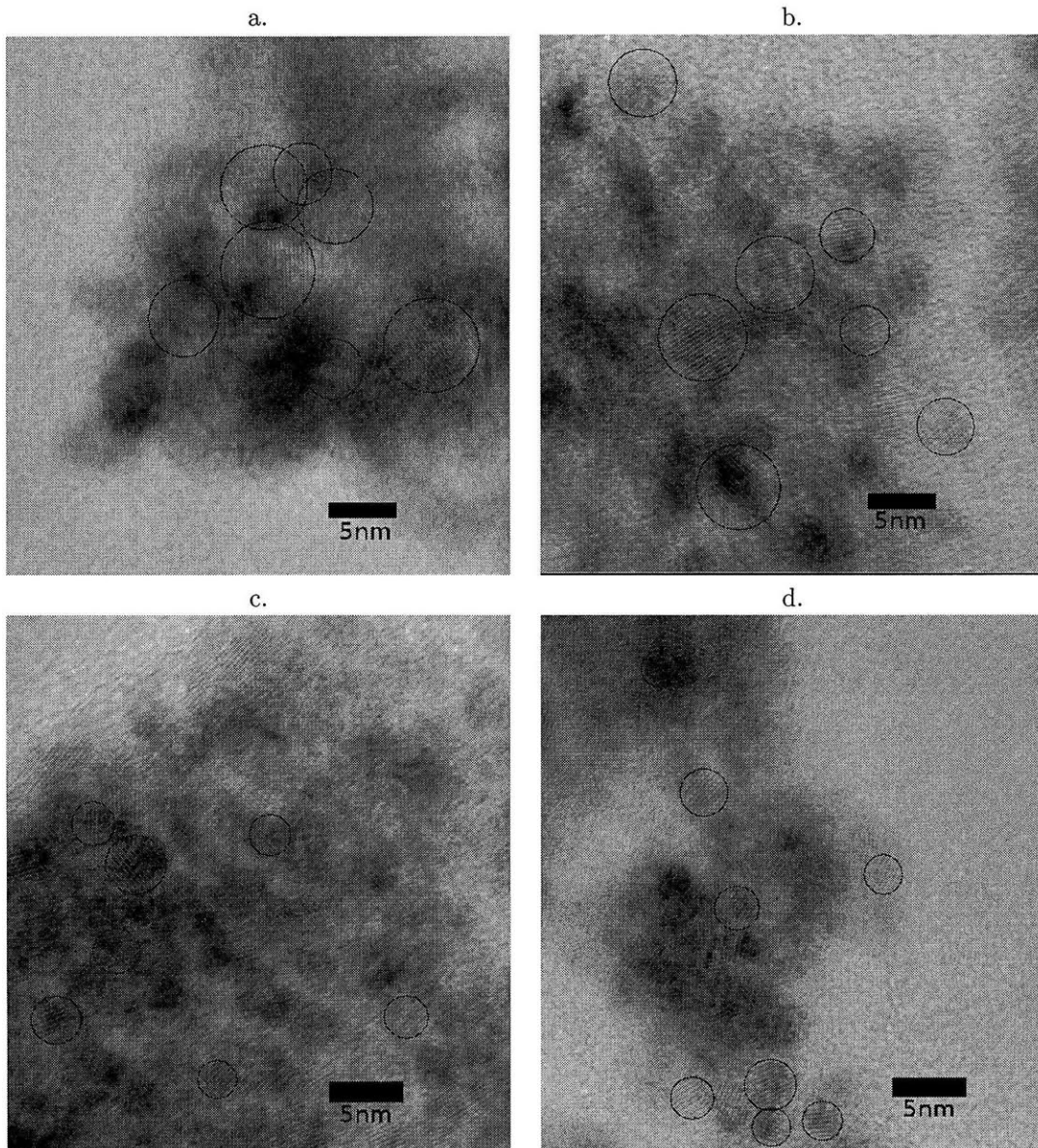
Figure 3-4: Characteristic TEM of the clusters of CeO_2 nanoparticles formed with varying amounts of H_2O_2. CeO_2 crystallites formed using a H_2O_2:$CeCl_3$ molar ratio of (a) 0.058:1 with an average size of 6.2 ± 1.5 nm. (b) 0.58:1 with an average size of 3.54 ± 0.5 nm. (c) 5.8:1 with an average size of 2.9 ± 0.8 nm. (d) 58:1 with an average size of 2.3 ± 0.6 nm.
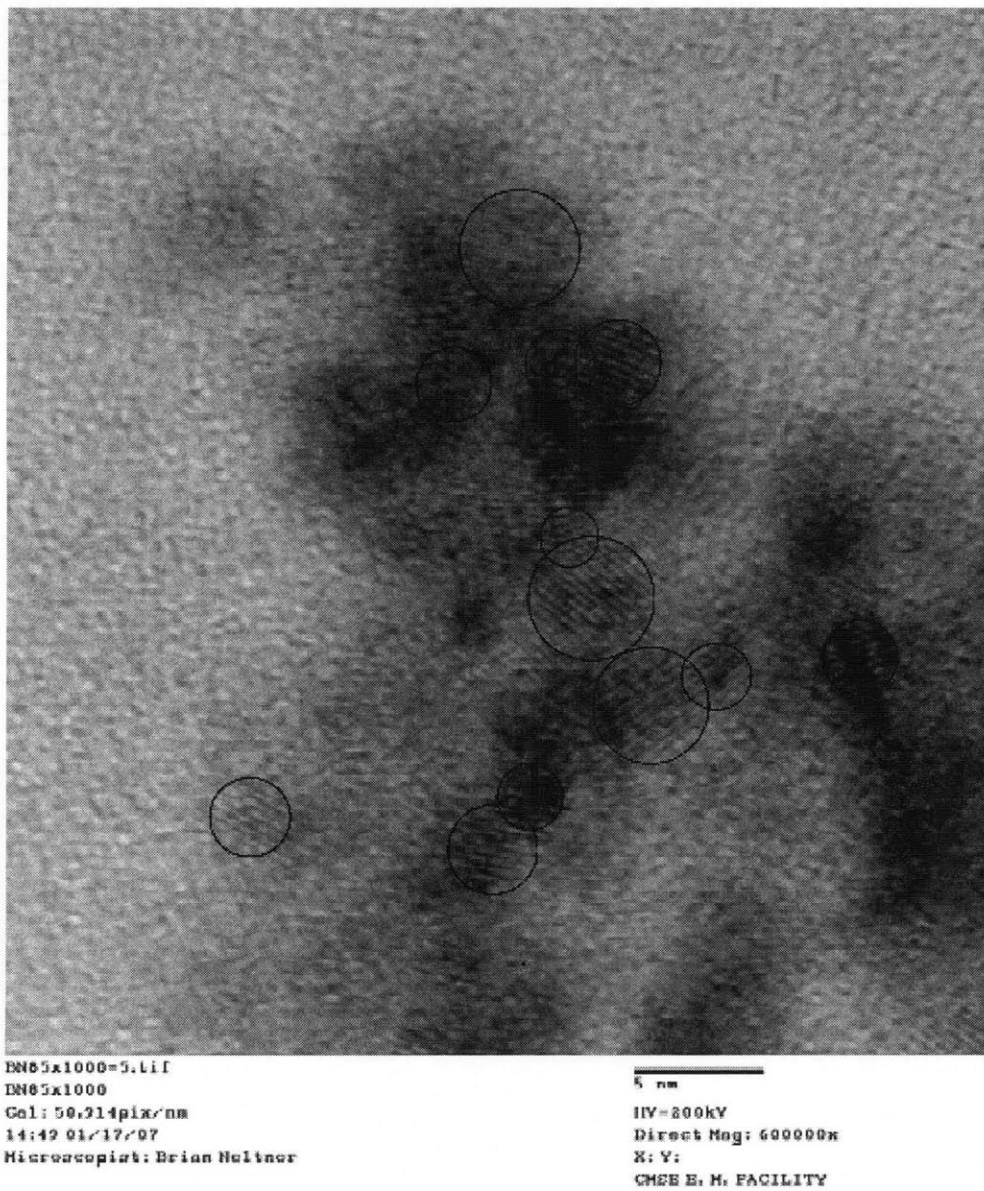
Figure 3-5: Representative TEM of 58:1 H_2O_2:$CeCl_3$ sample. Lattice fringes are clearly visible in particles all the way down to $\sim$2 nm.
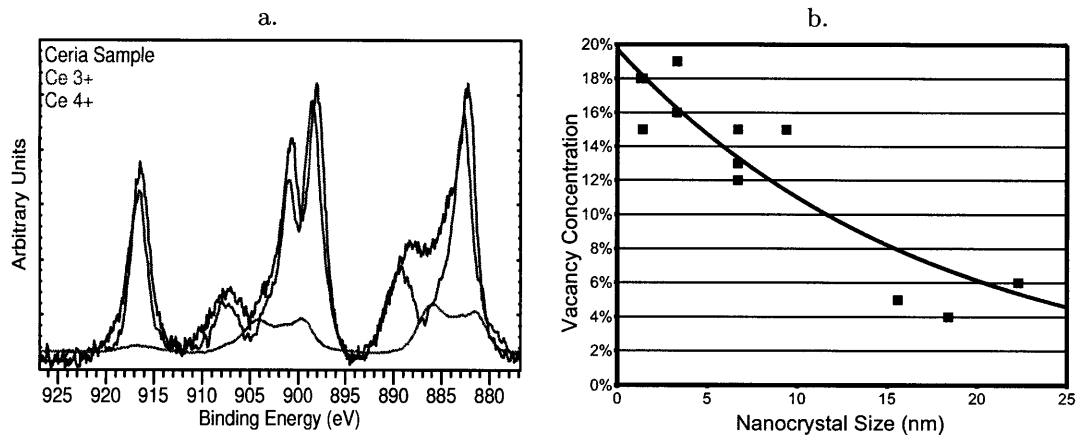
Figure 3-6: (a) Characteristic XPS spectra, as well as the fitted Ce^{3+} and Ce^{4+} principle components from which the oxygen concentration in the sample is derived. (b) Oxygen Vacancy concentrations as a function of nanoparticle size, showing the expected trend of increased vacancy concentration as particle size decreases.

3.3.2 Measurements

A measurement of oxygen vacancy concentration using XPS analysis combined with the CasaXPS software suite was performed, and the final data is, to our knowledge, the most complete done in a single experiment to date. Eleven samples were measured in the same XPS measurement round to ensure identical treatment of all samples and guarantee as much as is possible that there are no systematic errors in the relative values.

In ceria, each oxygen vacancy produces two atoms in the Ce^{3+} oxidation state instead of the typical Ce^{4+} oxidation state. Thus, by measuring the relative fractions of Ce^{3+} and Ce^{4+}, it is possible to indirectly measure the oxygen vacancy concentration in the material. [3,4,43–45,51,56,57]

Typically, this analysis is done by fitting a model of 10 peaks to the Ce 3d XPS peaks, 6 of which are associated with Ce^{4+} and 4 of which are associated with Ce^{3+}. [3,4,43–45,51,57] However, we found this analysis to be impossible to do repeatably, with the initial positions and shapes of the peaks dramatically effecting the corresponding oxygen vacancy concentration measured, regardless of the extent to which we constrained the positions of the peaks.

To alleviate this problem, we used principle component analysis (PCA) to reduce the number of independent variables to be optimized from 30 to 2 using the techniques outlined by Holgado *et al.* [56] Using the principle components kindly provided to us by Holgado in private correspondance, a reliable and repeatable estimate of the oxygen vacancy concentration was achievable (Fig 3-6a). The results of this analysis are shown in Figure 3-6b as a function of nanoparticle size, showing a trend towards increased oxygen vacancy concentration as particle size decreases.

The functional form of the trend is impossible to determine from this data, but it is known that the oxygen vacancy concentration asymptotes to ~ 0 in the bulk phase. Thus, fitting a simple

exponential model asympoting to zero gives the form

$$[V^O] = 19.7 \cdot 1.06^{-D} \tag{3.1}$$

where D is the measured nanoparticle diameter and $[V^O]$ is the oxygen vacancy concentration. However, this fit has a χ^2 of 4.7, so the confidence in this specific relation is poor.

XPS is known to be useful only as a relative measure of oxygen vacancy concentration due to the high vacuum necessary to make measurements; however, the measurements confirm that the expected trend of increasing oxygen vacancy concentration continues as particle sizes become extremely small.

The work of Kugai demonstrated that smaller nanocrystals result in a substantial improvement to the catalytic efficiency in the Ni-Rh/CeO$_2$ system, so even without bio-templating, utilizing this new synthesis for CeO$_2$ nanocrystals should result in a substantial improvement to the existing technology due to the decrease from about 13% to 18% oxygen vacancies going from his 6.1 nm particles to my 1.3 nm particles. [2]

3.4   CeO$_2$ Nanoparticle Thermal Stability.

The thermal stability of 2 nm, 3 nm, and 6 nm nanocrystals were tested by taking periodic XRD spectra of a powder sample heated to 450°C, 500°C, and 550°C for 2 hours using a PANalytical X'Pert PRO diffractometer with an in-situ furnace. The nanocrystal size was calculated using the full width at half maximum of the isolated ceria {200} peak at 48 degrees. Although using only a single peak reduces the absolute accuracy of an XRD-based size measurement due to the presence of strain in the crystallites, it also allows for time resolution of about 1 min per measurement. This quick measurement time allows for better comparison to time-dependent growth models, especially at early times when particles are growing rapidly. Longer period scans were done before and after the heat treatment to characterize the impact of strain on the particle sizes. Even in the case of 2.0 nm particles where strain went from ~2% to ~0.1%, the change in absolute offset was less than 0.5 nm.

The sintering behavior of loose powders is not very well understood, so we have applied a simple power-law style growth equation to the system in order to quantify the behavior. We have used the equation

$$D(t)^m - D(0)^m = k \cdot t \tag{3.2}$$

where $D(t)$ is the average particle diameter as a function of time, m is the "growth exponent", k is the rate constant, and t is the time. This equation is based on a model of diffusion limited coarsening. [58, 59]

D_0 (nm)	m	Q (eV)	C
6.0	9	1.9	$5 \cdot 10^{26}$
3.1	8	2.8	$4 \cdot 10^{29}$
2.0	8	3.5	$1 \cdot 10^{34}$

Table 3.3: The fitted growth parameters for nanocrystalline CeO_2.

The rate constant in diffusion-limited systems is frequently modeled as a diffusion rate governed by an Arrhenius type activation energy and prefactor. This can be written as

$$k = C \cdot \exp\left(\frac{-Q}{k_B T}\right) \tag{3.3}$$

where k is the rate constant in Equation 3.2, C is a prefactor on the rate characteristic of the sample, Q is an activation energy characteristic of the sample, and T is the temperature. Using this model, it is possible to take time-resolved measurements of the average particle size of a sample at different temperatures and fit the temperatures simultaneously to this model to calculate the rate constant prefactor, activation energy, and growth rate order of the system. With three variables and three sets of temperature data, the system should have a single solution that satisfies an optimal fit to all three temperature data sets.

Each spectrum was analyzed to determine the particle size, and the composite data is shown in Fig. 3-7. Of particular interest is the very high growth exponent, far higher than the third order behavior predicted for typical grain growth or diffusion limited growth. Additionally, the particles with the smallest initial size showed a larger difference in growth rate as a function of temperature, as well as a larger overall growth rate at high temperature, than the particles with the largest initial size. The fitted parameters m, Q, and C for these particles are summarized in Table 3.3.

3.4.1 Thermal stability mechanism

As described previously, the size-dependance of the energetics, which does not change as the particles grow, indicates a permanent structural defect introducted in the initial synthesis stages which is stable at the temperatures investigated. Of the likely defects, oxygen surface defects were chosen as the mechanism most consistent with the growth behavior. Hydroxide surface defects, Ce-O-Cl or other cerium compounds on the surface, and morphological changes which resists sintering were considered, but ultimately rejected.

To isolate which of these possible mechanisms are controlling sintering, a single large batch of ~ 3 nm particles were produced and subsequently postprocessed in a variety of ways. Although particles were shown to exhibit the $\sim 8^{th}$ order growth behavior when dried in air and then heat treated, if the samples were dried at 120°C, they exhibited classical 3rd order growth. Particles dried at room temperature and subsequently resuspended in water and dried at 120°C retained

68
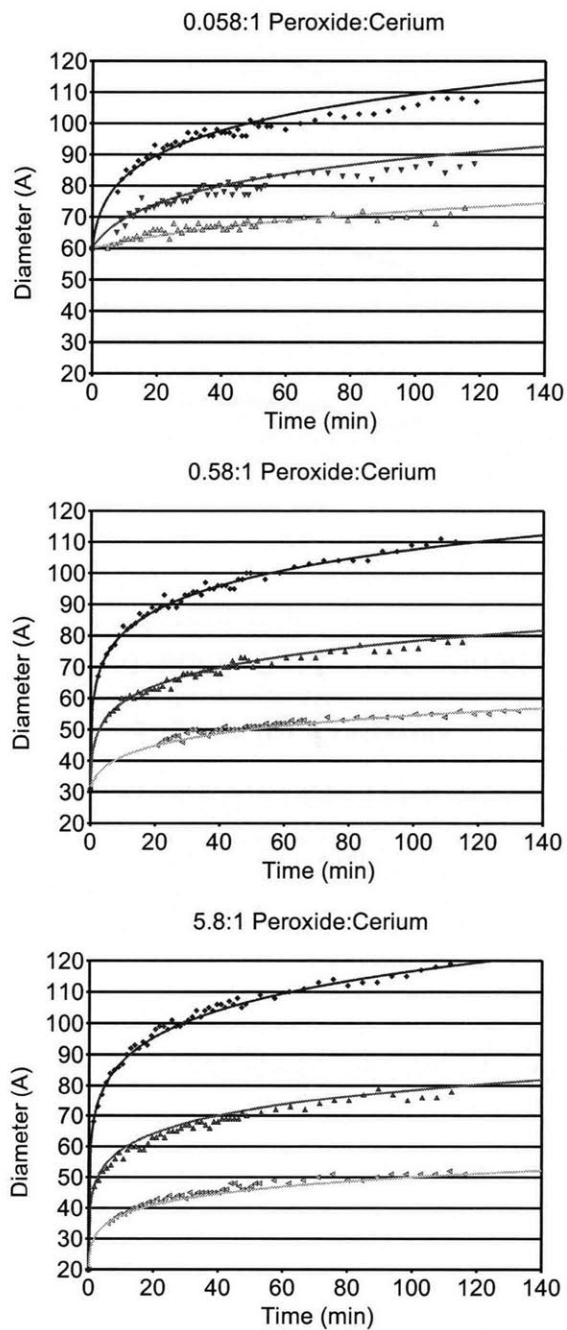
Figure 3-7: Sintering Behavior of CeO$_2$ Nanocrystals. (a) 6.0 nm initial size. (b) 3.1 nm initial size. (c) 2.0 nm initial size. Fit lines are plotted based on modeling all three sets of temperature data simultaneously to a power-law model, optimized to minimize total error from the real data by varying activation energy, growth exponent, and prefactor.
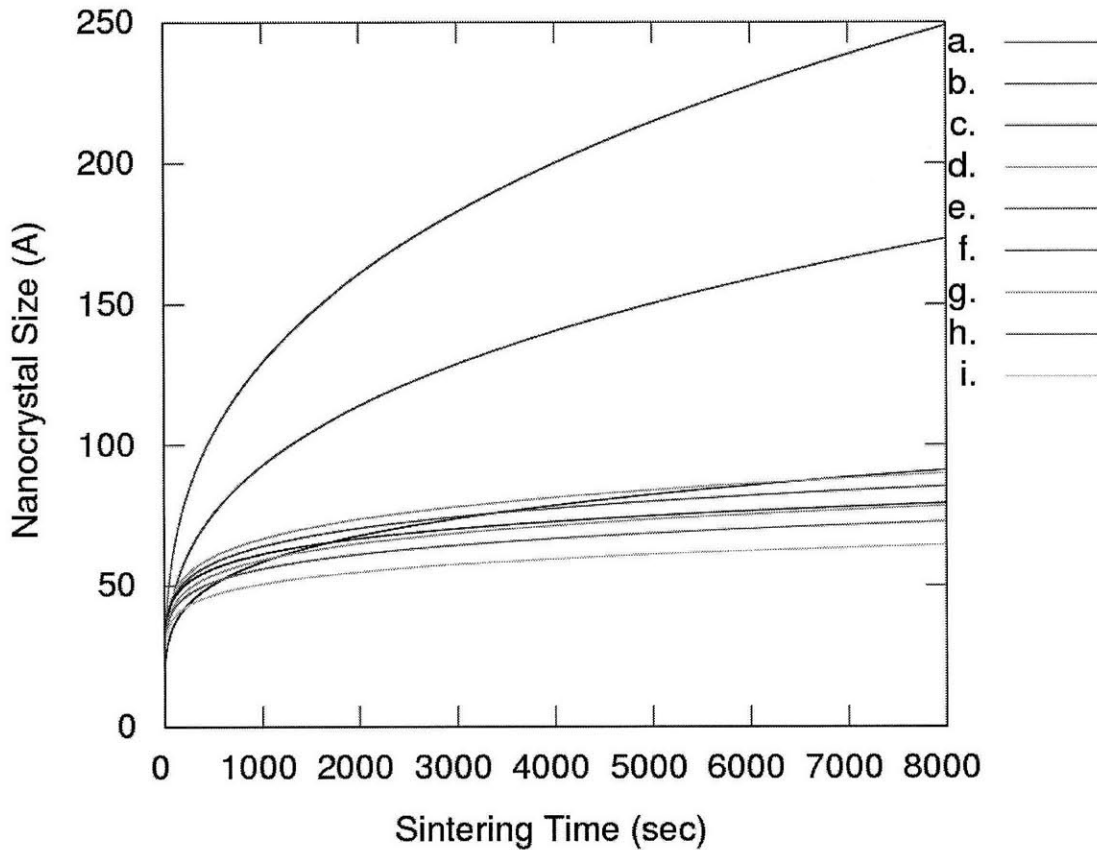
Figure 3-8: CeO_2 sintering tests done with different preperation methods. (a) Dried at 120C ($m = 3.2$) (b) Dried at 120C ($m = 3.3$) (c) Air Dried, Rewetted with H_2O, Heat Treated at 120C ($m = 4.7$) (d) Air Dried, Rewetted with Hexane, Heat Treated at 120C ($m = 7.0$) (e) Dried at 80C ($m = 7.2$) (f) Air Dried, Heat Treated at 120C ($m = 8.0$) (g) Air Dried, Heat Treated at 120C ($m = 7.4$) (h) Air Dried, Rewetted with H_2O, Heat Treated at 120C ($m = 8.0$) (i) Dried at 120C, Rewetted with H_2O, Air Dried ($m = 8.6$)

their $\sim 8^{th}$ order growth behavior. Particles dried at 120°C and subsequently resuspended in water and dried at room temperature demonstrated 8th order growth behavior. This result demonstrates that the critical step is drying at room temperature over a long time period, and that the aspect of the system which is inhibiting growth is stable once introduced. All results are shown in Fig 3-8.

Ce-O-Cl defects initially seem to be a likely mechanism as the defects would be stable at high temperature. To investigate this, a comparison synthesis was done using cerium nitrate as a precursor. The resulting sintering profile is shown in Fig. 3-9 alongside a typical chloride synthesis using the same methodology. As can be seen, the two curves are essentially overlapping within the errors of the measurement, demonstrating that chloride ions are not required to produce the observed behavior. XPS was performed to look at the surface ratio of chlorine to ceria, with a result of approximately 1 atomic% chlorine compared to cerium atoms. XPS also shows a small sodium peak (4 atomic%), so the chlorine is likely bound to the sodium, with a small amount of sodium

hydroxide remainder. Further, it is unlikely that nitride and chloride defects would exhibit identical energetics, making either defect unlikely due to the identical behavior. XPS of the nitride produced sample showed only a very tiny nitrogen peak in the final spectra.

Drying at room temperature is unlikely to cause morphological changes that would not occur at or be reversed by raised temperature due to the low mobility of atoms, so we do not believe that micro- or nano-structural effects could be the cause of the unexpectedly high thermal stability. Similarly, hydroxide defects are extremely unlikely to survive heat treatment; calcination under air is a standard way to convert hydroxide materials to oxides, so hydroxide defects surviving high temperature heat treatment is very unlikely.

The remaining candidate defect possibility is that of oxygen defects in the crystal. In the previous section we showed that the activation barrier to sintering is substantially higher for 2.0 nm particles ($Q = 3.5$ eV) than for 6.0 nm particles ($Q = 1.9$ eV). This energy barrier increase is consistent with an oxygen vacancy effect, as smaller particles also have a substantially higher oxygen vacancy concentration (18% for 2.0 nm versus 14% for 6.0 nm particles) and so more defects are present in the samples with higher energetic barriers to sintering.

Overall, we propose a mechanism of surface passivation by oxygen vacancies as the most likely cause of this high thermal stability. Particles are initially generated with a very large number of oxygen vacancies (~10-20% as demonstrated previously by XPS). After synthesis, due to the decreased oxygen capacity of ceria at elevated temperatures, and the increased oxidation speed of steam versus liquid water, drying the particles at over the boiling point of water provides a route to oxidize the particles beyond what would be their equilibrium point at room temperature, removing oxygen vacancies. If the particles are then re-exposed to water and allowed to dry at room temperature, the oxygen vacancies again go to the room temperature equilibrium levels over the long period of drying time.

There are several mechanisms by which oxygen vacancies could result in heightened thermal stability. First, when the particles begin to combine with their neighbors, a large number of oxygen vacancies would be trapped in the neck, producing pinning points that could act as an energetic barrier to sintering. Second, oxygen defects on the surface of the particles could act as pinning points and lead to a barrier to surface diffusion, likely the dominant transport mechanism at such low temperatures, and reduce the speed at which particles can merge. Finally, larger particles grown from smaller particles have a lower oxygen vacancy concentration, so the process of sintering the particles also requires the chemical removal of oxygen vacancies, which could represent an energetic barrier to growth based on the distance from the equilibrium oxygen vacancy concentration. It is unclear which of these specific mechanisms is the rate-limiting effect in this system.

It is unclear, based on this model, if sintering in the presence of steam would result in much faster growth of particles. If oxygen vancacies are removed during use, this model would predict
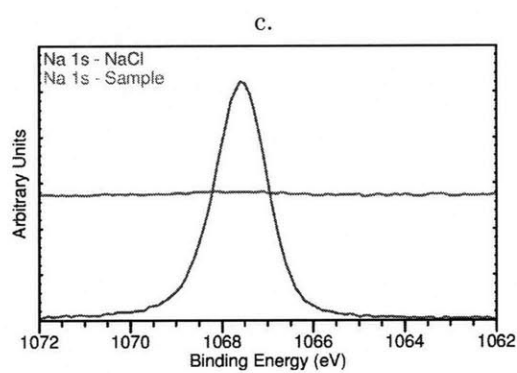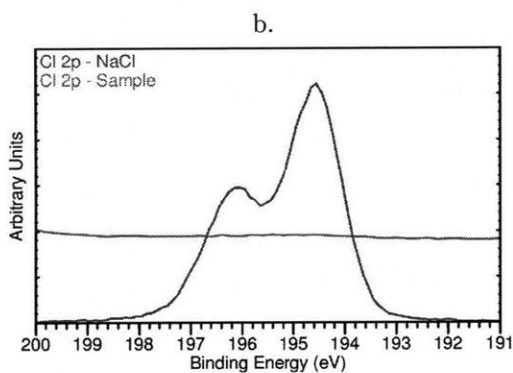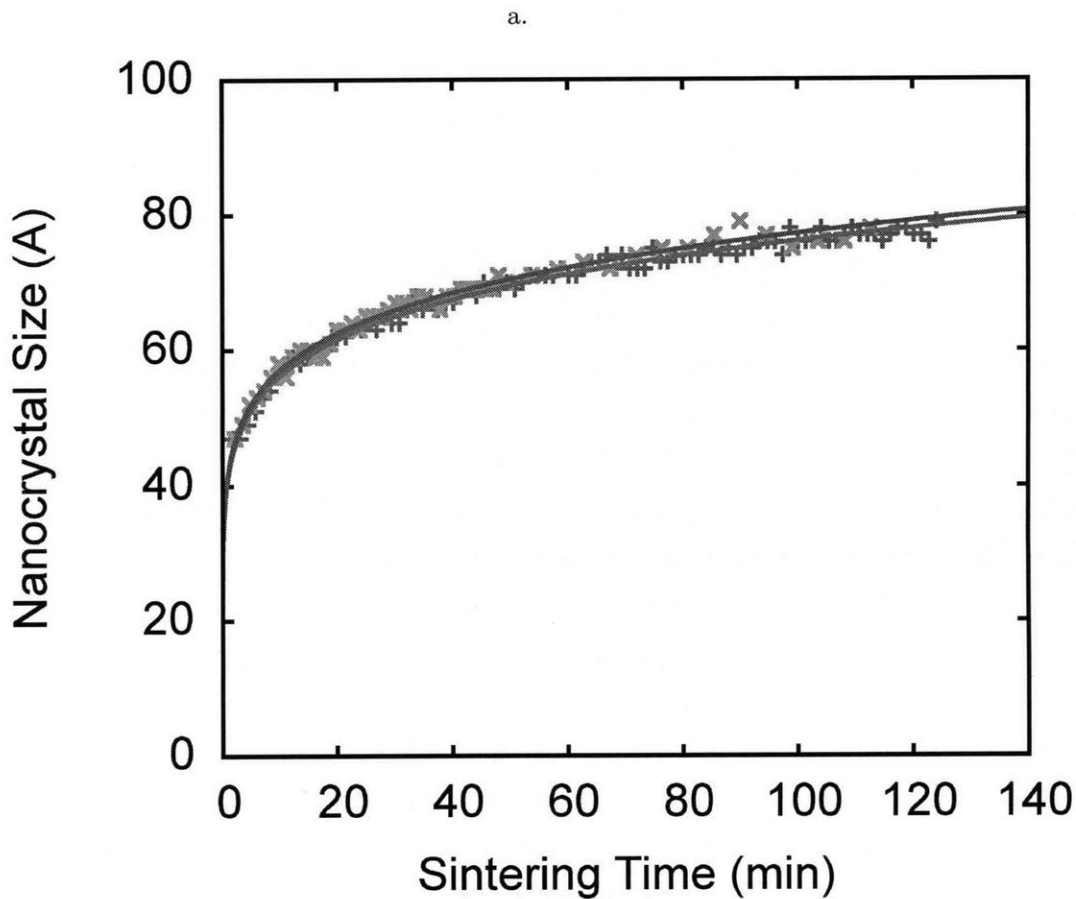
Figure 3-9: (a) CeO$_2$ sintering tests done using a nitrate precursor, compared to using a chloride precursor. Both samples were dried at room temperature and done at the same concentrations, and began with identical particle sizes. Both samples exhibit nearly identical 8th order growth rates. (b) XPS of the Cl 2p region showing NaCl compared to CeO$_2$ synthesized from chloride salts. The chlorine peak represents approximately 1:99 chlorine:cerium. (c) XPS of the Na 1s peak showing NaCl compared to CeO$_2$ synthesized from chloride salts. The sodium peak represents approximately 4:96 sodium:cerium.
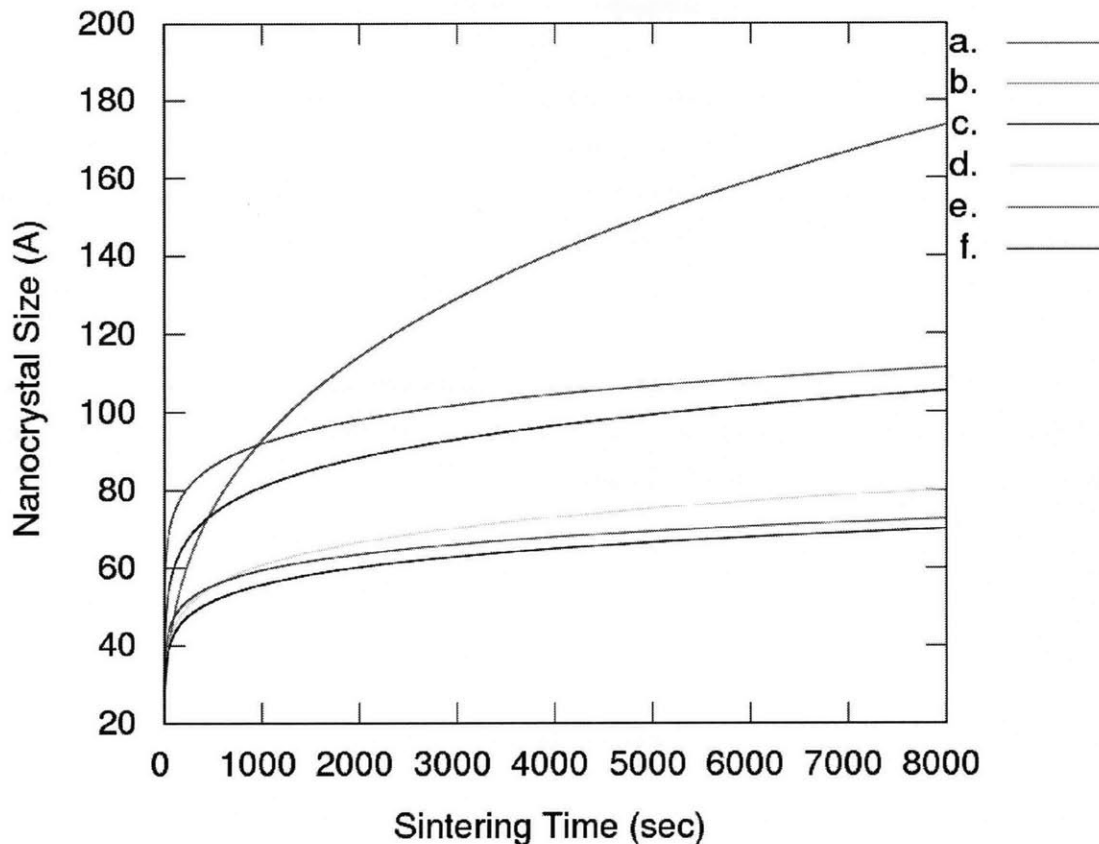
Figure 3-10: CeO_2 sintering tests done with lanthanum doping. (a) 0% La dried at 120C ($m = 3.3$) (b) 10% La dried at 120C ($m = 11.0$) (c) 5% La dried at 120C ($m = 7.9$) (d) 0% La air dried ($m = 7.5$) (e) 10% La air dried ($m = 10.3$) (f) 5% La air dried ($m = 9.0$)

that the particles would regain their typical growth exponent of 3. However, actual experimental results of taking air dried particles, rewetting with water or hexane, and drying at 120°C retained their thermal stability, suggesting that once dried at room temperature in water, the defects are stable in the presence of steam.

3.4.2 Lanthanum for surface passivation

Lanthanum was used to coat the nanoparticles and produce an alternative passivation mechanism by mixing lanthanum chloride with cerium chloride during synthesis at 5% and 10% molar ratios. Particles were dried both at room temperature in air as well as at 120°C. The overall growth is shown in Fig. 3-10.

In these tests, the only sample which exhibited low thermal stability was the one dried at 120°C with no La dopant. Even 5% La dopant increases the growth exponent to $m = 7.9$ when dried at 120°C, and 10% La increases the growth exponent all the way to $m = 11.0$. Overall, although the exact numbers for the growth exponent may not be accurate due to differences in the quality of

73

coating, this demonstrates the very high growth exponent caused by surface passivation.

This data also provides further evidence that the effect is not caused by surface chloride or nitride compounds, as the intentionally introduced lanthanum surface defects demonstrate very different energetics from the as prepared CeO_2 particles using chloride or nitride based precursors. The difference in energetics supports the statement made earlier that nitride and chloride impurities should exhibit different growth behavior, even if both would independently inhibit particle growth. This also provides an alternative option for producing extremely high thermal stability nanoparticles of ceria.

It is also notable that lanthanum-doped ceria particles show further suppressed growth when dried at low temperatures, suggesting a composite effect where both oxygen defects and lanthanum defects are contributing to the thermal stability.

Chapter 4

Peroxide Mediated Hydroxylation for Metal Oxide Nanoparticle Synthesis

A wide variety of metal oxide nanoparticles were synthesized using a peroxide mediated hydroxylation in which the metal chloride is converted either directly into the corresponding oxide, or into the corresponding hydroxide. Hydrogen peroxide was used to introduce defects onto the surface of newly nucleated particles to inhibit growth while not affecting particle nucleation rates. The result was nanocrystals ranging in size from less than 1 nm to several tens of nanometers. The particles were heat treated at 400°C to investigate particle growth and the properties after calcination.

4.1 Introduction

Metal oxides represent a very large class of materials useful in a variety of applications including electronics, optics, ceramics, and catalysts. [60] Many applications that are dependent upon surface area of the material or size of the crystallite domain can be further enhanced through the use of the nanoparticle form of metal oxides. [61] As such, metal oxide nanoparticles have garnered much research interest over the past few decades, both in novel applications and new synthesis methods.

Current metal oxide nanoparticle synthesis methods represent an eclectic ensemble of chemical processes; many, however, produce fairly large crystallite domains, require toxic chemicals, or take place only under extreme conditions. The most common methods use either aqueous or organic solvents, with or without the use of a surfactant, and generally take place under mild conditions. [61–63] Organometallic methods and microemulsion methods have also been used to synthesize metal oxide nanoparticles under mild conditions. [64–66]

Methods that require more extreme conditions include spray pyrolis, hydrogen-plasma metal reactions and hydrothermal reactions at supercritical conditions. [67–70] None of the above methods, however, have been reported to synthesize a broad class of metal oxide nanoparticles of very small nanocrystallite size, and instead appear to be used only in the synthesis of a small number of metal oxides. The ability to produce a wide range of materials with extremely small nanocrystalline domains allows for a wide array of new potential materials. In particular, a key to the manufacturability of mixed phase nanocrystalline materials, and a useful starting point for making complex single-phase ceramics, is that the materials can be made using compatible synthesis techniques.

With the great success in forming extremely small nanocrystals of ceria, further tests were warranted for seeing if other metal oxide nanoparticles could be synthesized using the same synthesis methods.

4.2   Procedure

Using a method derived from that developed by Yamashita et al [52], nanocrystals of various metal oxides were formed using precipitation in aqueous solution of a corresponding metal chloride or metal chloride hydrate by adding NaOH and H_2O_2. Instead of using a small amount of hydrogen peroxide to oxidize the materials, we increased the amount of hydrogen peroxide by 100-fold over the literature in order to produce smaller nanocrystallites, and induce more complete initial oxidation.

Nanoparticles were produced according to the following procedure.

1. 100 mL of 100 mM metal chloride solution is stirred rapidly in a 250mL Erlenmeyer flask for 30 minutes.

2. 200 uL of 30 wt% H_2O_2 is added to 10 mL of 3 M NaOH solution in a separate flask.

3. The mixed NaOH/H_2O_2 solution is added rapidly to the metal chloride solution.

4. Solution is allowed to react for 30 minutes.

5. Supernatant is removed by centrifugation, precipitate is washed with millipore water to remove any remaining NaCl, and centrifuged again. This is repeated for a total of three washings.

6. Supernatant is discarded and precipitate is dried in air at room temperature.

The dried precipitate is split into two samples of roughly equal size. One is heat treated at 400°C for 2hr. Both samples are analyzed with XRD.

4.3   Results

The 22 different materials formed with this synthesis were categorized into a number of groups. Of the materials attempted, 15 of them appeared to readily form either the oxide or a mostly amorphous material which appeared to be oxide and which transformed into identifiable oxide after

Precursor	Init Prod	Init Size	400C Prod	400C Size
$CeCl_3$	CeO_2	2.0	CeO_2	4.5
$RuCl_3$	RuO_2	2.9	RuO_2	34.6
$InCl_3$	In_2O_3	<1	In_2O_3	1.2
$SnCl_3$	SnO_2	<1	SnO_2	1.2
$CoCl_3$	Co_3O_4	4.5	Co_3O_4	6.9
$TbCl_3$	Tb_2O_3	1.0	Tb_4O_7	1.4
$MnCl_2$	Mn_3O_4	13.2	Mn_3O_4	15.5
$SmCl_3$	Sm_2O_3	3.8	Sm_2O_3	5.0
$LuCl_3$	Lu_2O_3	1.0	Lu_2O_3	1.1
$GdCl_3$	Gd_2O_3	1.1	Gd_2O_3	1.3
$YbCl_3$	Yb_2O_3	1.0	Yb_2O_3	1.3
YCl_3	Y_2O_3	1.0	Y_2O_3	1.0
$DyCl_3$	Dy_2O_3	1.1	Dy_2O_3	1.3
$ErCl_3$	Er_2O_3	1.0	Er_2O_3	1.3
$RhCl_3$	Rh_2O_3	<1	Rh_2O_3	4.0

Table 4.1: Fifteen of the materials attempted with this synthesis method were made easily and appeared to immediately form the oxide with no heat treatment. In each case, the sample was heat treated, and the nanocrystallite size as measured by XRD peak broadening was recorded. In the case of terbium oxide, the oxide phase appears to have changed during heat treatment. Sizes are shown in nanometers.

a heat treatment at 400°C for 2 hours. Four more materials formed a non-oxide phase initially, but were transformed into the oxide after heat treatment at 400°C for 2 hours.

Each of the samples was analyzed using XRD as initially prepared and after heat treatment in order to get an estimate of crystallite size. In the case of the partially amorphous samples, the size was determined from the peak broadening of the lower angle peak only, to remove errors which would be introduced by incorrectly fitting the amorphous part of the spectra to nanocrystalline peaks. The materials which were readily synthesized in this way are listed in Table 4.1.

In each case, the initially formed oxide, initial nanocrystallite size, final oxide formed, and final nanocrystalline size are reported. The only material which appeared to change oxide phase during heat treatment was terbium oxide, which began as the white Tb_2O_3 due to the initial Tb^{3+} ions in solution, and became the brown Tb_4O_7 phase upon heat treatment. However, with these two phases, the crystal structures are nearly indistinguishable due to the small particle size, so the phase change is inferred from the color change only.

In most cases, the initially formed nanoparticles are exceptionally small, with an estimated particle size of approximately 1 nm or less for 9 of the samples. The only sample which began with a crystallite size greater than 4.5 nm was Mn_3O_4, showing the general advantage gained by using peroxide to inhibit particle growth and encourage the formation of only very small nanocrystals. In many cases, there was very little crystallite growth during the heat treatment phase, although in the case of RuO_2 there was a very significant size increase. Representative TEM of Co_3O_4, Lu_2O_3, and Tb_4O_7 showing the general microstructure of materials synthesized using this method (Fig 4-1).

In the case of four of the attempted materials, the initially formed phase was not the oxide,
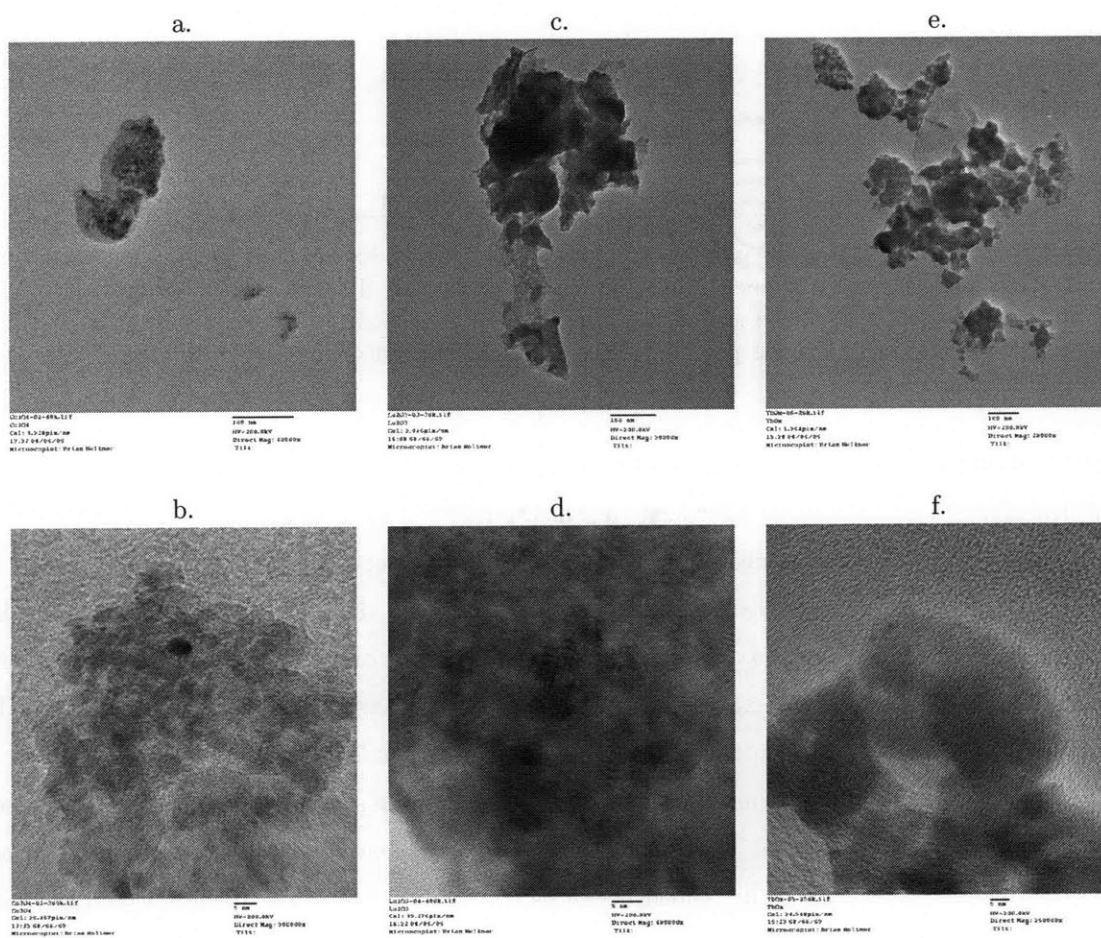
Figure 4-1: Representative TEM images of metal oxides synthesized using peroxide mediated hydroxylation. a) Co_3O_4 at low magnification. b) Co_3O_4 at high magnification showing lattice fringes. c) Lu_2O_3 at low magnification. d) Lu_2O_3 at high magnification showing lattice fringes, e) Tb_4O_7 at low magnification. f) Tb_4O_7 at high magnification showing lattice fringes.

Precursor	Init Prod	400C Prod	400C Size
$NiCl_2$	$Ni(OH)_2$	NiO	9.6
$FeCl_3$	$Fe_2O_3+FeO(OH)$	Fe_2O_3	1.4
$CuCl_2$	$Cu(OH)_2$	CuO	22.7
$ZnCl_2$	Mixed	ZnO	16.3

Table 4.2: The materials which initially formed a non-oxide phase in a large amount, but which fully transformed to the oxide phase upon heat treatment at 400°C for 2 hours. The initially formed phase, final phase, and final phase nanocrystallite size estimate are shown. Sizes are shown in nanometers.

Precursor	Init Prod	800C Prod
$LaCl_3$	$La(OH)_3$	$La_2O_3+LaOCl$
$NdCl_3$	$Nd(OH)_3+NdOCl+amorph$	$Nd_2O_3+NdOCl$
$PrCl_3$	$Pr(OH)_3$	PrO_2

Table 4.3: The materials which did not convert to an oxide readily after a 400°C heat treatment for 2 hours are shown. In each case, after further heat treatment at 800°C, the material formed the oxide as a majority phase, and in some cases also contained a chloride impurity. Sizes are shown in nanometers.

but after heat treatment at 400°C, the material transformed fully into the oxide (Table 4.2). In three of these cases, the initial material was the related hydroxide, but in the case of zinc oxide, the initially formed material had a large number of unidentifiable phases present. However, all of the unidentifiable phases disappeared upon heat treatment.

Three of the materials we attempted to synthesize did not form an oxide even upon heat treatment at 400°C (Table 4.3). In the case of lanthanum oxide, it formed instead lanthanum hydroxide $La(OH)_3$ of fairly large particle size. The lanthanum hydroxide particles appear to shrink upon heat treatment, suggesting that they are being gradually converted into another material, and indeed the amorphous background appears to increase in the heat treated sample. However, after heat treating the sample at 800°C, the majority of the sample is in the La_2O_3 or the $LaOCl$ phase with a small impurity of $La(OH)_3$, suggesting that this material simply requires a higher temperature for full conversion. The chloride is likely a residual of using a chloride precursor, and switching to a nitrate precursor should remove this byproduct.

In the case of neodymium oxide, the initial synthesis produced a combination of large $Nd(OH)_3$ and $NdOCl$ particles with a background of about 1 nm particles of an unidentifiable phase. The unidentifiable phase represented approximately 60% of the spectrum. After heat treatment at 400°C, the amorphous background grew to the dominant phase, and is clearly not $Nd(OH)_3$ or $NdOCl$. Upon heat treatment at 800°C, it becomes clear that the other phases were being converted into Nd_2O_3, and almost all of the peaks present are Nd_2O_3. However, there is a small impurity of $NdOCl$, likely possible because of the presence of chloride precursor. If it was desired to remove the chloride, it should be possible to do the same synthesis with nitrate precursors.

The praseodymium oxide synthesis initially formed a material readily identifiable as praseodymium

hydroxide $Pr(OH)_3$. Upon heat treatment, the color changed from a pale green to brown, and the XRD became a more complicated mixed phase of $Pr(OH)_3$ and PrO_2. However, the amount of PrO_2 was small compared to the $Pr(OH)_3$ amount. Further heat treatment should readily produce the oxide phase.

In terms of trends, the three most difficult materials are all located near each other on the periodic table and would have formed a 3^+ oxide. Cerium, the element between them, formed the 4^+ oxide immediately upon synthesis, suggesting that if the lanthanum, praseodymium, and neodymium had a stable 4^+ oxide, they may have been able to form readily.

The four materials which formed the oxide after a mild heat treatment were also all very close to each other on the periodic table, and several began as the 2^+ salt. The remaining materials all formed an extremely small oxide readily and rapidly at room temperature with no heat treatment.

4.3.1   Cerium Oxide

Cerium oxide CeO_2 phase was formed immediately as prepared, and remained in the CeO_2 phase through heat treatment at 400°C. The nanocrystals started at 2.0 nm and grew to 4.5 nm over the course of heat treatment. The product began as an orange powder, and became pale yellow after heat treatment.

4.3.2   Ruthenium Oxide

Ruthenium oxide RuO_2 phase was formed immediately as a nanocrystalline material as prepared, and remained in the RuO_2 phase through heat treatment at 400°C. The nanocrystals started at 2.9 nm and grew to 34.6 nm over the course of heat treatment (Fig 4-2). The product began as a black powder and remained a black powder after heat treatment.

4.3.3   Indium Oxide

Indium oxide In_2O_3 phase was formed immediately as prepared, and remained in the In_2O_3 phase through heat treatment at 400°C, although it was highly nanocrystalline throughout. The nanocrystals started at less than 1 nm, and grew to 1.2 nm over the course of heat treatment (Fig 4-3). Due to the highly nanocrystalline sample, they were further heat treated at 800°C in order to perform phase identification, which produced a clear In_2O_3 phase. The product was a white powder before and after heat treatment.

4.3.4   Tin Oxide

Tin Oxide in the Casserite SnO_2 phase is formed immediately as prepared, and remained in the SnO_2 phase through heat treatment (Fig 4-4). The nanocrystals started at less than 1 nm and grew

Figure 4-2: XRD Ruthenium Oxide before and after heat treatment. a) As prepared. b) After heat treatment at 400°C for 2 hr. The lines corresponding to RuO_2 are shown for comparison.

Figure 4-3: XRD of Indium Oxide before and after heat treatment. a) As prepared. b) After heat treatment at 400°C for 2 hr. The lines corresponding to In_2O_3 are shown for comparison. Subsequent heat treatment at 800°C was done to confirm the phase identification for the nanocrystalline material.
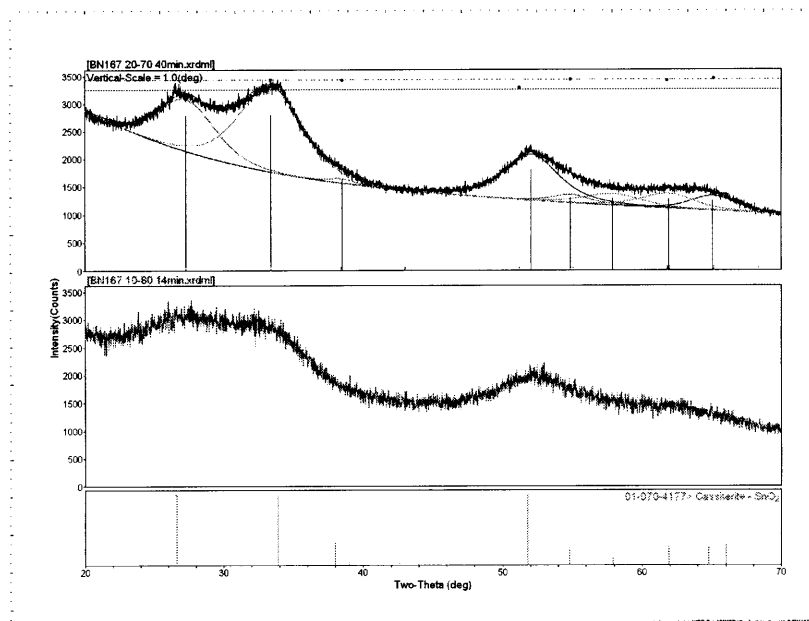
Figure 4-4: XRD from 20-70 degrees of SnO_2 is shown before and after heat treatment. The lines corresponding to SnO_2 phase are shown for comparison.

to 1.2 nm after heat treatment. The product was a white powder before and after heat treatment.

4.3.5   Cobalt Oxide

Cobalt Oxide in the Co_3O_4 phase was formed immediately as prepared, and remained in the Co_3O_4 phase through heat treatment. The nanocrystals started at 4.5 nm, and grew to 6.9 nm over the course of heat treatment (Fig 4-5). The product was a black powder before and after heat treatment.

4.3.6   Terbium Oxide

Terbium Oxide (Tb_2O_3 or TbO_2) was formed immediately as prepared, but we believe it transformed to the Tb_4O_7 phase upon heat treatment at 400°C. The product started as a white powder, typical of a Tb_2O_3 phase, and became brown after heat treatment, typical of a Tb_4O_7 phase.

The Tb_2O_3 and TbO_2 phases are nearly indistinguishable by XRD, and the nanocrystals made were exceptionally small, with the peaks largely overlapping. As Tb_4O_7 is a mixed phase of TbO_2 and Tb_2O_3, it is also indistinguishable from the other oxides by XRD alone. However, the peaks are distinct enough to rule out an amorphous material — they are instead extremely nanocrystalline.

The nanocrystals size estimated by looking at only the first peak, started at 1.0 nm, and grew to 1.4 nm over the course of heat treatment (Fig 4-6).

Figure 4-5: XRD from 10-85 degrees of Cobalt Oxide before and after heat treatment. a) As prepared. b) After heat treatment at 400°C for 2 hr. The lines corresponding to Co_3O_4 are shown for comparison.

Figure 4-6: XRD from 10-85 degrees of Terbium Oxide before and after heat treatment. a) As prepared. b) After heat treatment at 400°C for 2 hr. The lines corresponding to TbO_2 are shown for comparison.

4.3.7 Manganese Oxide

Manganese oxide Mn_3O_4 phase was formed immediately as prepared, and remained in the Mn_3O_4 phase through heat treatment at 400°C. The nanocrystals started at 13.2 nm, and grew to 15.5 nm over the course of heat treatment (Fig 4-7). The product began as a very dark brown powder, and remained a dark brown powder after heat treatment.

4.3.8 Samarium Oxide

Samarium oxide Sm_2O_3 was formed immediately as prepared, and remained in the Sm_2O_3 phase through heat treatment at 400°C. The nanocrystals started at 3.8 nm and grew to 5.0 nm over the course of heat treatment (Fig 4-8). The product began as a white powder, and remained a white powder after heat treatment.

4.3.9 Lutetium Oxide

Lutetium oxide Lu_2O_3 was formed immediately as prepared, and remained in the Lu_2O_3 phase through heat treatment at 400°C. The nanocrystals started at 1.0 nm and grew to 1.1 nm over the course of heat treatment (Fig 4-9). The product began as a white powder, and remained a white powder throughout heat treatment.

4.3.10 Gadolinium Oxide

Gadolinium Oxide Gd_2O_3 phase was formed immediately as prepared, and remained in the Gd_2O_3 phase through heat treatment at 400°C. The nanocrystals started at 1.1 nm, and grew to 1.3 nm over the course of heat treatment (Fig 4-10). The product began as a white powder, and remained a white powder after heat treatment.

4.3.11 Ytterbium Oxide

Ytterbium oxide Yb_2O_3 phase was formed immediately as prepared, and remained in the Yb_2O_3 phase throughout heat treatment at 400°C. The nanocrystals started at 1.0 nm and grew to 1.3 nm over the course of heat treatment (Fig 4-11). The product began as a white powder, and remained a white powder after heat treatment.

4.3.12 Yttrium Oxide

Yttrium oxide Y_2O_3 phase was formed immediately as prepared, and remained in the Y_2O_3 phase through heat treatment at 400°C. The nanocrystals started at 1.0 nm and did not grow appreciably

Figure 4-7: XRD from 10-85 degrees of Manganese Oxide before and after heat treatment. a) As prepared. b) After heat treatment at 400°C for 2 hr. The lines corresponding to Mn_3O_4 are shown for comparison.

Figure 4-8: XRD from 10-85 degrees of Samarium Oxide before and after heat treatment. a) As prepared. b) After heat treatment at 400°C for 2 hr. The lines corresponding to Sm_2O_3 are shown for comparison.
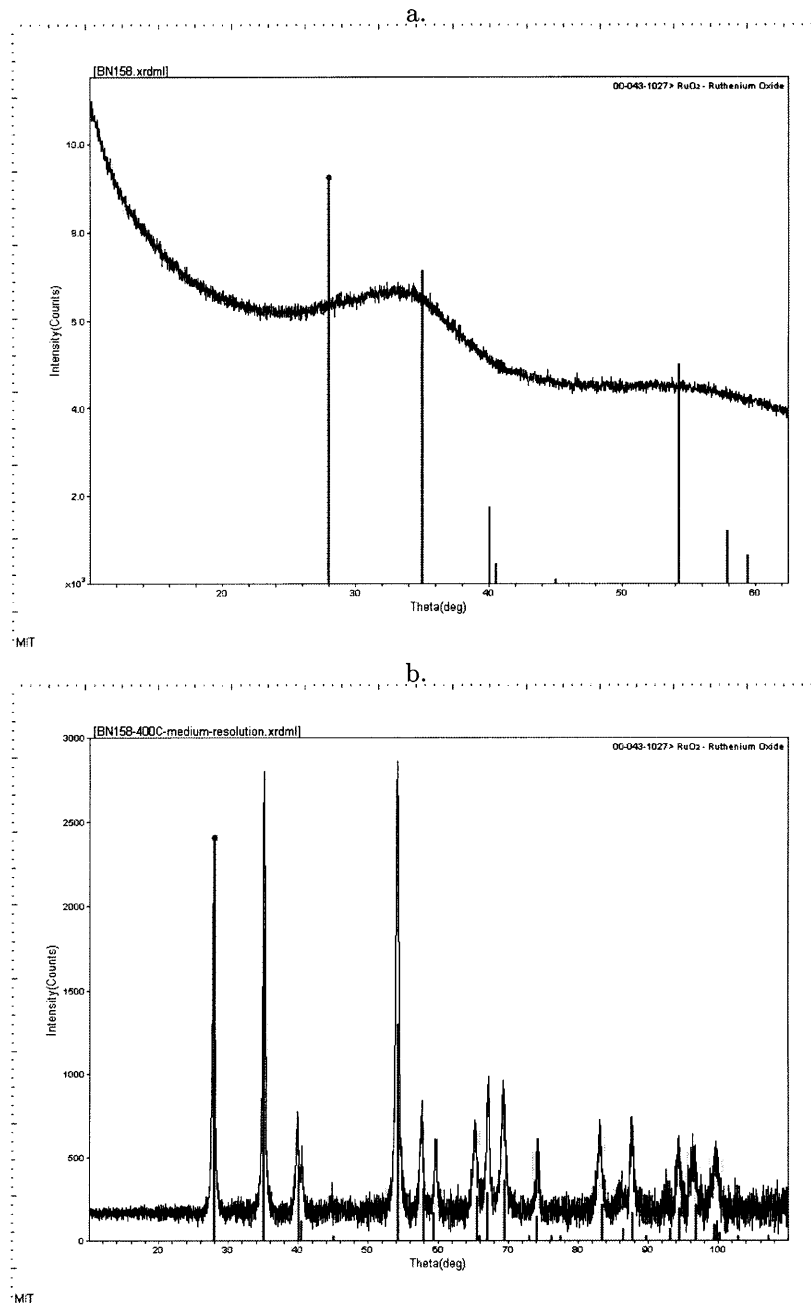
Figure 4-9: XRD from 10-85 degrees of Lutetium Oxide before and after heat treatment. a) As prepared. b) After heat treatment at $400°C$ for 2 hr. The lines corresponding to Lu_2O_3 are shown for comparison.

89

Figure 4-10: XRD from 10-85 degrees of Gadolinium Oxide before and after heat treatment. a) As prepared. b) After heat treatment at 400°C for 2 hr. The lines corresponding to Gd_2O_3 are shown for comparison.
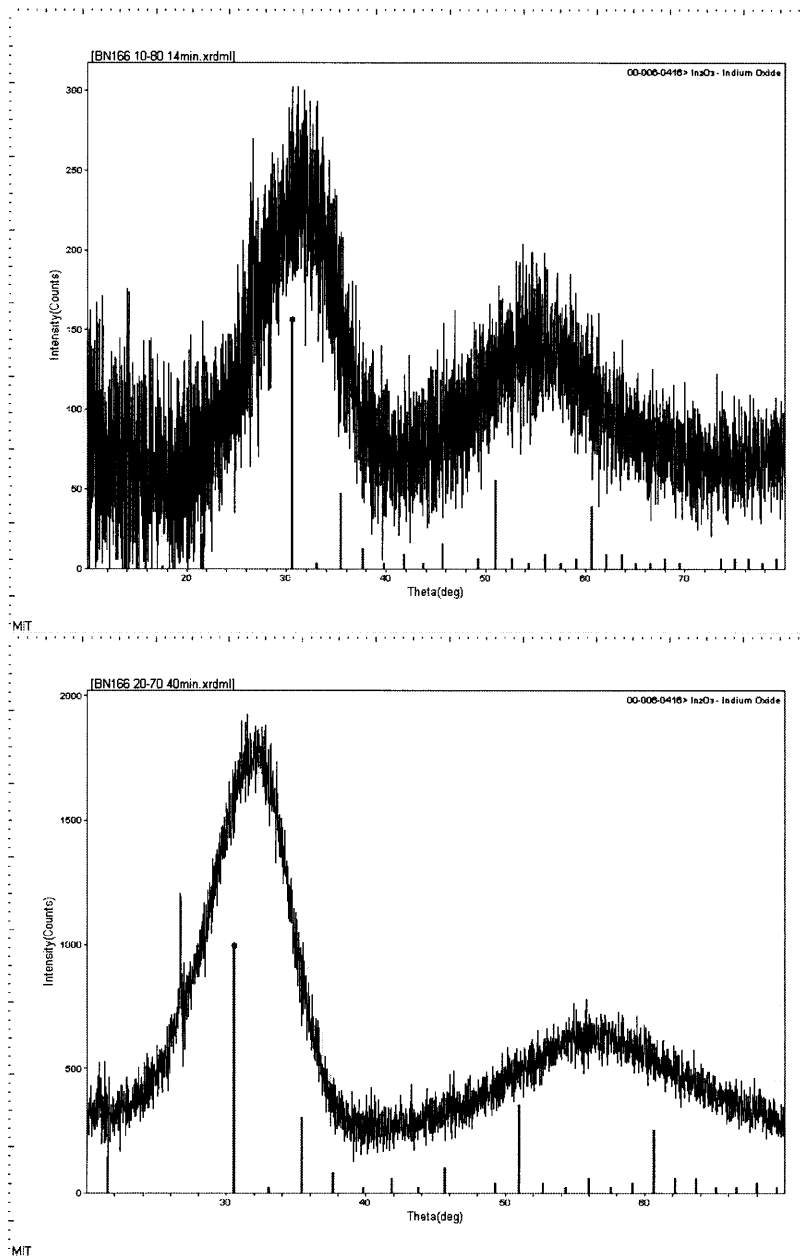
90

Figure 4-11: XRD from 10-85 degrees of Ytterbium Oxide before and after heat treatment. a) As prepared. b) After heat treatment at 400°C for 2 hr. The lines corresponding to Yb_2O_3 are shown for comparison.

during heat treatment (Fig. 4-12). The product began as a white powder and gained a pale yellow tint after heat treatment.

4.3.13 Dysprosium Oxide

Dysprosium oxide Dy_2O_3 phase was formed immediately as prepared, and remained in the Dy_2O_3 phase through heat treatment at 400°C. The nanocrystals started at 1.1 nm and grew to 1.3 nm over the course of heat treatment (Fig 4-13). The product began as a white powder and remained a white powder after heat treatment.

4.3.14 Erbium Oxide

Erbium oxide Er_2O_3 phase was formed immediately as prepared, and remained in the Er_2O_3 phase through heat treatment at 400°C. The nanocrystals started at 1.0 nm, and grew to 1.3 nm over the course of heat treatment (Fig 4-14). The particles began as a pink powder, and remained a pink powder throughout heat treatment.

4.3.15 Rhodium Oxide

Rhodium oxide was formed in an amorphous phase initially and became more clearly Rh_2O_3 after heat treatment at 400°C. The nanocrystal final size was approximately 4.0 nm (Fig 4-15). The particles were black after heat treatment.

4.3.16 Nickel Oxide

Nickel hydroxide $Ni(OH)_2$ phase was formed immediately as prepared, and was converted to the NiO phase through heat treatment at 400°C. The final NiO formed was 9.6 nm (Fig 4-16). The particles began as a bluish-green powder, and became dark black after heat treatment.

4.3.17 Iron Oxide

Iron oxide hematite Fe_2O_3 phase was formed immediately as a mixed phase with iron oxide hydroxide FeO(OH), and remained in this mixed phase through heat treatment at 400°C. The nanocrystals of Fe_2O_3 grew to 1.4 nm over the course of heat treatment (Fig 4-17). The particles began as an orange powder, and became slightly darker after heat treatment.

4.3.18 Copper Oxide

Copper Hydroxide $Cu(OH)_2$ phase was formed immediately as prepared, and transformed to the CuO phase through heat treatment at 400°C. The nanocrystals grew to 22.7 nm for the oxide over
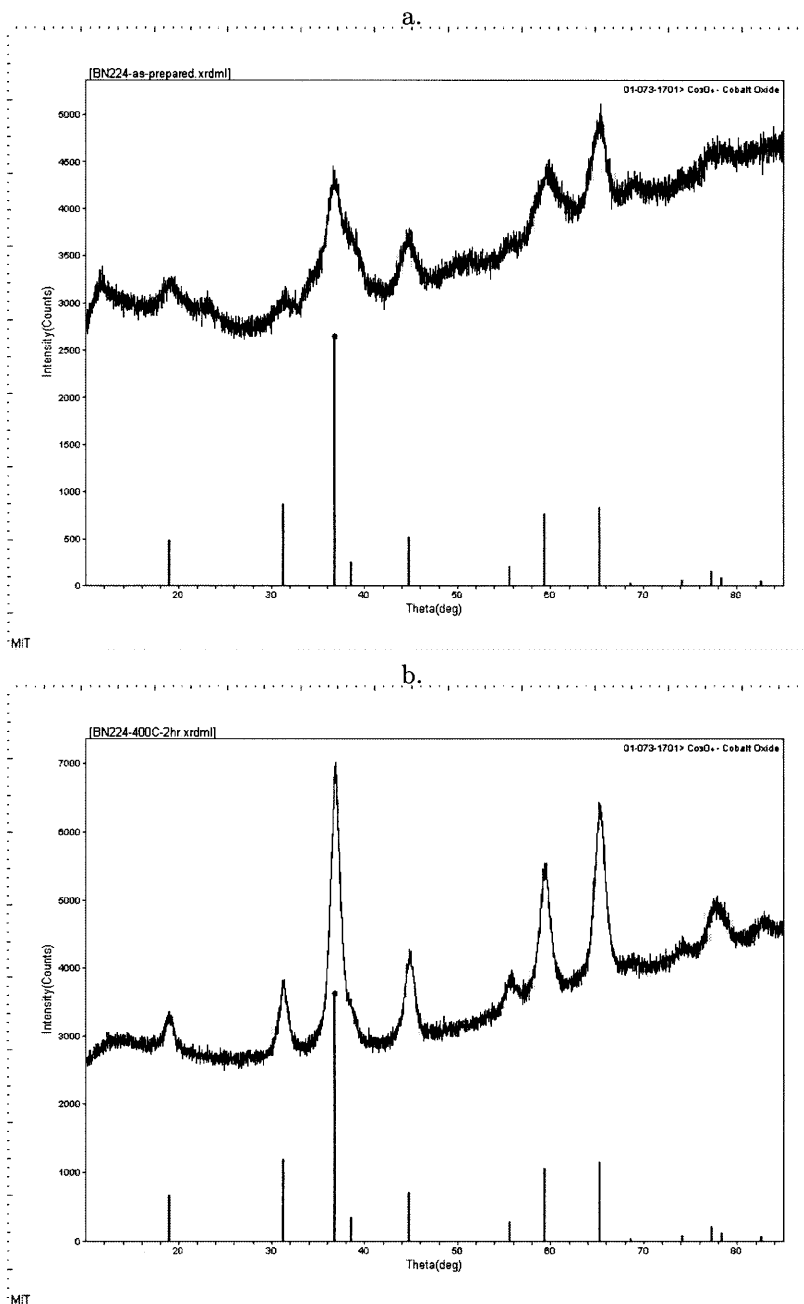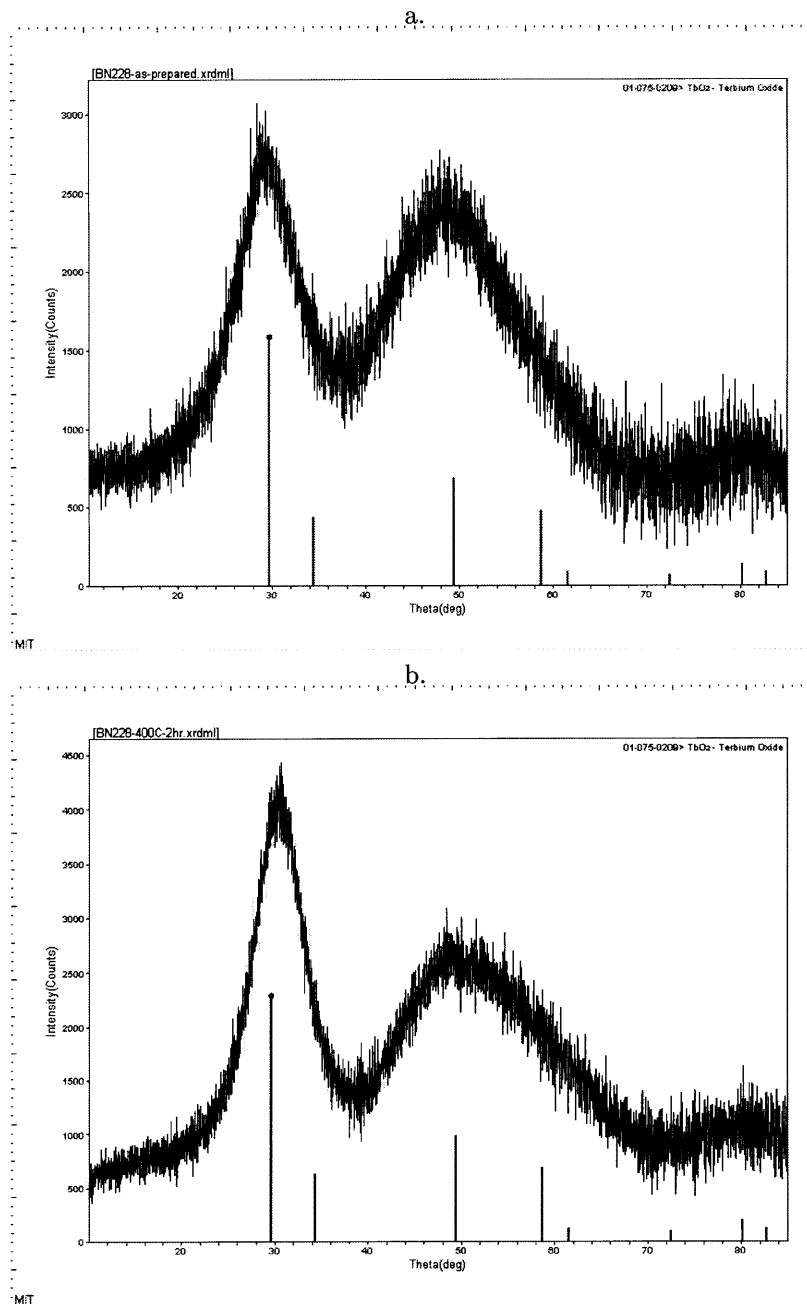
Figure 4-12: XRD from 10-85 degrees of Yttrium Oxide before and after heat treatment. a) As prepared. b) After heat treatment at 400°C for 2 hr. The lines corresponding to Y_2O_3 are shown for comparison.

Figure 4-13: XRD from 10-85 degrees of Dysprosium Oxide before and after heat treatment. a) As prepared. b) After heat treatment at 400°C for 2 hr. The lines corresponding to Dy_2O_3 are shown for comparison.

Figure 4-14: XRD from 10-85 degrees of Erbium Oxide before and after heat treatment. a) As prepared. b) After heat treatment at 400°C for 2 hr. The lines corresponding to Er_2O_3 are shown for comparison.
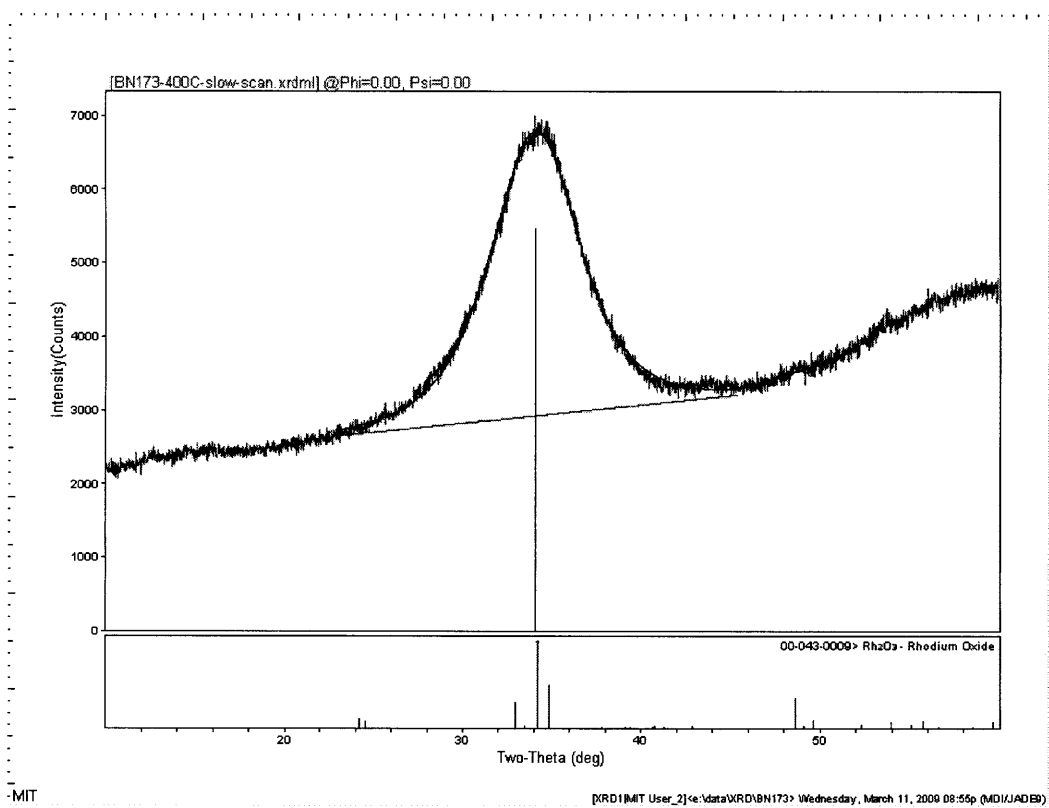
Figure 4-15: XRD from 10-60 degrees of Rh_2O_3 after heat treatment at 400°C for 2 hr. The lines corresponding to Rh_2O_3 are shown for comparison. The sample was amorphous immediately after synthesis.

a.

[BN162 10-80 14min.xrdml]

00-014-0117> Theophrastite - Ni(OH)₂

b.

[BN174-400C-slow-scan.xrdml]

00-047-1049> Bunsenite - NiO
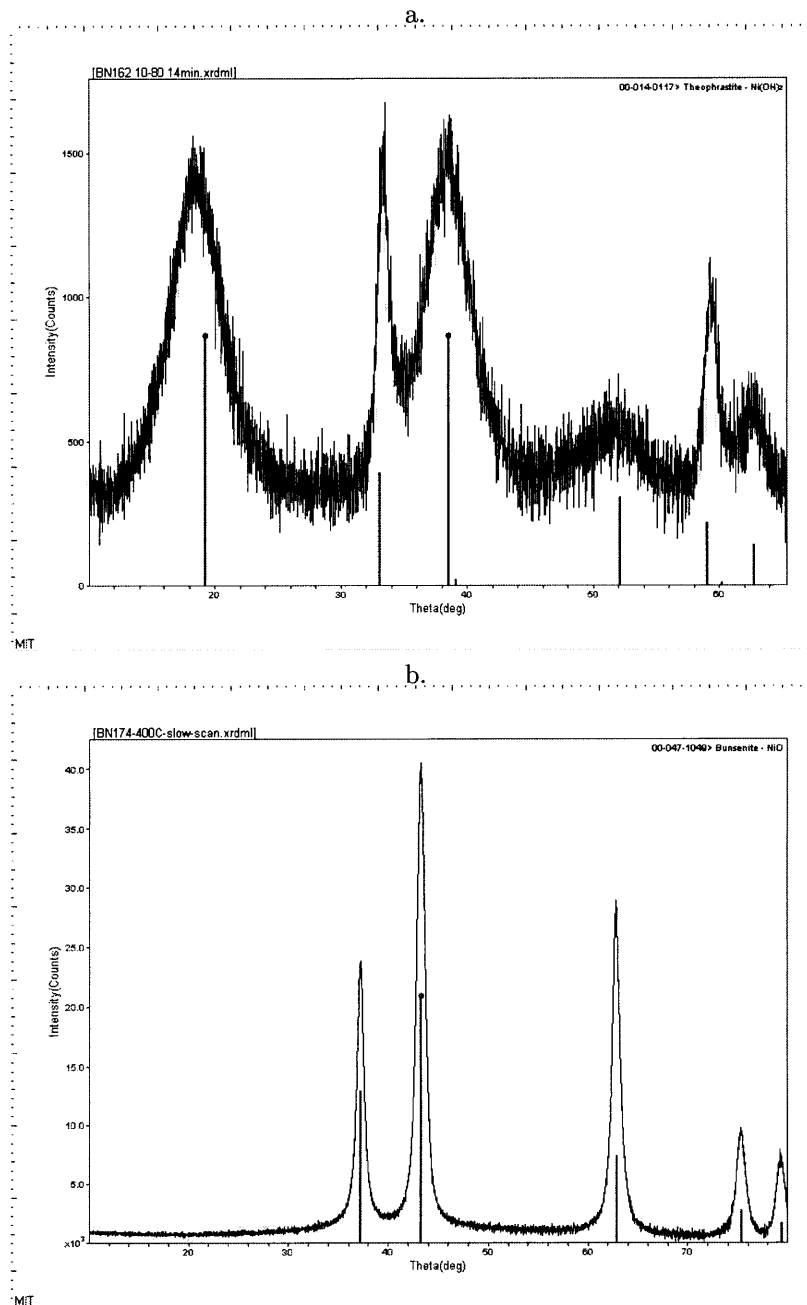
Figure 4-16: XRD from 10-65 degrees of Nickel Hydroxide before heat treatment, and the Nickel Oxide formed after heat treatment from 10-80 degrees. a) As prepared. b) After heat treatment at 400°C for 2 hr. The lines corresponding to Ni(OH)₂ are shown for (a) and the lines corresponding to NiO are shown for (b) for comparison.
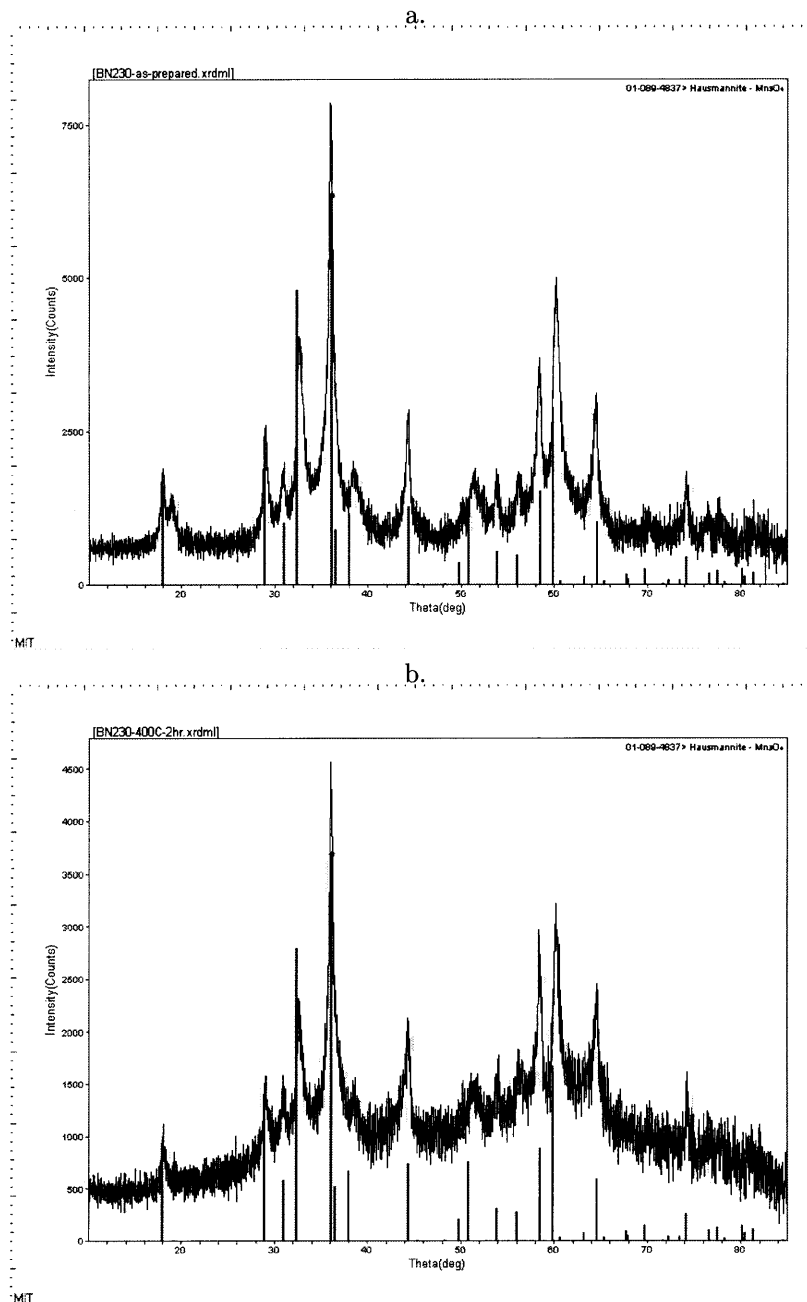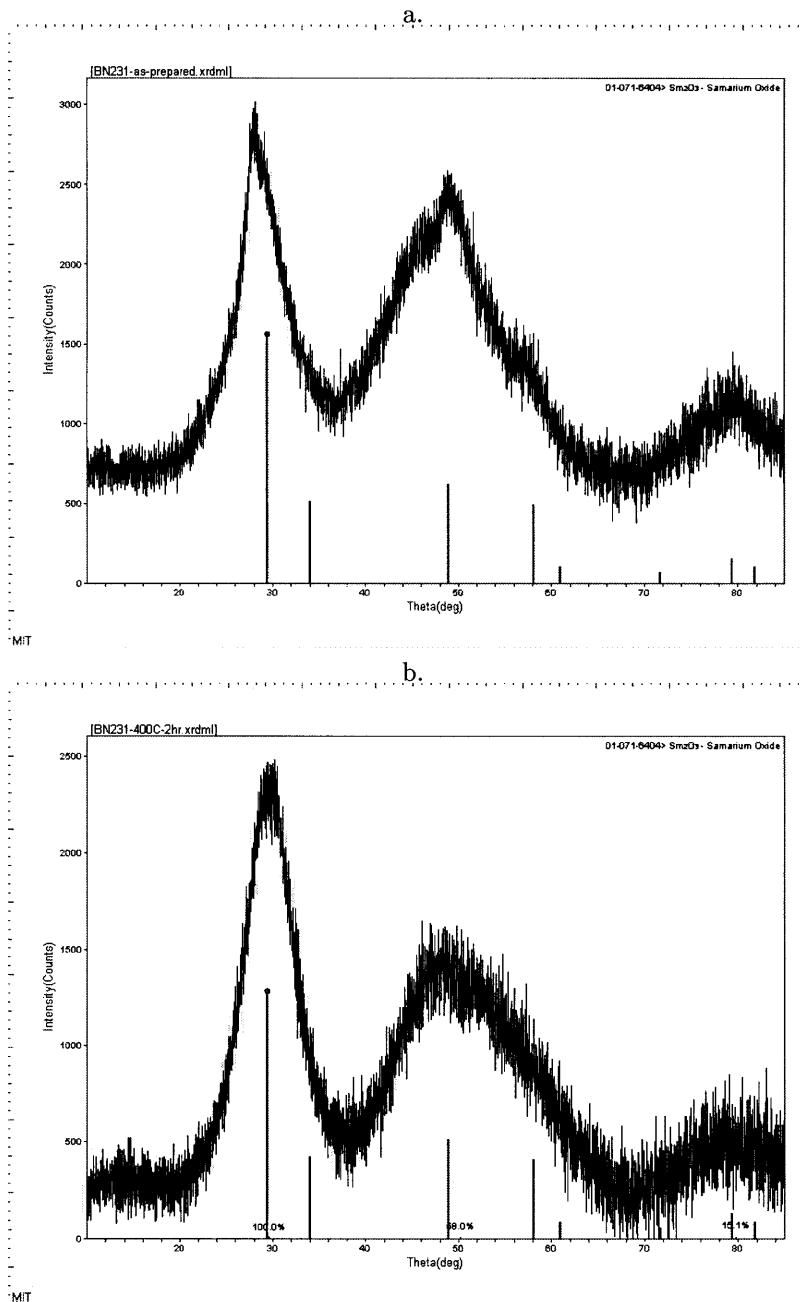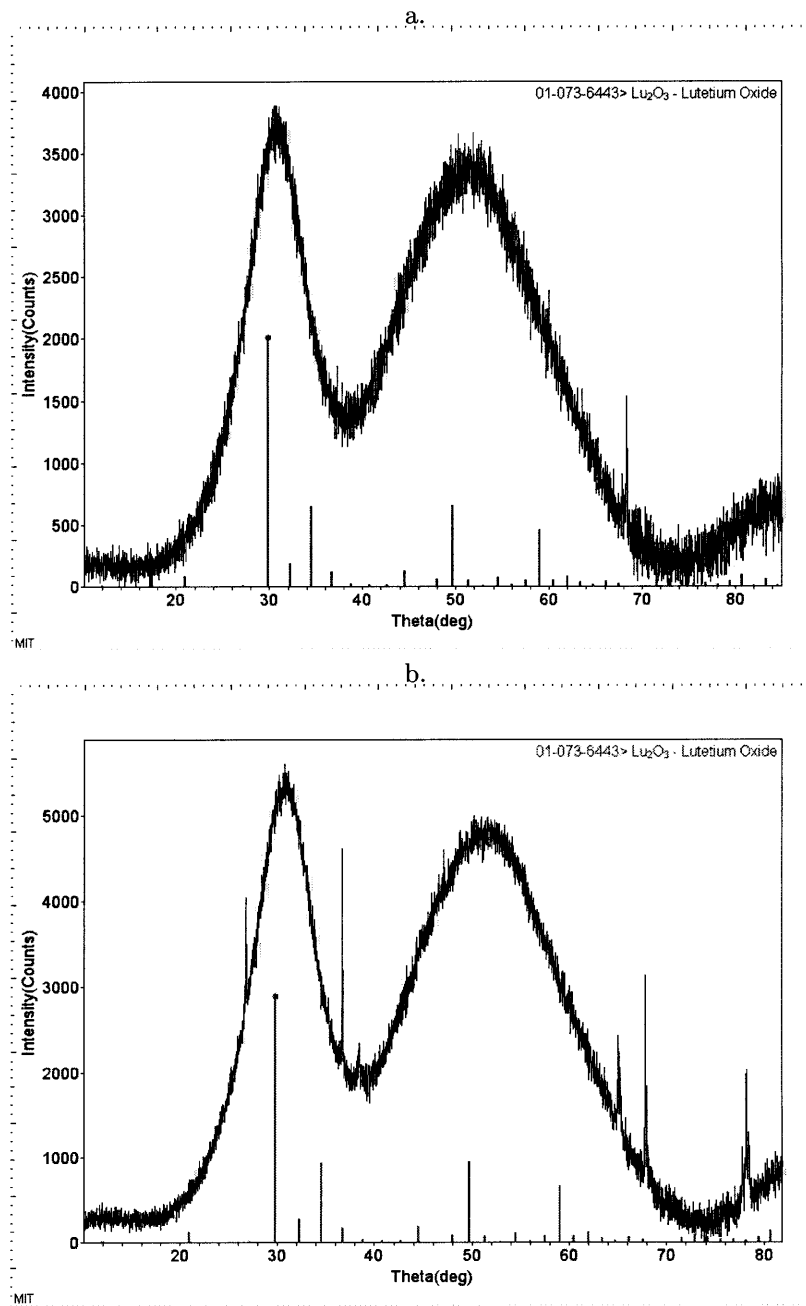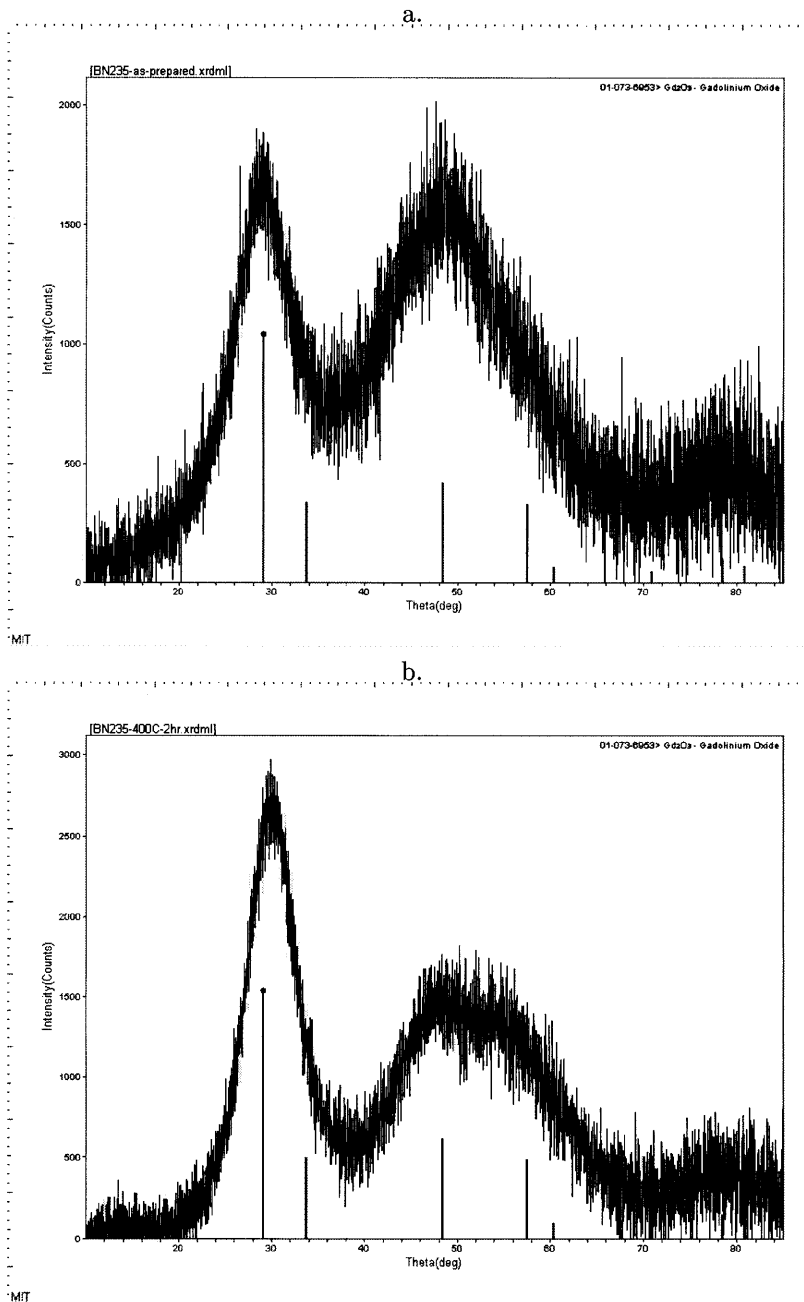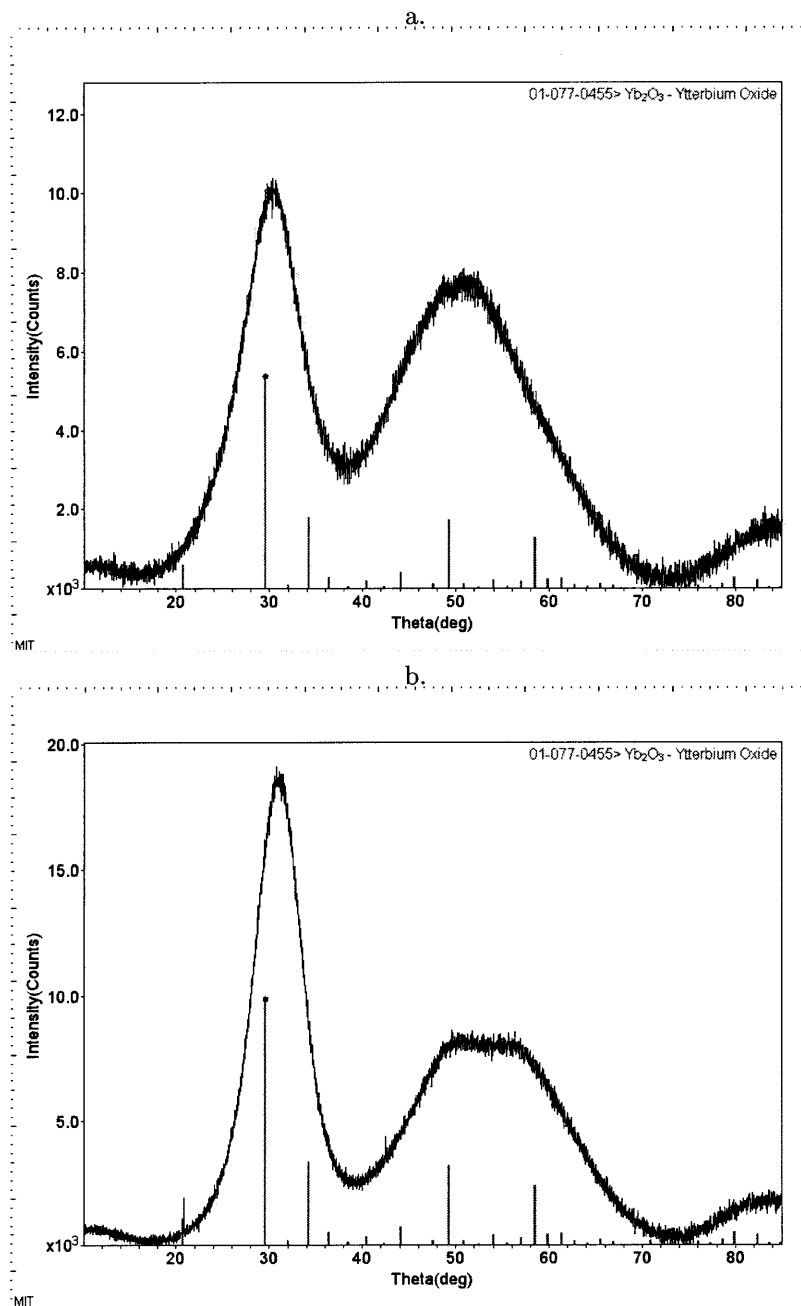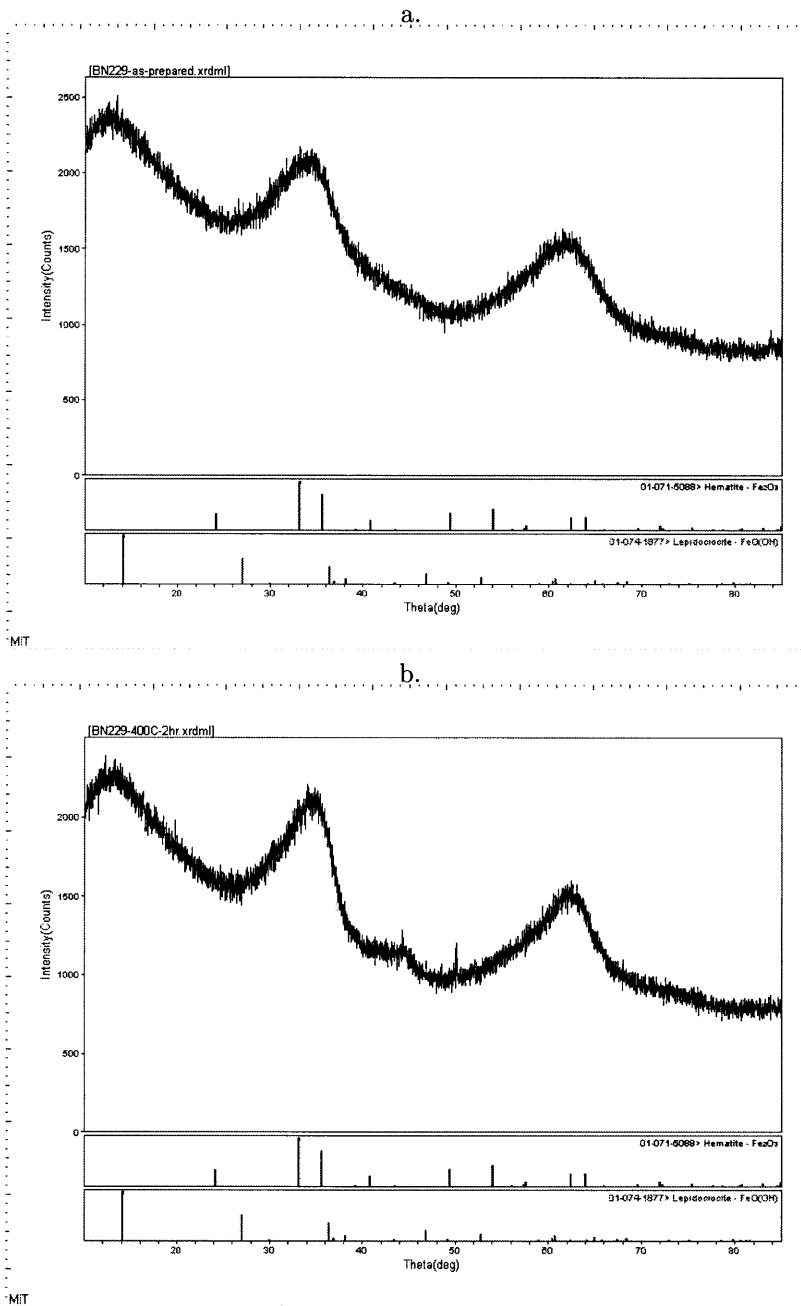
Figure 4-17: XRD from 10-85 degrees of Iron Oxide before and after heat treatment. a) As prepared. b) After heat treatment at 400°C for 2 hr. The lines corresponding to Fe_2O_3 (top) and $FeO(OH)$ (bottom) are shown for comparison.

the course of heat treatment (Fig 4-18). The particles began as a bright blue powder, and became a dark black powder after heat treatment.

4.3.19 Zinc Oxide

Zinc Oxide (ZnO) was formed initially, but the powder was a highly mixed phase containing a number of materials. After heat treatment, the impurity phases disappeared, and only ZnO peaks are visible from XRD. The nanocrystals had a final size of 16.3 nm (Fig 4-19). The powder was a white powder before heat treatment, and developed a pale yellow tint after heat treatment.

4.3.20 Lanthanum Oxide

Lanthanum Hydroxide phase was formed immediately as prepared, and remained in the $La(OH)_3$ phase through heat treatment at 400°C. The nanocrystals started at 13.0 nm, and grew to 21.0 nm over the course of heat treatment (Fig 4-20). The particles began as a pale yellow powder, and became white after heat treatment.

After further heat treatment at 800°C, the particles were transformed to a mixture of primarily La_2O_3 and LaOCl.

4.3.21 Neodymium Oxide

A mixed phase of neodymium hydroxide $Nd(OH)_3$ and neodymium oxide chloride NdOCl was formed immediately as prepared, on top of an unidentifiable amorphous fraction which made up roughly 60% of the material. Upon heat treatment at 400°C, the amorphous fraction increased to the majority phase representing a characteristic nanocrystallite size of approximately 1 nm (Fig 4-21).

After further heat treatment at 800°C, the particles converted to primarily one of the two phases of Nd_2O_3 with an impurity of NdOCl. Because the amorphous fraction is completely gone after high temperature heat treatment, it is likely that the amorphous fraction was the Nd_2O_3 nucleating in the existing hydroxide particles, which then grew into the peaks missing at 400°C. The product was initially a pale blue and became slightly darker upon heat treatment.

4.3.22 Praseodymium Oxide

Praseodymium hydroxide $Pr(OH)_3$ phase was formed immediately as prepared, and was partially converted to PrO_2 phase after heat treatment at 400°C (Fig 4-22). The product began as a white powder, which became brown upon heat treatment, although to a visual inspection the powder was mixed brown and white. The powder was remixed for analysis, but it is likely that a longer heat treatment period would be sufficient to convert the white hydroxide phase to the brown oxide phase.
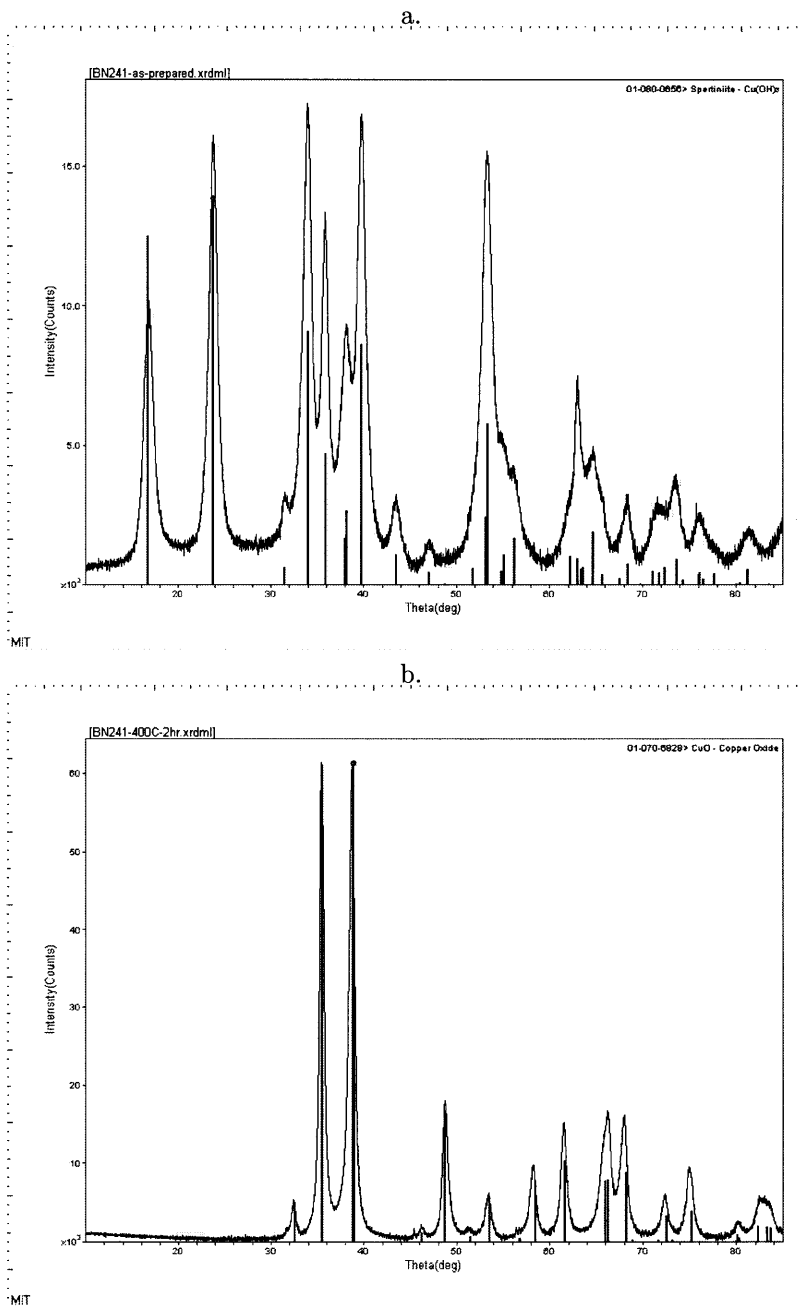
Figure 4-18: XRD from 10-85 degrees of Copper Hydroxide before and Copper Oxide after heat treatment. a) As prepared Copper Hydroxide. b) Copper Oxide after heat treatment at 400°C for 2 hr. The lines corresponding to $Cu(OH)_2$ (a) and CuO (b) are shown for comparison.
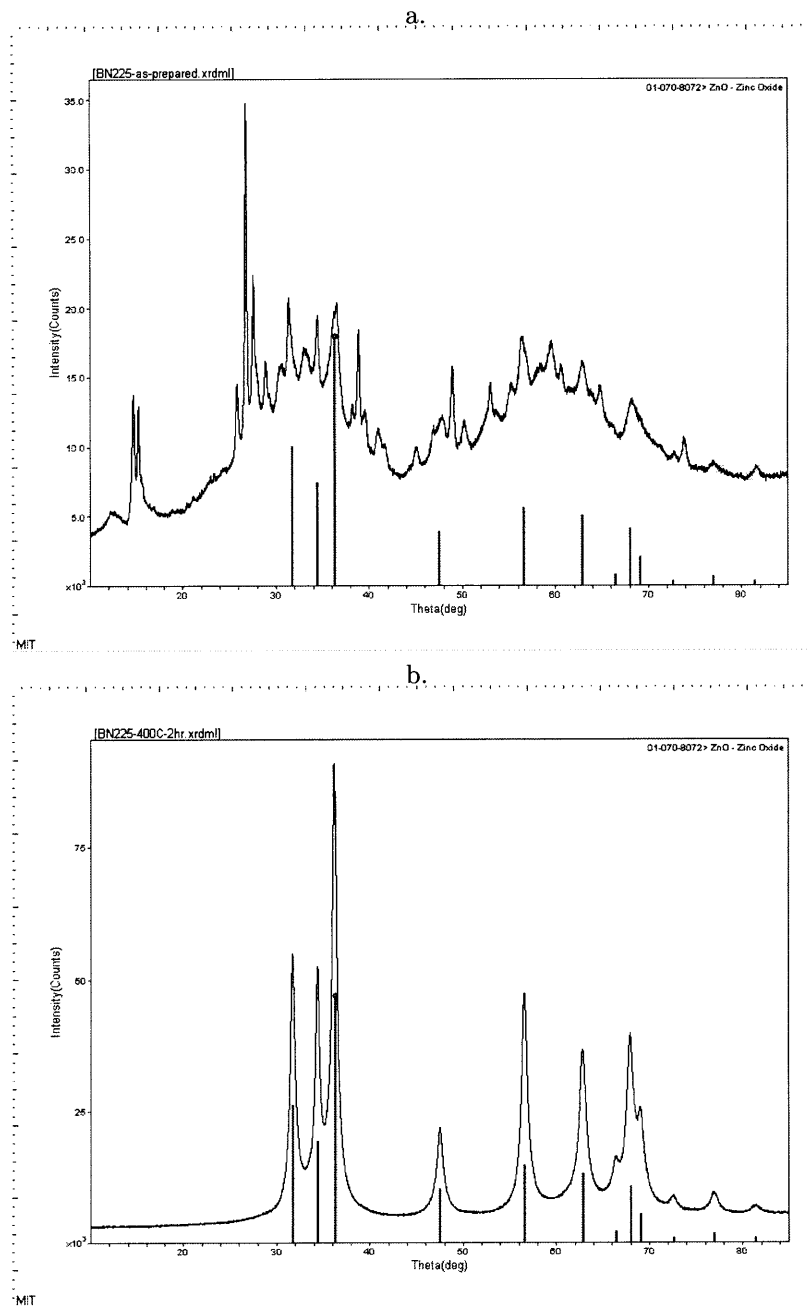
Figure 4-19: XRD from 10-85 degrees of Zinc Oxide before and after heat treatment. a) As prepared. The ZnO peaks are present, but there are many unidentified peaks indicating a highly mixed phase. b) After heat treatment at 400°C for 2 hr, the unidentified peaks have vanished. The lines corresponding to ZnO are shown for comparison.
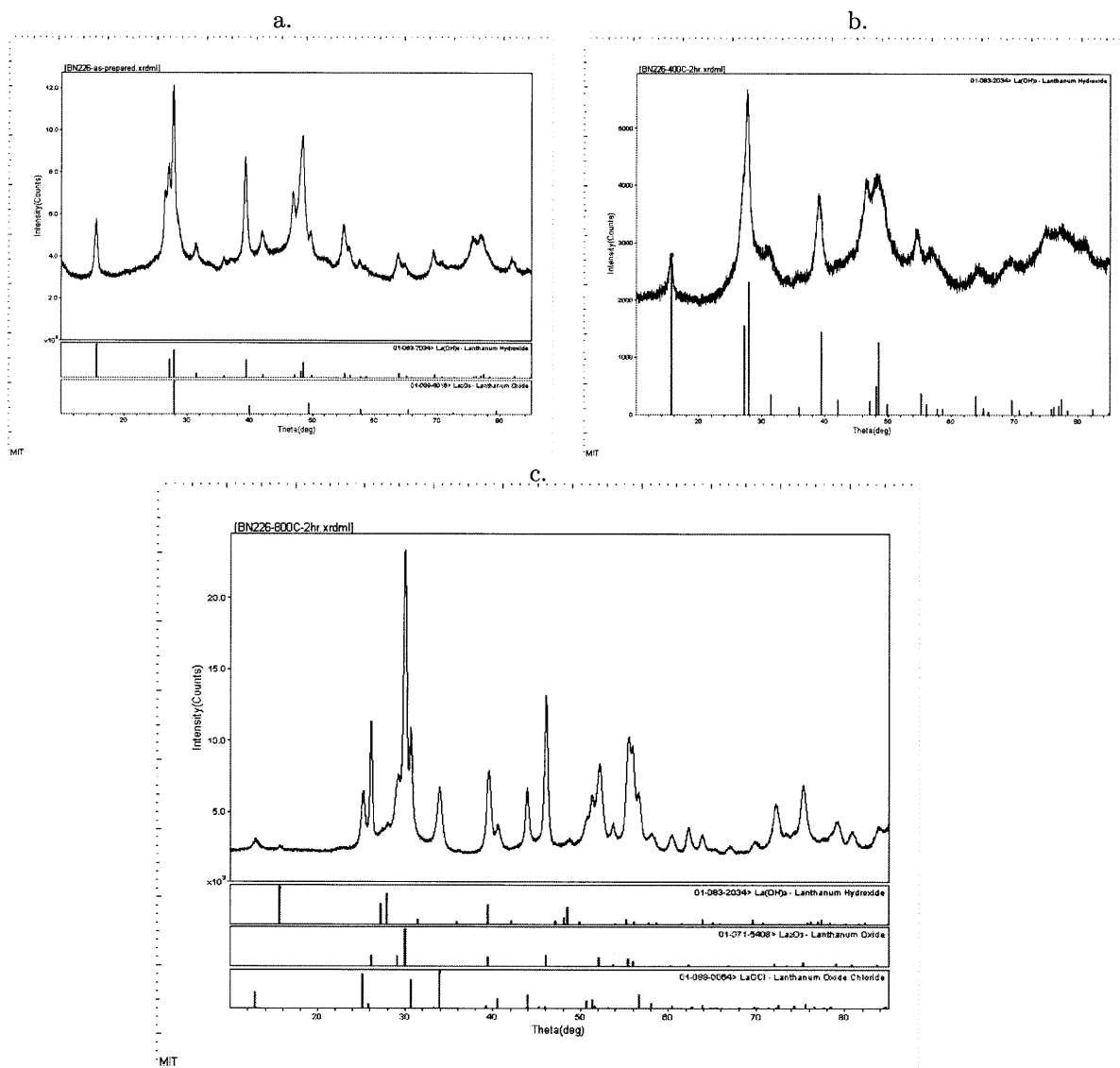
Figure 4-20: XRD from 10-85 degrees of Lanthanum Oxide before and after heat treatment. a) As prepared. b) After heat treatment at 400°C for 2 hr. The lines corresponding to La(OH)$_3$ are shown for comparison. c) After heat treatment at 800°C for 2 hr with corresponding lines for La(OH)$_3$, La$_2$O$_3$, and LaOCl shown for comparison.
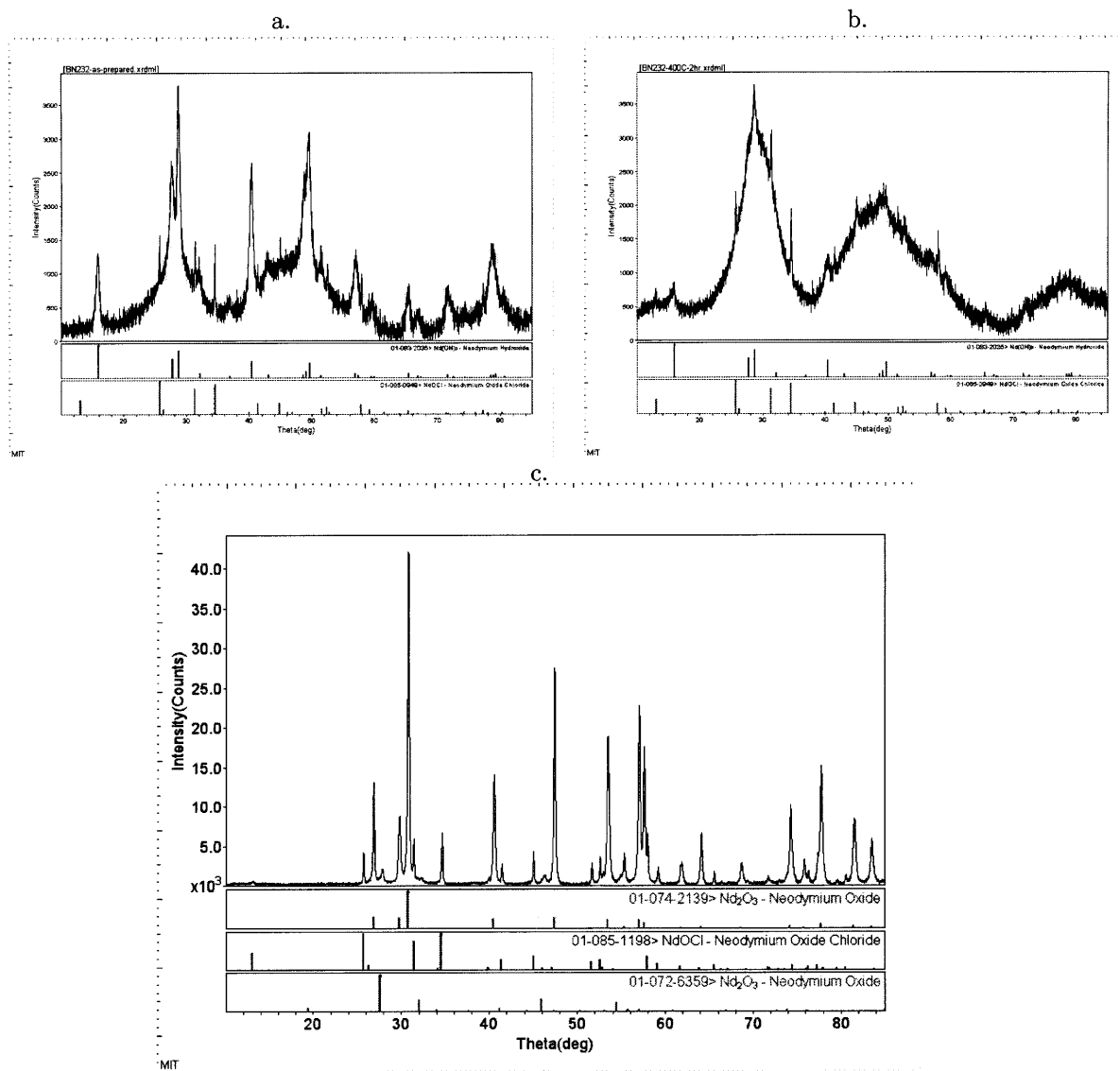
Figure 4-21: XRD from 10-85 degrees of Neodymium Oxide before and after heat treatment. a) As prepared. b) After heat treatment at 400°C for 2 hr. The lines corresponding to Nd(OH)₃ and NdOCl are shown for comparison. c) After heat treatment at 800°C for 2 hr with corresponding lines for the two Nd₂O₃ phases as well as NdOCl shown for comparison.
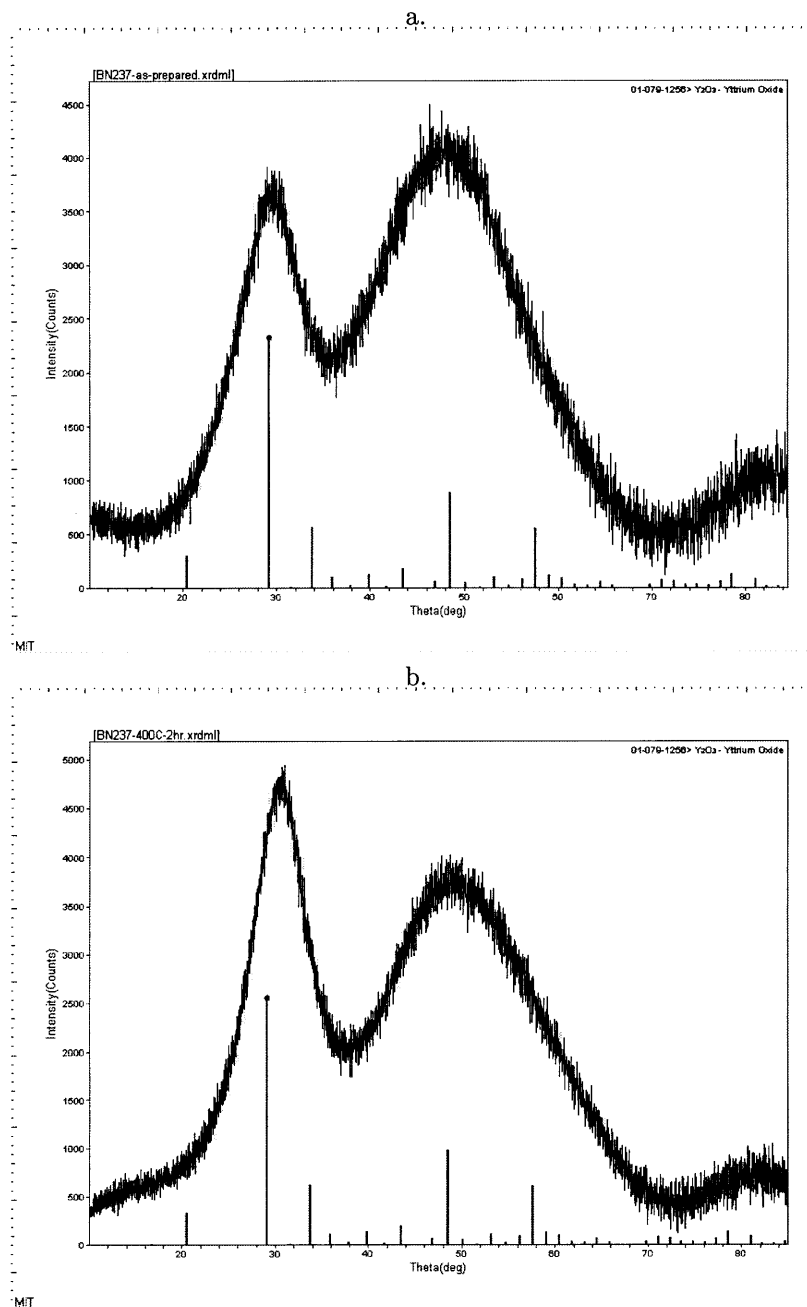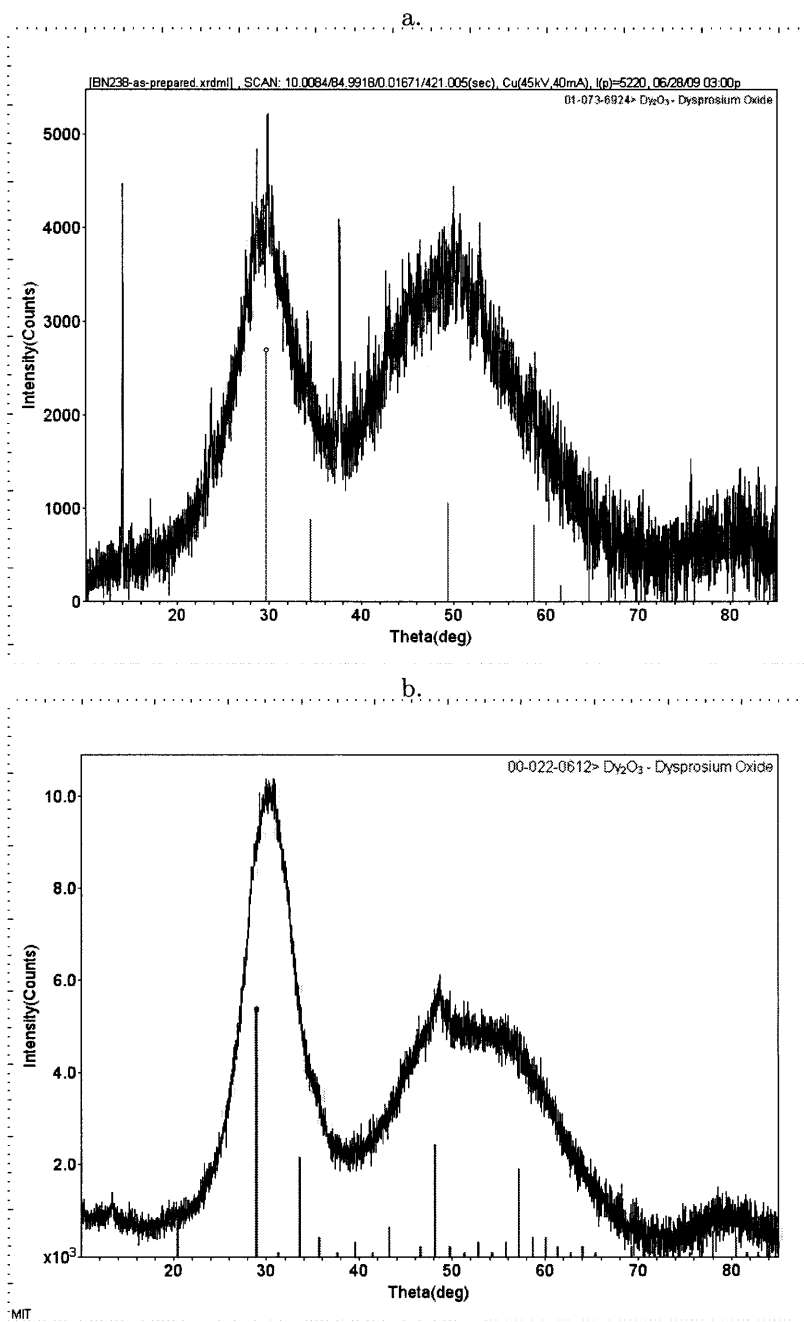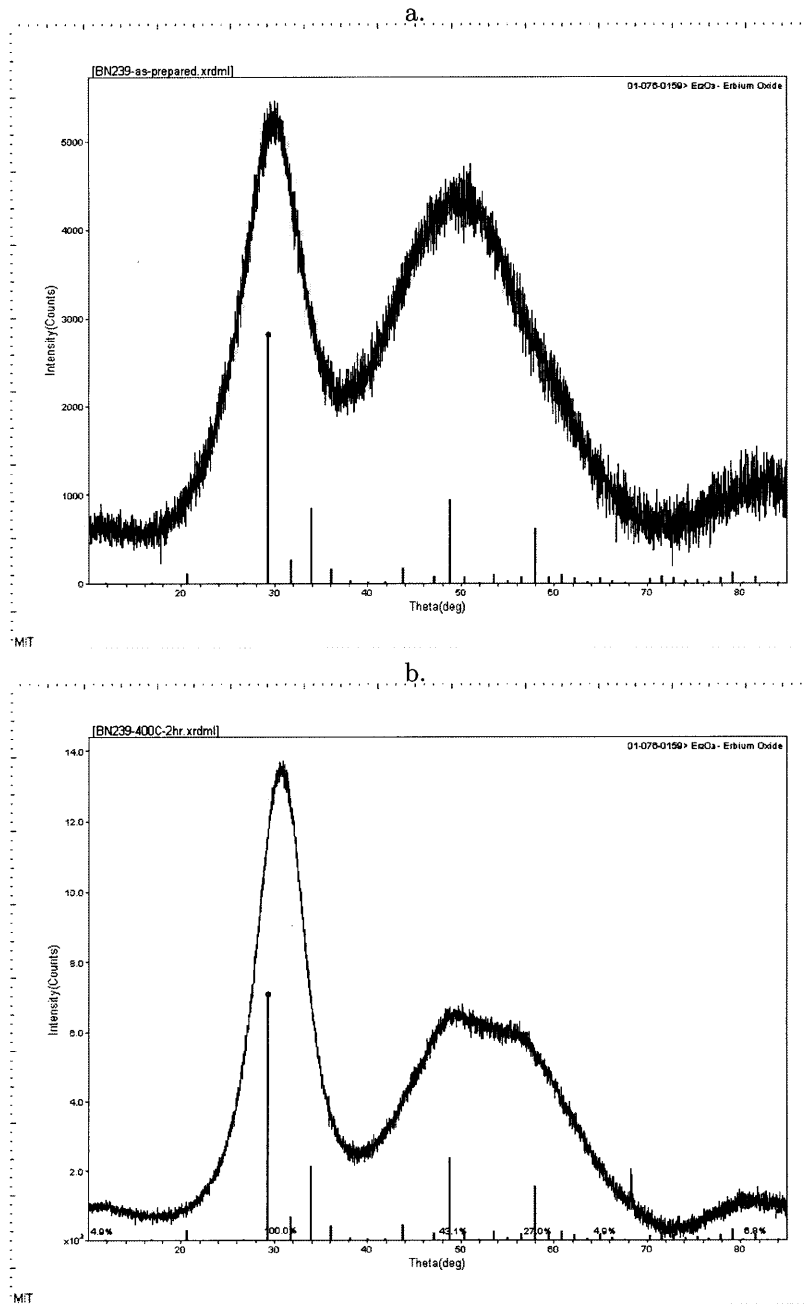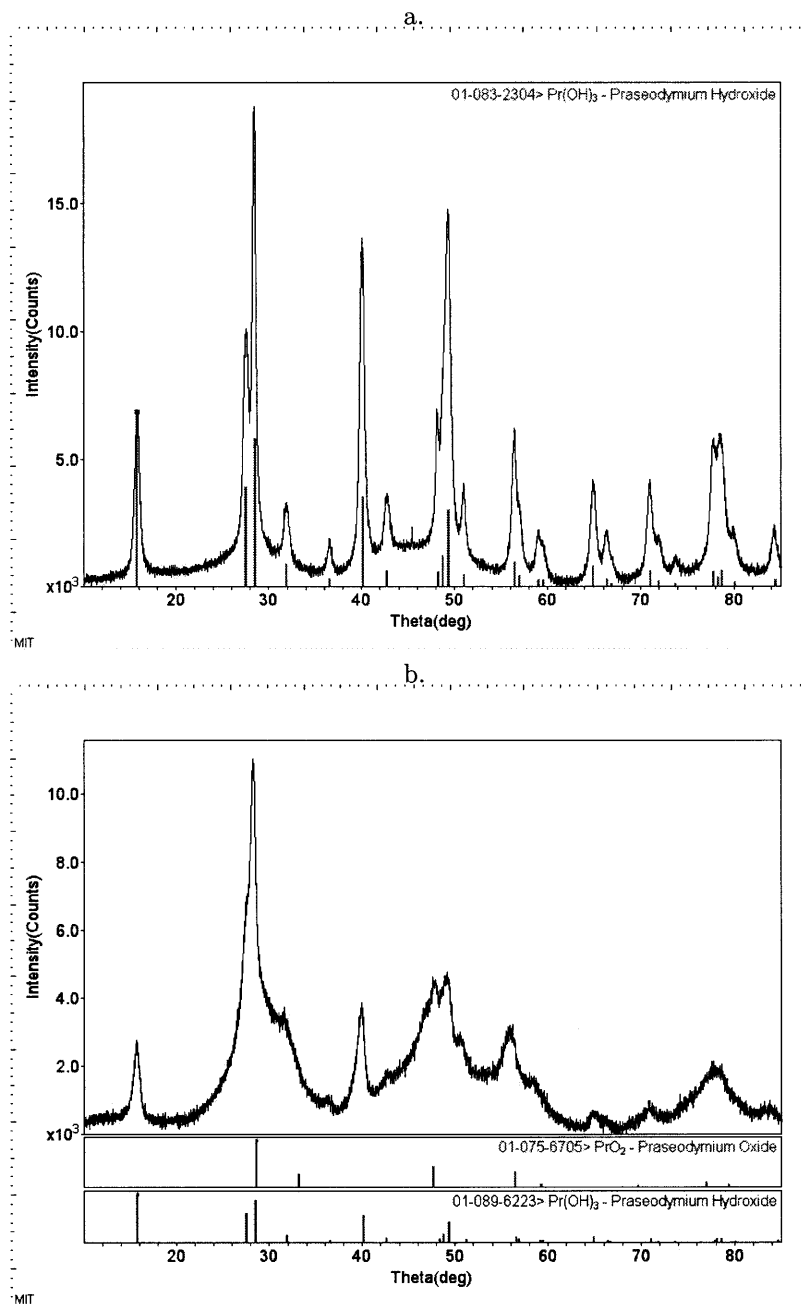
Figure 4-22: XRD from 10-85 degrees of Praseodymium Oxide before and after heat treatment. a) As prepared. b) After heat treatment at 400°C for 2 hr. The lines corresponding to Pr(OH)$_3$ and PrO$_2$ are shown for comparison.

4.4 Summary

We have demonstrated an extremely simple method for producing very small nanocrystals of a very wide range of metal oxides in aqueous solution using only mild precursors. Each material was characterized with XRD before and after heat treatment to show the different phases produced, and nanocrystal size was estimated by using the peak broadness.

This technique is primarily novel in the use of extremely high concentrations of hydrogen peroxide as a temporary capping agent. We suspect that the peroxide forms defects on the surface of forming nanocrystals, inhibiting particle growth while allowing or even encouraging particle nucleation. The result is substantially improved kinetics towards producing extremely small nanoparticles.

Due to the wide range of nanoparticles synthesized using the same method, it is also very likely that the reported syntheses can be mixed to great effect in order to produce highly nanocrystalline mixed material systems. Further, the materials reported in this work also represent a good starting set of compounds for future attempts at synthesizing complex single-phase ceramics.

Chapter 5

Development of Rh-nucleating Peptides

5.1 M13 Engineering

5.1.1 Traditional Phage Display

Phage display is a technique used all over the world to discover protein sequences with binding affinity for a particular, typically organic substrate. In the Belcher lab, we take this a step further and use bioengineering techniques to use the entire M13 bacteriophage resulting from phage display as a scaffold for the templating of desired inorganic materials.

The phage display process is one of directed natural selection, where an initial phage library will take wild-type M13 and use genetic manipulation to randomize a short sequence of amino acids expressed typically on the terminus of the virus. In the case of the commercially available phage libraries which we use made by New England Biolabs, we are inserting a 12-mer linear protein sequence into the p3 protein, or a 7-mer cyclical protein into the same p3 protein, which is then expressed on the terminus five times around a five-fold rotation axis which goes down the center of the virus.

The phage library is exposed to our materials to discover which sequences bind the best, the result is amplified to produce a new input phage library with decreased diversity but better average binding affinity, and after several rounds one or a few consensus sequences are found which will bind strongly to the substrate, as shown in Fig. 5-1. Typically, 3-5 rounds are required to reach a consensus sequence. In some cases, the sequence will also be capable of nucleating the material it was selected against.

Traditionally, the proteins discovered using phage display are used for affinity protein tagging
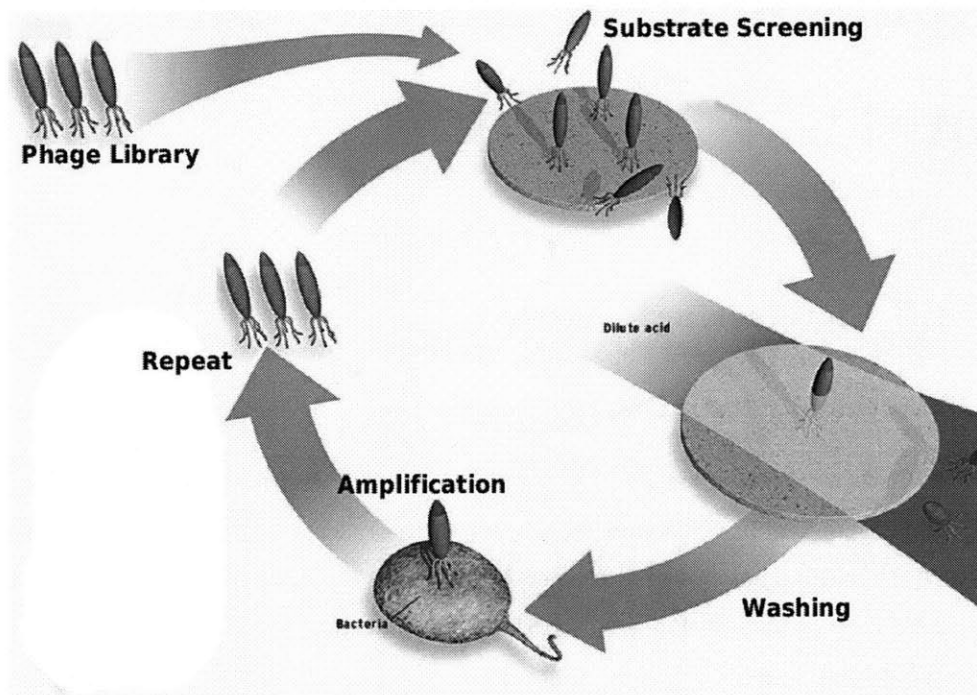
Figure 5-1: A cartoon showing the process of phage selection. First, the phage library is screened against the desired substrate and the weakly or non-binding phage are washed off. The resulting eluate is amplified in bacteria to produce a new input phage library with decreased diversity, but better average binding affinity, and the process is repeated until a strongly binding sequence is discovered.

and ligand pair discovery. More exotically, the proteins discovered using phage display can then be used in systems such as high pressure liquid chromatography (HPLC) to perform otherwise difficult separations for chirality.

5.1.2 Inserting Sequences into p8

In research which is fairly unique to the Belcher lab, instead of using the binding peptides as an affinity tag, we select for proteins which bind to inorganic materials or nanomaterials. Phage display techniques have been very successful to date and have been able to bind a wide variety of 2-6 and 3-5 semiconductor materials, as well as gold, cobalt oxide, sapphire, iridium oxide, iron oxide, lithium managanese compounds, cerium oxide, and a number of others. [54]

In order to make nanowires using proteins derived from a p3 library, the binding sequence is inserted into the end of a DNA sequence that produces the p8 major coat protein. This DNA sequence can be then inserted into a plasmid and produced in E. coli concurrently with phage reproduction to result in a small amount of "impurity" proteins in the major coat. Alternatively, the entire phage DNA sequence can be engineered to replace the naturally occurring p8 sequence with the engineered p8 sequence containing the discovered p3 binding sequence, producing phage with 100% expression of the engineered p8 protein.

This system is very flexible in that if desired, multiple types of hybrid p8 proteins can be inserted independently into the coat of the virus, allowing for the potential of adding in more than one type of binding protein into the phage coat.

5.1.3 p8 Phage Display

An alternative and complementary approach to causing binding or nucleation on the major coat protein of the M13 phage is to engineer a phage display library using a randomized p8 protein instead of a randomized p3 or p9 protein. This method is advantageous because it eliminates the possibility of phage produced using an inserted p3/p9 binding sequence in the p8 protein being non-viable. Phage which are not viable with 100% expression of the binding p8 protein will never be discovered because they will not be viable from the start.

This method is substantially more complicated in that the libraries are not commercially available and must be created in the lab. Additionally, this approach only easily allows for the expression of a protein at a 100% level — although it may be possible in the future to clone in multiple copies of the p8 sequence into the M13 DNA, it is not yet possible to control the relative expressions of multiple proteins. This is a great advantage for producing whole, structurally stable nanowires, but is a disadvantage when producing hybrid systems.

5.1.4   Mixing p8 Display with p3-p8 Phagemids

The best option in terms of balancing complexity with versatility is to use several of the above described methods. For example, a p8 protein is found using either p8 phage display or p3 insertion into p8 into the full phage genome which is capable of either binding or nucleating the material of interest. This phage is treated as the new standard phage, and has 100% expression of the binding sequence on the surface.

Next, one or several p3 binding sequences are found, each of which is specific for a desired "impurity" material to be expressed in the final virus as p8 protein at a level of about 3-10%. The p8 protein derived from the discovered p3 sequence is then inserted into a plasmid for concurrent production along with infection of the standard phage.

This allows you to nominally take a strain of E. coli which will produce binding affinity at a 3-10% level for a particular material, for each material you may be interested in, along with a strain of M13 developed using a p8 library to ultimately produce a primary scaffold of another material, and enables you to combine them combinatorially to produce a wide variety of mixed systems.

For example, if you take E. coli with a phagemid to produce a protein that will bind to rhodium metal, and infect it with an M13 strain capable of nucleating CeO_2, the grown up M13 particles will primarily nucleate CeO_2, with about a 3% impurity of rhodium metal — precisely the system we are trying to make as a catalyst.

5.2   Experimental

5.2.1   Phage Display to Find a Rh-binding Sequence

The New England Biolabs Ph.D.-12 kit was used to find a binding sequence for rhodium metal ordered from Alfa Aesar in powder form, with negative selection done against cerium oxide pellets also ordered from Alfa Aesar. One round of selection was done as follows.

1. Place a cerium oxide pellet into an epindorph tube.

2. Place 10 μL of phage library directly onto cerium oxide pellet.

3. Incubate for ~30 minutes, collect supernatant and discard binding phage.

4. Place 50 mg of rhodium metal powder into epindorph tube and add supernatant containing phage library which did not bind to cerium oxide. Add TBS with Tween soap to make binding more difficult.

5. Incubate for 60 minutes.

BN208-18	H	F	**G**	S	Q	**L**	R	Y	H	S	E	**L**
BN208-19	H	E	S	F	W	Y	**L**	**P**	H	Q	S	Y

Table 5.1: Comparison of groups on the two consensus sequences for binding rhodium metal. Red - Positive Charge. Green - Negative Charge. Blue - Nucleophilic. Cyan - Aromatic. Violet - Amide. **Black** - Hydrophobic.

6. Centrifuge and remove supernatant to discard non-binding phage. Wash several times with Tween-TBS solution.

7. Elute bound phage using non-specific disrupter, and centrifuge to remove the rhodium powder. After removing rhodium powder, neutralize the acidic solution used to eluate phage.

8. Amplify eluate to create input library for the next round of panning, increasing the stringency of the selection (higher concentration of Tween soap, decreased binding time, longer washin time) each time until a consensus sequence is found.

Two primary sequences were displayed in the third round of selection, HESFWYLPHQSY and HFGSQLRYHSEL. The two sequences are shown graphically in Table 5.1 with the functional groups labeled. Of particular interest is that in both sequences, H is found in the same position, and in both sequences, S is found in very close positions. Further, the overall charge of both sequences is positive, which is unexpected considering that rhodium will typically accept electrons in binding events.

5.2.2 Testing Nucleation Capacity

The M13 phage as a whole has a mass of approximately 16 million daltons, while expressing only five binding/nucleation sites. Thus, for nanopartices in the 3-10 nm size range, a nucleating protein would produce a final system with approximately 10^{-3} rhodium compared to the phage. To further complicate things, the phage is invisible to TEM, so telling whether a particle has been nucleated on the p3 protein is very difficult, if you can find the particles at all — the overall number of particles is very small, so only a handful would be present on the TEM grid.

XRD Detection of Nucleated Particles

It has been impossible to use XRD to detect nucleation events on p3 proteins due to the tiny fraction of the total material present which would show the relevant peaks. This is largely because the amorphous signal from the phage swamps out the signal from any nanoparticles nucleated on the end.

However, with the use of more advanced equipment and using more sophisticated measurement techniques, we have successfully compared the two protein sequences found as consensus sequences for nucleation ability and found that one shows nucleation while the other does not. The XRD in
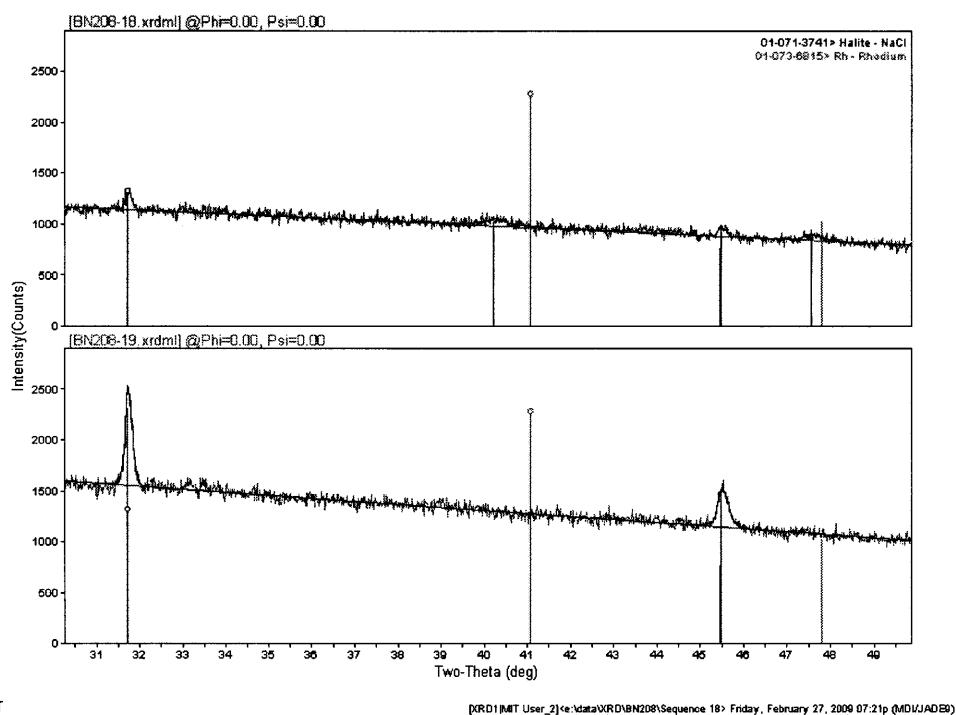
Figure 5-2: XRD Data showing a comparison between the two consensus sequences found in the third round of biopanning. Peaks less than one degree from the predicted locations for rhodium metal are seen in one measurement, but not the other, clearly indicating a difference in nucleation capacity. The sharper peaks are salt from residual TBS in the pellet after centrifugation. The top sequence is BN208-18, HFGSQLRYHSEL, and the bottom sequence is BN208-19, HESFWYLPHQSY

the relevant range is shown in Fig. 5-2. Comparing the 100% Rh peak area with the area of the entire amorphous hump (15-80°, only a section shown), the result suggests roughly 10^{-3} rhodium per phage (by approximately mass), which is in line with the predicted values assuming 5 binding sites per phage, and demonstrates the potential resolution of XRD in detecting minority phases against an amorphous background. The particles were roughly 15 nm in diameter, suggesting that the five binding sites may have combined to nucleate a single larger nanoparticle.

Chapter 6

CeO$_2$ Nanowires

6.1 Initial Nucleation using E3

Ki Tae Nam developed a strain of the p8 protein called E4, which expresses four glutamic acids on the surface of the major coat. This causes the coat to be highly negatively charged, causing it to readily bind and nucleate a wide range of metals and metal oxides from their positive ions in solution. Ki Tae used this to create a hybrid system containing gold nanoparticles inserted into a cobalt oxide nanowire. The E4 strain typically mutates to AEEE (E3) after a few amplifications, and E3 is used throughout this research in place of E4.

The use of this strain is very straightforward, and has been used to nucleate a wide range of nanowires in the Belcher lab. Initial attempts resulted in isolated phage with extremely good coverage as shown in Fig. 6-1 by incubating the E3 phage with CeCl$_3$ and then nucleating nanoparticles by adding NaOH and H$_2$O$_2$ in a similar manner to nanoparticles alone.

6.2 Nanostructural Dependence on Phage Concentration

6.2.1 Phage Concentration Series

After nucleation capacity was confirmed, the following experiment was devised to investigate the effect of phage concentration on nanostructure.

1. Amplify E3, a similar but degraded version of E4 containing only three copies of glutamic acid, to a concentration of $\sim 10^{14}$.

2. Add 500 μL of 1 mM CeCl$_3$ to an epindorph tube.

3. Add 100 μL of E3 phage with between 10^5 and 10^{12} phage particles added from amplified solution.
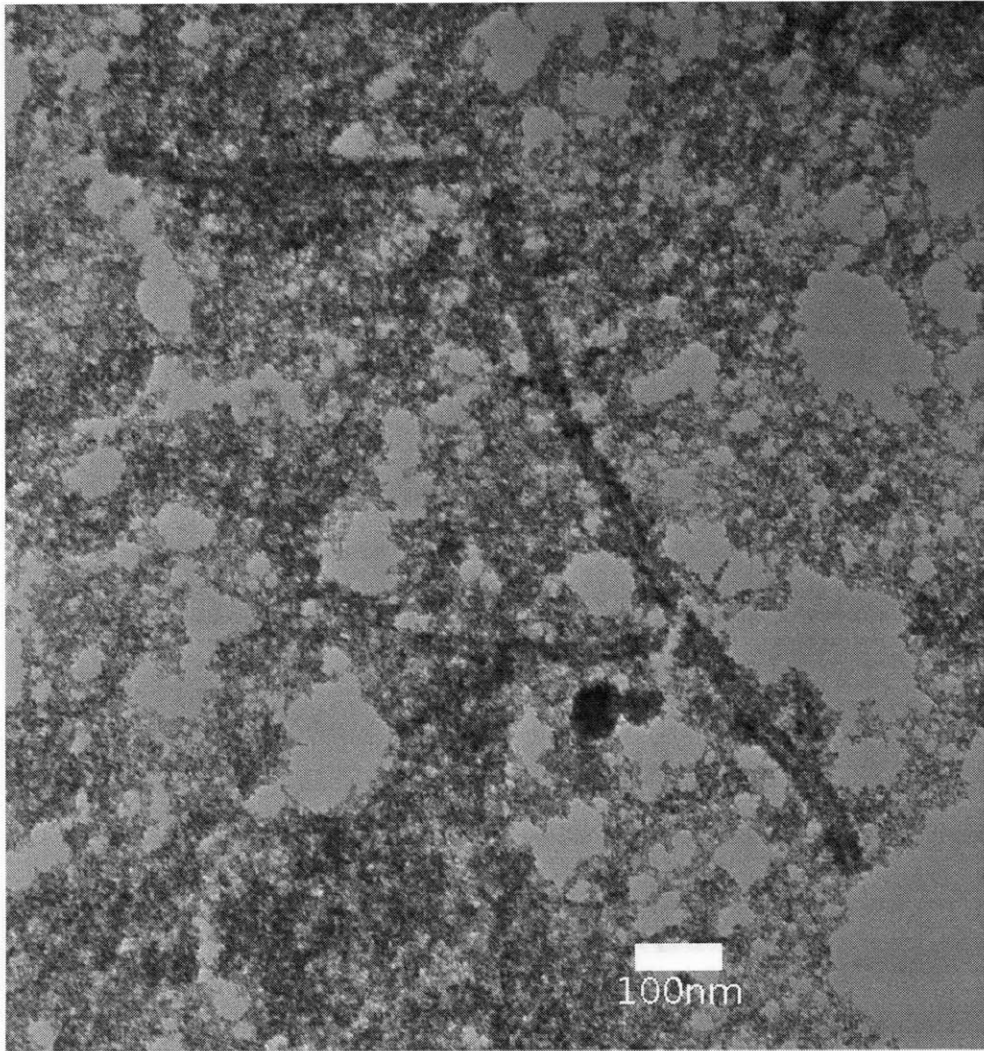
Figure 6-1: TEM of a CeO$_2$ nanowire produced with phage particles after a long incubation time. The empty thread down the center of the dark wire is the center of the virus, which is empty of material that has contrast under TEM.

4. Incubate for 10 minutes.

5. Add 50 μL of NaOH simultaneously with 1 μL 0.3 wt% H_2O_2 and immediately vortex to form wires.

6. Add 10 μL of solution to TEM grid for imaging.

As shown in Fig. 6-2, the structure of the material appeared to be dendridic even at concentrations of phage which should have been low enough to have no effect. However, there is what appears to be a phase transition at between 10^{10} and 10^{12} phage where the appearance goes from what appears to be a dendridic structure to a liquid crystal type structure where phage are forming a close-knit network and then nucleating particles on the surface. This is more apparent in zoomed in images as shown in Fig. 6-3. However, all samples still showed clear lattice fringes from CeO_2 nanoparticles as shown in Fig. 6-4.

6.2.2   Proposed Mechanism for Dendridic Growth

It is unlikely that this sort of dendridic structure would appear due to variations in the precursor solution, so we propose a true dendridic mechanism of growth in the cases of small amounts of phage. We suspect that the phage is forming a nanowire of CeO_2 rapidly compared to homogenous nucleation of phage in solution. The wire is very long compared to it's radial characteristic distance, forces a constraint on the dimensionality of any perturbations.

In the case of both a nanoparticle and a nanowire, as a perturbation appears, it will be unstable considering only diffusion effects because the perturbation front is now in a solution with a higher concentration of cerium ions than the interface which is lagging behind. Therefore, relative to the interface next to the positive perturbation, it will grow more quickly, the key requirement for dendridic growth. The newly formed dendrite will now comparitively rapidly "shoot out" from the core of the phage. Subsequently, the process can occur again on the newly formed dendrite, creating sub-dendrites until a "snowflake" style nanostructure is formed.

In the case of a spherical isolated nanoparticle, a perturbation on one side will result in a "pore" with a neck size with a fairly large solid angle defined by the ratio of the perturbation area to the surface area of the spherical nanoparticle. However, in the case of a nanowire, a perturbation will have a solid angle proportional to the ratio of the length of the pertubation around the circumference compared to the total circumerence — a much smaller amount, because the symmetry of the wire along the axial direction dictates that growth in that direction can be assumed to generally be blocked (Fig. 6-5). If diffusion is blocked from the -z direction at a particular angle, it will also be blocked from the +z direction, resulting in a lower solid angle for material to diffuse into the pore, and increasing the magnitude of the perturbation instability.
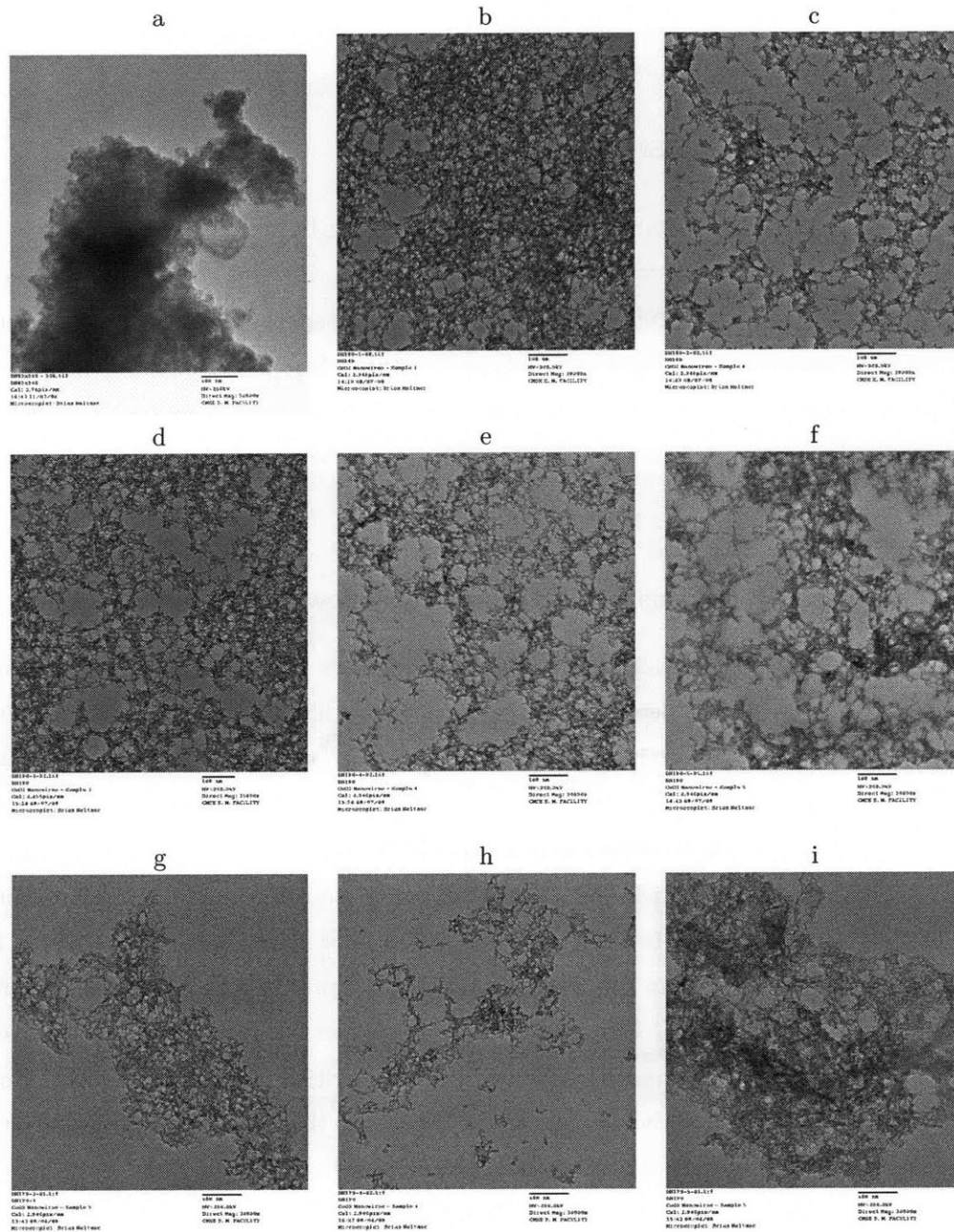
Figure 6-2: CeO$_2$ shown at varying phage concentrations and similar magnifications (100 nm scale bars) (a) No phage (b) At 10^5 particles, the phage appears to cause the structure to become more porous, but does not immediately cause a dendridic structure to be apparent. (c-h) 10^6-10^{11} particles respectively. In this concentration range, the dendridic structure becomes apparent, but there is no obvious change in the structure as phage concentration changes. (i) At 10^{12} particles, the structure appears to have completely closed up, and now very clear evidence of the phage liquid-crystal templating is visible – the CeO$_2$ appears to have a "worm-like" secondary structure.
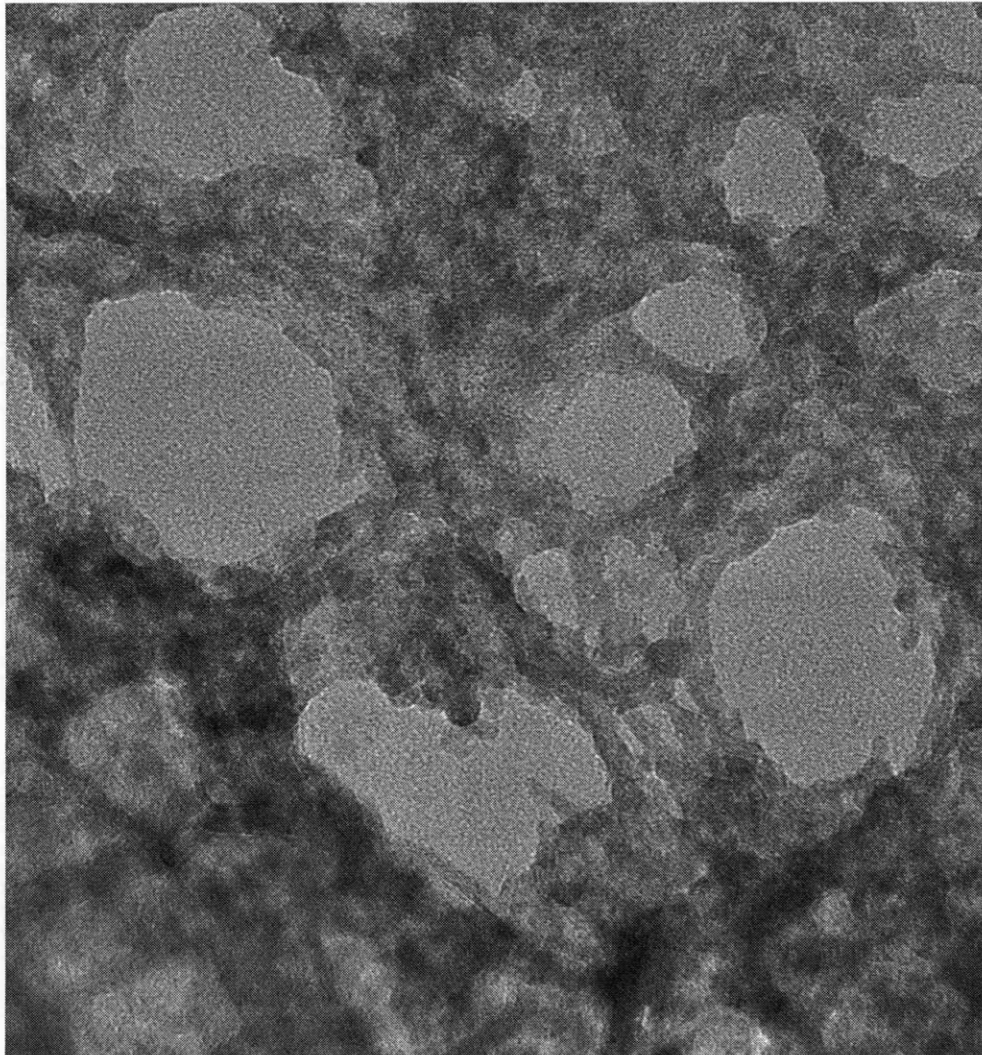
116

Figure 6-3: TEM of CeO_2 nanowires produced with 10^{12} phage particles in solution showing the liquid crystal structure. In several places, the phage can be identified by the thin hollow white line showing the core of the phage where no CeO_2 is present.
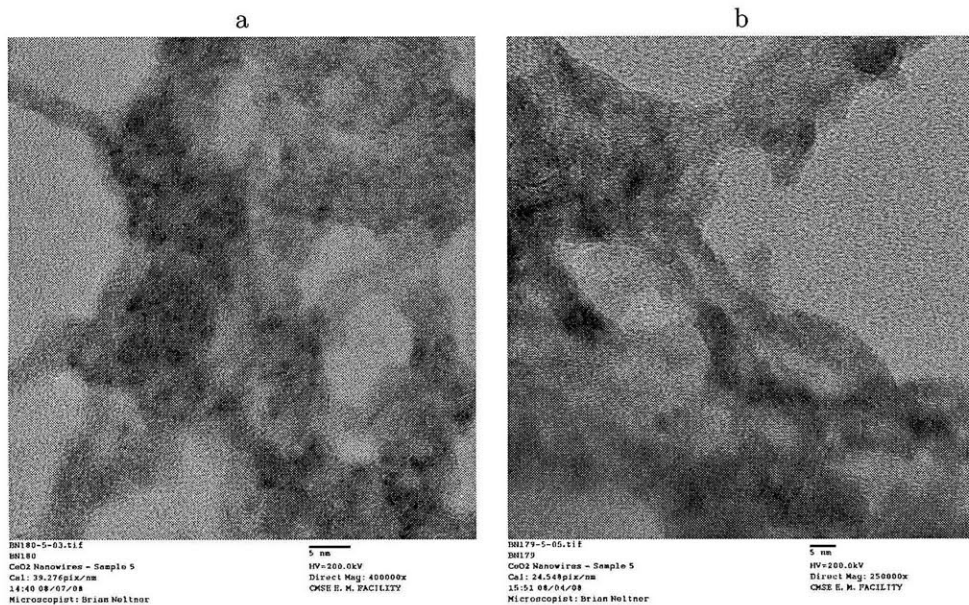
Figure 6-4: TEM showing the crystallinity of all nanowires. (a) With 10^9 phage particles. (b) With 10^{12} phage particles.
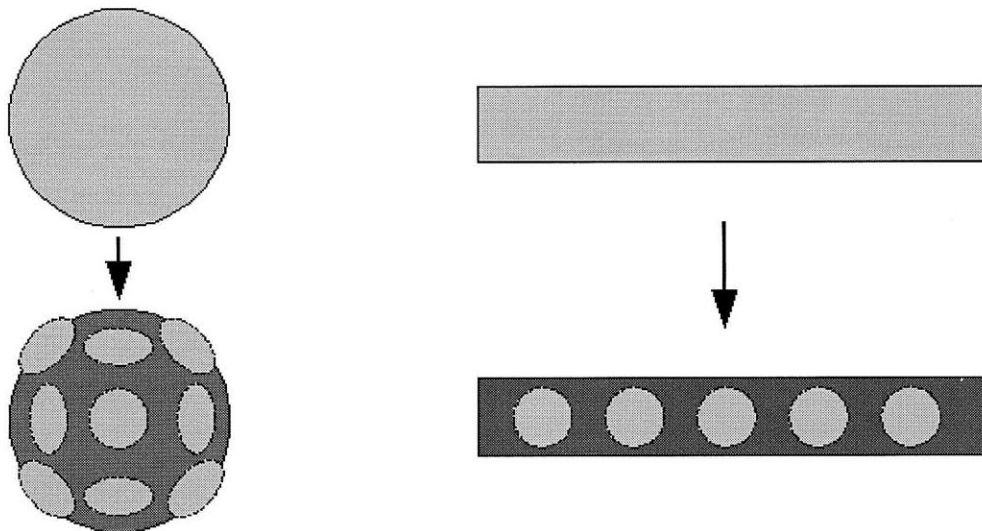
Figure 6-5: Cartoon showing the proposed mechanisms. On the left, in 3D the pores have a fairly wide solid angle between them from which new material can diffuse in. On the right, in 2D the pores are much more constrained due to the imposed initial axial symmetry in the system.
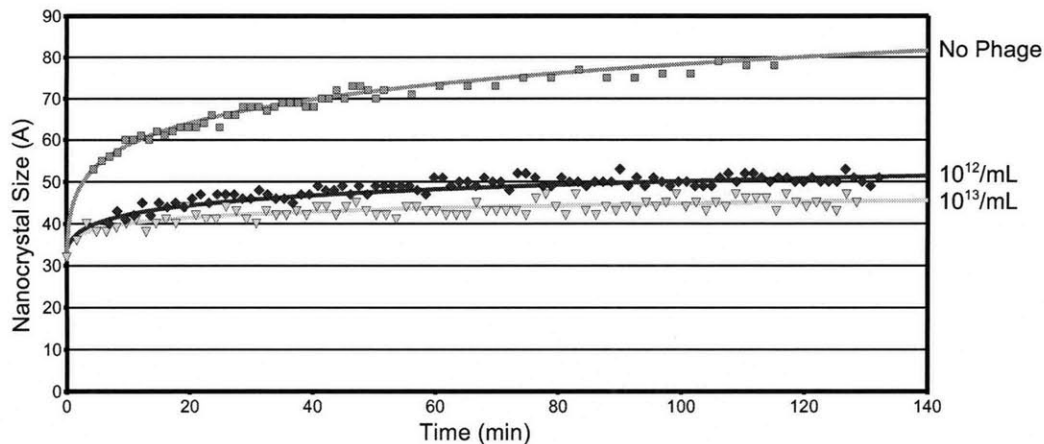
Figure 6-6: Thermal stability test of untemplated and M13-templated CeO_2 nanoparticles over three hours at 500°C in air. All particles were made at a 10 mM concentration of $CeCl_3$. From top to bottom, no M13 showing a growth exponent of 8, 10^{12} M13/mL showing a growth exponent of 13, and 10^{13} M13/mL showing a growth exponent of 21. This demonstrates that as more M13 is added the thermal stability of the CeO_2 crystallites improves.

The end result is that the neck size of the "pores" created by perturbations will be much smaller when formed on the nanowire than when formed on a nanoparticle. Thus, we propose that by seeding the solution with nanowires, a dendridic structure is formed which would otherwise be too slowly forming compared to diffusion to occur.

6.3 Thermal Stability

The nanowires formed with varying amounts of M13 phage for templating were analyzed for thermal stability by heating to 500°C using an in-situ furnace on the PANalytical X'Pert PRO diffractometer. Ceria crystallite size was estimated using the isolated {200} peak at 48 degrees, with approximately 1 min time resolution between measurements of crystallite size. The resulting crystallite sizes measured over two hours were fit using a power-law model of

$$D(t)^m - D(0)^m = k \cdot t \tag{6.1}$$

where D is the average nanocrystal diameter, m is the growth exponent, k is the rate constant for sintering, and t is the time. [71] This model showed suppression of ceria nanocrystal growth as more M13 is added during synthesis, with the growth exponent increasing from 8 with no M13 to 21 with 10^{13}/mL M13 and 10 mM metal precursor as shown in 6-6. The catalytic performance decreases as nanocrystallite size increases, making this improved thermal stability critical in creating a high-performance catalyst. [2–4, 43, 71]

Chapter 7

Production of Integrated Rh-Ni/CeO$_2$ Nanowires

Nanowires were synthesized via co-precipitation directly onto E3, which provides the benefits of phage templating in terms of long-range nanostructure such as extremely high surface area, narrow pore size distribution, and high pore volume, but does not necessarily reach the maximum potential of a fully genetically engineered strain. Although it was straightforward to find a sequence which nucleated rhodium metal, this was largely a fortuitous circumstances. In the case of both nickel oxide and ceria, a sequence was never found which was able to nucleate the material (although one may exist).

After several attempts at finding nucleating sequences for nickel oxide and ceria, this was abandoned. It is probable that the improvement from local templating are significantly less than the improvements that would be realized from a pure co-precipitated E3 system, and further work can pursue whether or not the improvement achieved by local ordering outweigh the cost and difficulty of using a more complicated phage system.

7.0.1 Nanoparticle Sample

The first step in synthesizing the composite nanowires it to form the equivalent nanoparticles. This was done using co-precipitation of RhCl$_3$, NiCl$_2$, and CeCl$_3$ using NaOH and H$_2$O$_2$ as pH modifier and oxidizer to form Rh$_2$O$_3$, NiO, and CeO$_2$, the catalytically active phases of each material.

A solution containing 1% RhCl$_3$, 5% NiCl$_2$, and 94% CeCl$_3$ was made. This solution was precipitated by adding NaOH and H$_2$O$_2$ in the same way as was done for CeO$_2$ nanoparticles alone, at a 100x H$_2$O$_2$ concentration. The solution was dried in air, and then heat treated at 200°C.

Nanoparticles of Rh$_2$O$_3$ were formed by themselves using this method as described in Section 4.3.15. Similarly, nanoparticles of NiO were formed by themselves as described in Section 4.3.16.
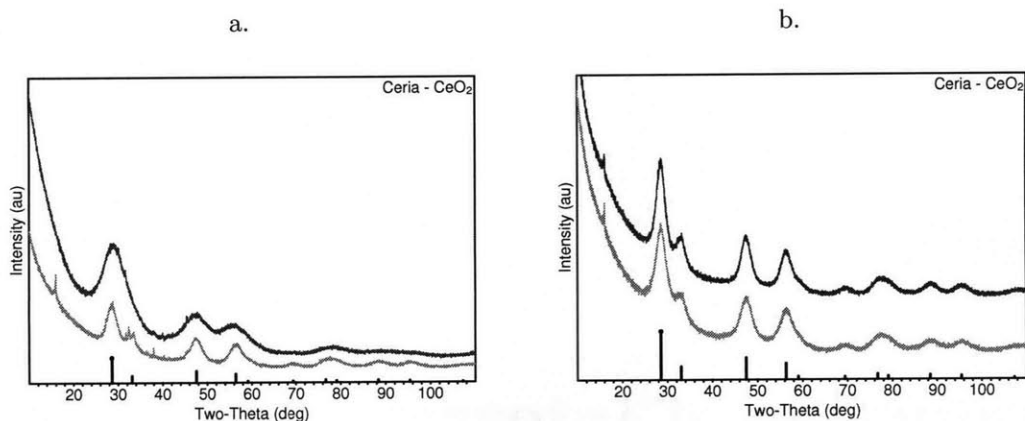
Figure 7-1: XRD data before (top) and after 60 hr heat treatment in air at $400°C$ (bottom) for (a) M13 templated 1%Rh-5%Ni@CeO$_2$ and (b) non-templated 1%Rh-5%Ni@CeO$_2$, showing that in the templated sample, no impurity phases are seen before or after heat treatment.

It is therefore assumed that although no peaks for NiO or Rh$_2$O$_3$ show up in XRD as shown in Fig. 7-1b, these are the phases that are present in the co-precipitated system. However, it is possible that the Ni, Ce, and Rh ions are forming more complicated compounds on the CeO$_2$ primary matrix.

To verify that the ratio of the final particles is roughly the same as the ratio of the precursor mixture, TEM was done on a final dried nanoparticle sample made with 5% RhCl$_3$ and 95% CeCl$_3$. Energy dispersive spectroscopy was used for elemental analysis as shown in Fig. 7-2. The results showed 88 at% Ce, 5 at% Rh, and 7 at% Cl, which is approximately in line with the input precursors. It is assumed that the 7 at% Cl is residual NaCl or CeOCl tetragonal phase formed during the precipitation due to the presence of chlorine ions. It is unclear if the presence of the chloride will degrade the catalyst performance; however, Kugai used RhCl$_3$ as a precursor and had active catalyst.

The nanoparticle powder has an average crystallite diameter of about 3.0 nm as measured by XRD, and a BET surface area of 152 m^2/gm, with a volume of 0.113 cm^3/gm contained in pores. The pore size distribution of the nanoparticle powder is shown in Fig. 7-3.

7.0.2 Nanowires formed via Co-Precipitation on E3

Nanowires were then formed via simple co-precipitation by using a solution with 1% RhCl$_3$, 5% NiCl$_2$, and 94% CeCl$_3$. E3 phage was added to get to an equivalent concentration of 10^{11} phage particles per mL with 100 mM total concentration of metal salt precursors. Again, it is assumed that because the synthesis successfully formed Rh$_2$O$_3$ in Sections. 4.3.15 and 4.3.16 that it will form them successfully in this system as well. It is also assumed that the particles will, at a minimum, experience heterogeneous nucleation on the sites formed by the CeO$_2$ nanowires being formed in solution. In an ideal situation, the Rh$_2$O$_3$ and NiO would also be templated into wires on the E3 phage, but this was not tested.
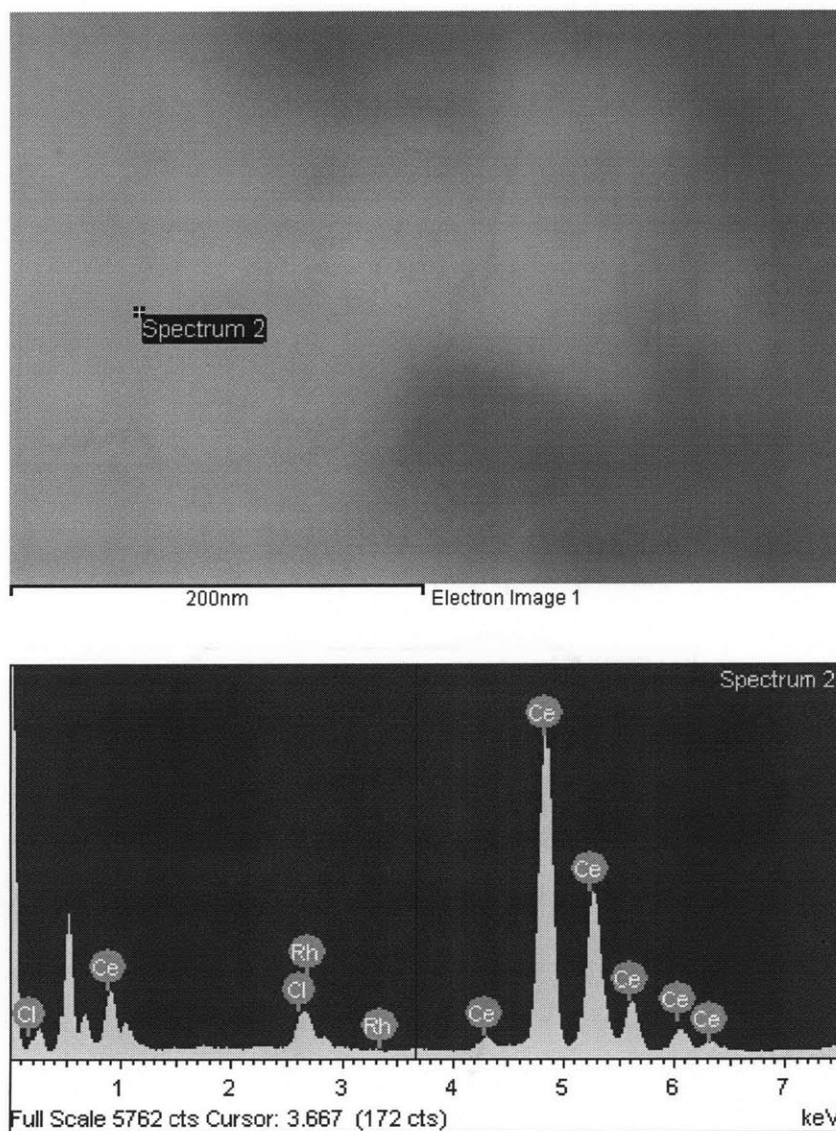
Figure 7-2: A dark field image and EDS elemental X-ray spectra taken with a TEM probe at the point shown. The composition at the selected point is roughly 5% Rh, 88% Ce, and 7% Cl (excluding oxygen because EDS analysis of oxygen is non-quantitative).
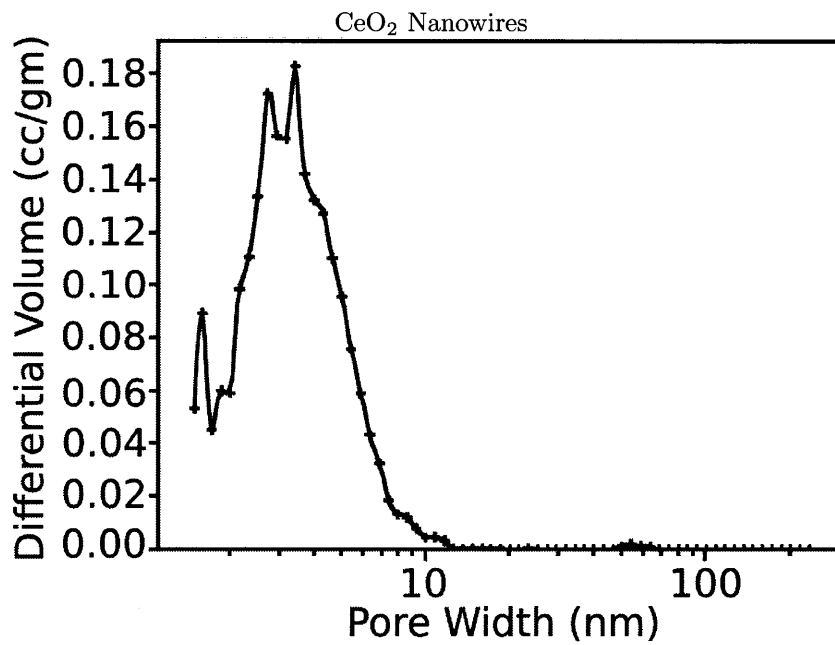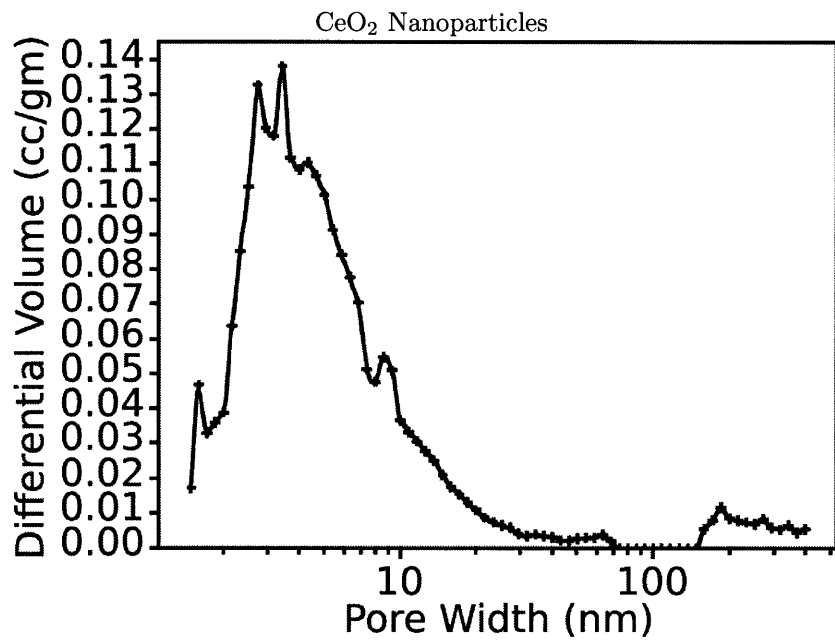
Figure 7-3: Pore size distribution of CeO$_2$ nanoparticles and CeO$_2$ nanowires calculated using a DFT model. The nanoparticles have less total area contained in pores, and the nanowires also have a more narrow pore size distribution.

The resulting nanowire powder had an average crystallite size of 3.5 nm, and a BET surface area of 180 m^2/gm with a pore volume of 0.121 cm^3/gm. The pore size distribution for the nanowires formed via co-precipitation on E3 is shown in Fig. 7-3.

The powder was heat treated at 400°C for 60 hours to look at it's thermal stability. Unlike the nanoparticle sample, the nanowires showed no noticeable precipitation of minor phases over the length of the heat treatment as shown in Fig. 7-1a. This is very encouraging because it suggests good integration of rhodium and nickel into the nanowire structure, as opposed to discrete clusters of rhodium and nickel separate from the nanowires.

In both cases, it is assumed initially that Rh_2O_3 and NiO are active catalytic species based on the reports by Kugai in which he successfully performed oxidative steam reforming by using Rh_2O_3 and NiO nanoparticles on a CeO_2 foam.

7.0.3 Dispersion

To investigate the nanoscale elemental distribution using TEM, catalyst samples were heat treated at 400°C for 2 hr to remove any residual carbon and fully calcine the materials. Samples were re-suspended in ethanol and deposited onto a TEM grid to examine the dispersion of rhodium and nickel into the ceria structure. In the case of both nanoparticles (7-4) and nanowires (7-5), the materials formed via this route appear to be well dispersed, and of approximately the elemental ratios predicted by the precursor fractions.
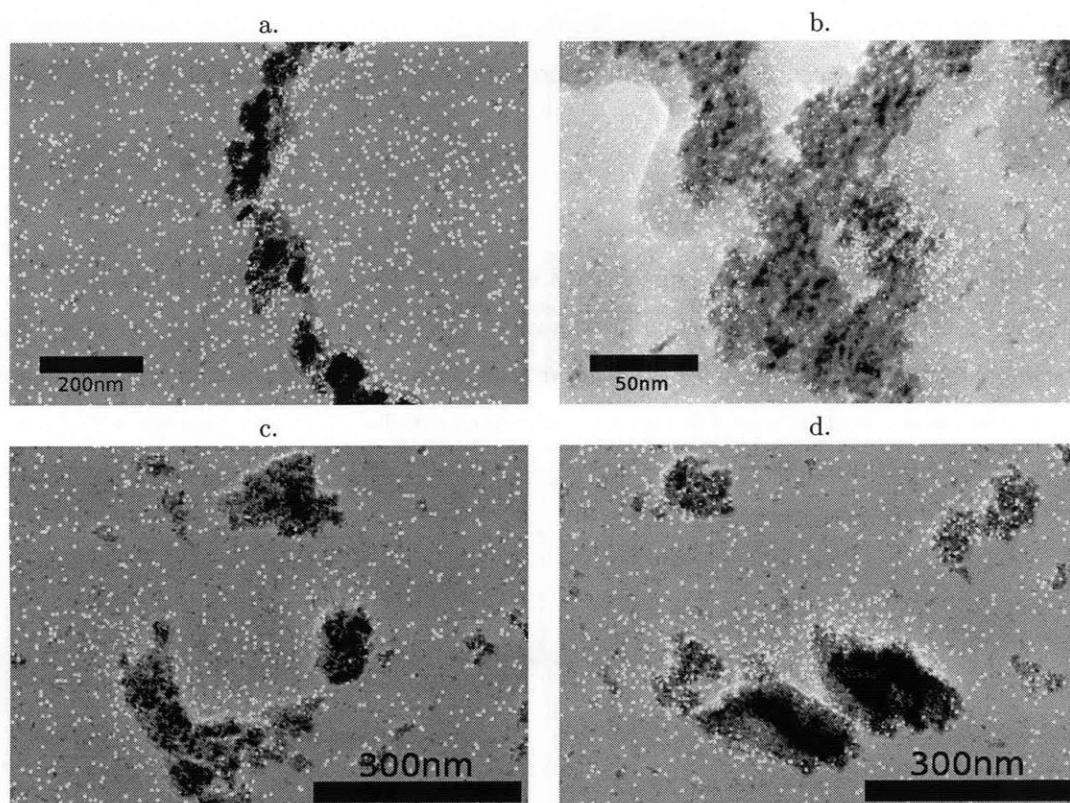
Figure 7-4: TEM micrographs showing the elemental distribution in untemplated catalyst after heat treatment in air and re-dispersion in ethanol. (a) 120k (b) 500k (c) 200k (d) 200k magnification. In each case the overall molar ratio was approximately the same as the molar ratio of the precursors. Blue is rhodium, green is nickel, and red is cerium. (Images taken by Dr. Dong Soo Yun)
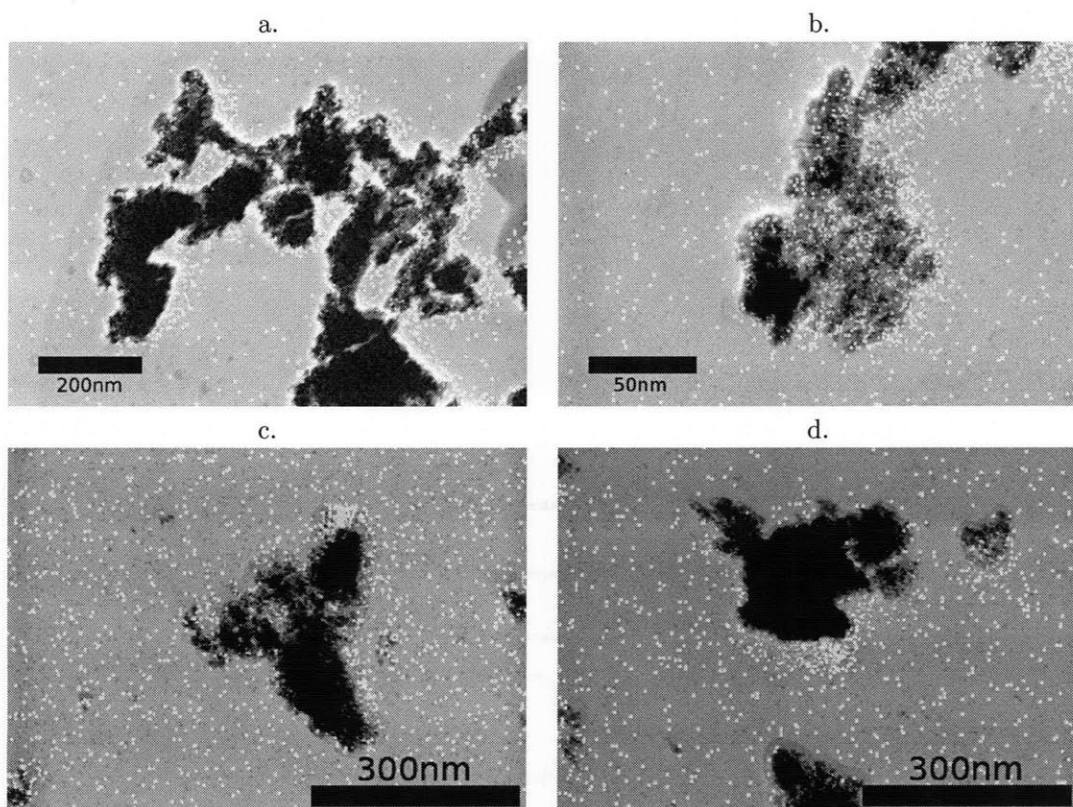
Figure 7-5: TEM micrographs showing the elemental distribution in M13 templated catalyst after heat treatment in airand re-dispersion in ethanol. (a) 120k (b) 500k (c) 200k (d) 200k magnification. In each case the overall molar ratio was approximately the same as the molar ratio of the precursors. Blue is rhodium, green is nickel, and red is cerium. (Images taken by Dr. Dong Soo Yun)

Chapter 8

Catalytic Results

The nanowires and nanoparticles produced using the knowledge from the previous chapters were tested for catalytic activity against ethanol in the formation of hydrogen. This chapter is split into two sections, one for the FTIR Based system which was used first (Section 8.2), and one for the Gas Chromatography (GC) Based system which superceded it (Section 8.3).

8.1   Overview of Reactor Differences

The largest drawback to using FTIR to make measurements here is using multiple sensors for the same gas stream, which allows for the possibility of changes in composition due to water condensation, or simply miscalibrations to result in large differences between the instruments. Further, the hydrogen sensor broke repeatedly and seemed to be sensitive to some other compound in the stream, making the data even more suspect. Although significant steps were taken to try to work around these issues, it was ultimately impossible to validate the results sufficiently to trust the data.

Further, the FTIR system had several key design flaws in the overall reactor topology. First, the input stream had both a water and an ethanol flow controller with the idea of being able to vary the input ratio easily. However, at low flow rates, this resulted in drops of ethanol and drops of water hitting the boiler at different times, resulting in wild fluctuations in the input ratio to the reactor. This was addressed in the GC-based reactor by using a premixed solution of ethanol and water which was injected using a fuel injector directly into the reactor. Direct injection aerosolized the liquid, enabling more even evaporation, allowed for a better "steay-state" operating condition, and the reduced tubing path before the reactor bed limits the effect of homogeneous and tubing-catalyzed reactions.

Next, the stainless steel tubing was difficult to regulate the temperature of due to poor conductivity. In the GC system, this is dealt with by holding the majority of the reactor inside the furnace and eliminating most external tubing. The remaining length of stainless steel tubing between the

furnace and the GC was clad in copper tubing to act as a heat spreader, which reliably kept the temperature above boiling without superheating anywhere. Further, the tubing was brought with copper cladding intact inside of the heated sample box of the GC, meaning that at no point the tubing is exposed to an ambient temperature that would allow condensation. The GC reactor also has stainless steel filter elements installed at multiple locations to prevent particulates from clogging the tubing or valve box to cause pressure spikes (which were seen regularly on the FTIR system). Further, the GC system has a 150 mL residence volume post-reactor to integrate out high-frequency oscillations in the output composition. The GC system was also generally allowed to equilibrate over 35 minutes per measurement, resulting in more stable and repeatable measurements.

Last, the GC system is able to measure all components simultaneously and with high sensitivity, making it easy to ensure that there were no "hidden" products in the complicated FTIR spectra. The measurement of inert N_2 gas in the system also allowed the straightforward calculation of the input ethanol concentration based on the amount of nitrogen in the output stream and the initial ratio of the two. This allows for the fairly direct calculation of the conversion percentage of ethanol in the stream.

The results from using the GC are significantly better than the results from using the FTIR in several key ways, and the FTIR results and analysis should be taken purely for educational value — the results themselves are unreliable. However, the GC results were steady for long periods of time, were readily repeatable, and there were no signs of systematic problems with the reactor design in that system.

8.2   FTIR Based Reactor

The overall design of the test reactor is shown in Fig. 8-1. Part descriptions are as follows:

1. Compressed Air Inlet from Air Tank. An air compressor proved to not provide a steady enough inlet pressure to give good control over the flow rates through the flow controllers.

2. Liquid water in a double ended sample cylinder with back pressure provided by air. Swagelok Part# 316L-HDF4-500. 500mL volume.

3. Liquid ethanol in a double ended sample cylinder with back pressure provided by air. Swagelok Part# 316L-HDF4-500. 500mL volume.

4. Alicat LC-5CCM-D/5V, RIN mass flow controller with a range from 0-5 mL/min of liquid. Compatible with Water, and has an RS232 interface.

5. Fluid Solutions L13V02-AGD-11-K mass flow controller with a range from 0-1 mL/min of liquid. Compatible with Ethanol and constructed of 316 stainless steel. Has an RS232 interface.

6. Alicat MC-1SLPM-D/5M, RIN, GAS gas mass flow controller with a range of 0-1 SLPM of Air and an RS232 interface.

7. Heated Manifold, constructed from 316 stainless steel. Temperature is measured with a in-line type K thermocouple and controlled using an Omega temperature controller with a setpoint above 150°C. Heating the manifold is accomplished with heat rope powered from AC voltage.

8. Tube Furnace with catalyst fixed bed reactor inside. Tube furnace is model HTF55122A, is vertically mountable, and is controllable with RS232. The fixed bed reactor is made from an in-line particular filter using a 0.5μm mesh 316 stainless steel filter. The filter is filled with sand up to the level of the top of the filter, and then the catalyst powder is placed on top.

9. All tubing is 316 stainless steel, in most places wrapped with heat rope and layers of insulation to prevent any condensation of water inside the tubing. The temperature of each tubing run is controlled with an in-line type K thermocouple at the output and an Omega temperature controller.

10. Jasco FTIR-4100 with a heated stainless steel gas cell using ZnSe windows. The input gas comes in through a compression fitting directly to the stainless steel tubing from the reactor, flows through the cell with an internal volume of 38.5 mL. At a flow rate of 100 mL/min, this should allow the FTIR to come roughly into equilibrium with the reactor output within approximately 10 time constants due to the mixing allowed in the FTIR gas cell, giving roughly four minutes as the lag time between the reactor and the FTIR measurement.

11. Set of dual miniature solenoid valves to allow sampling of the output stream after passing through the FTIR. The set allows electronic switching between exposing the hydrogen sensor to the sample gas and a 5% H_2 in N_2 forming gas to prevent carbon monoxide or oxygen buildup from causing an offset in the hydrogen measurement.

12. H2Scan Hydrogen Sensor capable of measuring 0-100% by volume hydrogen in a gas stream. Measurement can be read either digitally, or via an analog output current. Sensor cannot be exposed to CO or O_2 for long periods without developing an offset. The offset can be reversed by exposing the sensor to hydrogen gas overnight.

After collecting all of the parts, the system was assembled inside of a fume hood as shown in Fig. 8-2. All sensors and control systems were attached to a computer and LabView was used to control and automate taking measurements on the catalyst at a variety of different operating conditions.
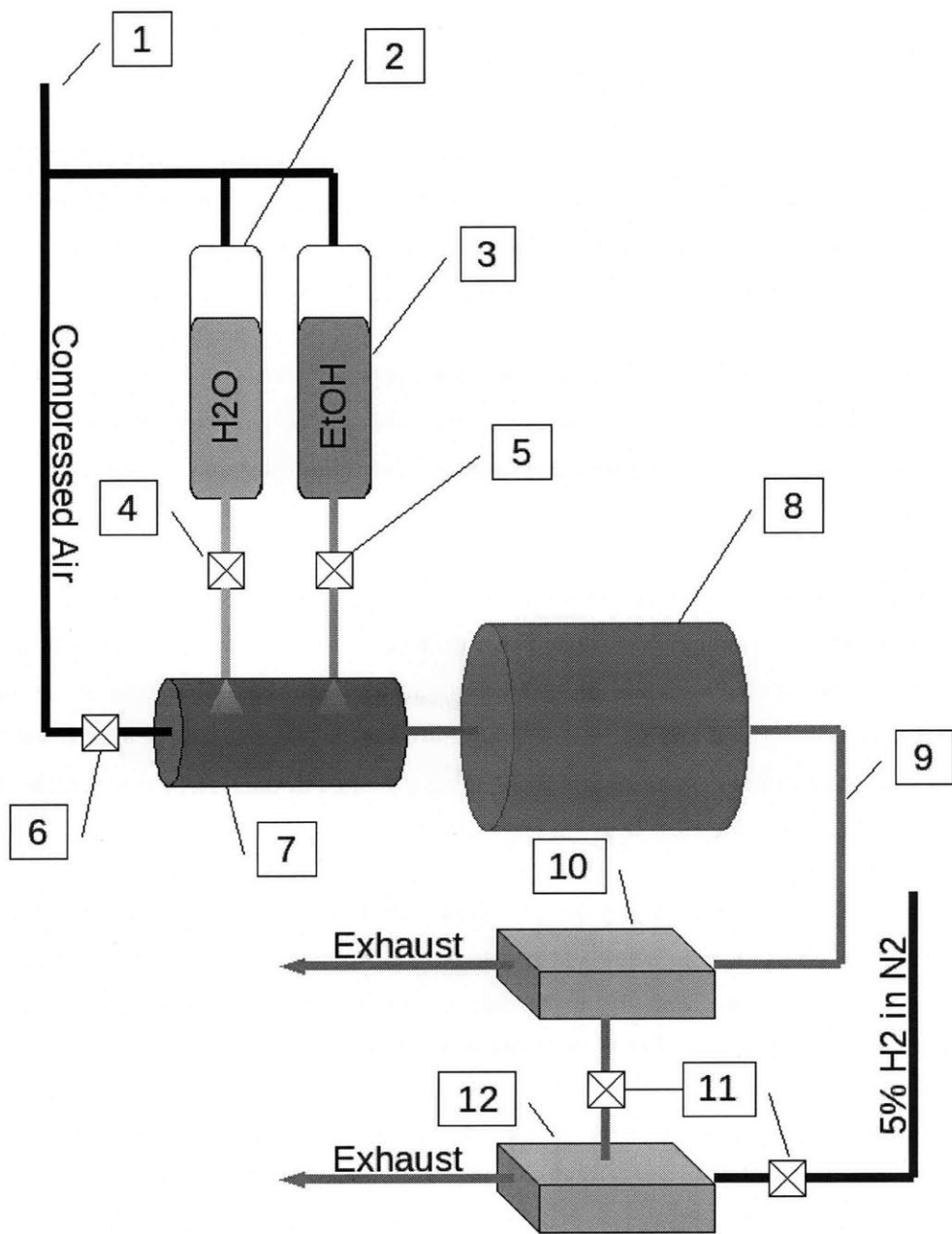
Figure 8-1: A schematic overview of the test reactor. Part descriptions are given in the main text.
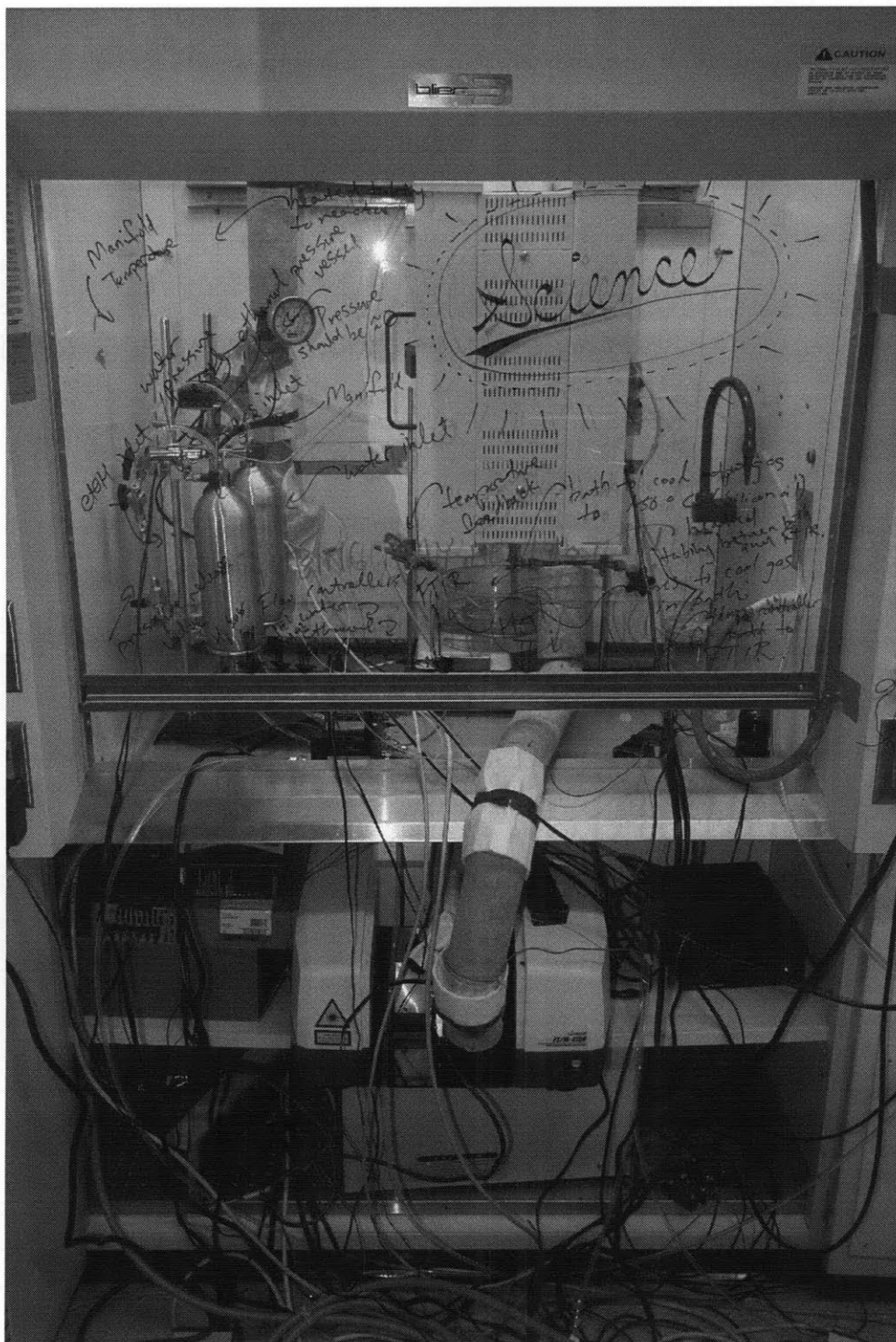
Figure 8-2: A photo of the test reactor. FTIR and Hydrogen Sensor are in the vented cabinet underneath while the flow controllers, manifold, and reactor are above in the fume hood.

8.2.1 FTIR Catalytic Tests

The reactor was used to measure the composition of the output gas resulting from the use of various catalysts as a function of flow rate, etOH:H_2O:O_2 ratio, temperature, and material.

8.2.2 FTIR Catalyst Heating

The catalyst powders were heated from the outside by use of a tube furnace. The powders were held on a 0.5 μm stainless steel filter inside of a 316 stainless steel cylinder. The cylinder is roughly 3/4" in diameter, 1.5" in height, and 1/16" in wall thickness. At the flow rates used in this experiment, ethanol was typically flowing at roughly 1.4 mmol/min. With a heat of combustion of 1300 kJ/mol, this is equivalent to a maximum power output of 30.3 W in the case of all ethanol being completely combusted on the catalyst. The value of 30.3 W represents a maximum "unexpected" heating power input to the catalyst powder.

The 316 stainless steel filter has a thermal conductivity of roughly 20 $Wm^{-1}{}^{\circ}K^{-1}$, which corresponds to a temperature difference of approximately 1 °K to transmit 30 W through the wall of the reactor vessel. The air outside of the reactor vessel was kept at a well-regulated temperature through use of a thermocouple and feedback to the furnace controller, so although the maximum average temperature inside the reactor vessel might be slightly above the desired setpoint, the error is negligible at the temperatures being investigated (300-400 °C).

Although we can say with certainty that the average temperature inside the bed should not significantly exceed the setpoint temperature dictated by the temperature of the air outside of the reactor vessel, it is not clear if local hot spots in the catalyst powder may be forming. It is possible that the reaction could heat up local areas of the catalyst significantly higher than the expected temperature, and remain high due to the poor thermal conductivity in the catalyst powder.

8.2.3 FTIR Calibration

Calibration of the FTIR was done by using pure samples of each anticipated component of the gas stream. Calibration gas standards were purchased from Airgas for CO_2 (19.99%), CH_4 (20.36%), and CO (9.83%). The remaining identified peaks in FTIR seem to belong to etOH, H_2O, and formaldehyde (CH_3COH). For each of the remaining peaks, calibration was done by using the existing flow controllers to inject a 5 mol% mixture of the desired liquid with air in the manifold with no catalyst present in the reactor.

The resulting calibration standards are shown in Fig. 8-3. The standard for water is considered to be non-quantitative due to the atmosphere in the FTIR being open outside of the gas cell. This was necessary in order to allow tubing from the reactor to enter the FTIR measurement chamber. As such, water is taken as a calibration standard only in the sense that it is used to remove water

peaks from the data during fitting — the actual values fitted are not used in the analysis.

8.2.4 FTIR Orthogonal Area Fitting

Each FTIR measurement was independently analyzed using a custom data algorithm written in Matlab. Initially, a simple least squares regression was attempted, but due to clipping of the signal at large adsorbances, DC offset due to the FTIR windows collecting particulates, and peak broadening as the intensity increased, this simple fit failed to provide a good fit to the data.

It is known that the area under a peak in FTIR is related to the concentration of the component; however, the peak shape changes as concentration changes in small ways, and small amounts of DC noise can dramatically influence a least squares regression fit. To take advantage of this, the area of isolated peaks referenced to their baseline is measured in order to get a good value for the amount of a single component in the system.

After finding the concentration of a single component, that component can be approximately removed from the original dataset by scaling linearly and subtracting, producing a dataset of all the remaining components — effectively removing that factor from the data fitting. This technique has been named orthogonal areas matching, as it uses area matching to determine the magnitude of each orthogonal component, but then uses linear combinations to remove the signal from the rest of the dataset, allowing area matching to be performed on otherwise obscured peaks.

In this case, the CO peak between 2101 and 2097 nm is nicely isolated, and is first used for area matching. After this match is completed, the water peaks between 3952 and 3796 are isolated. Next, the CH_4 is removed using the peak between 2921 and 2912. After removing the CH_4, there is still an artifact from clipping at the very sharp peak at between 3001 and 3026 — this is removed by replacing that segment of the remaining dataset with a linear interpolation between the endpoints, and this is repeated for the CH_4 peak between 1297 and 1309. Next, CO_2 is removed by using the now isolated secondary peaks between 3767 and 3501 instead of the primary peak which is unusable due to clipping in the calibration standard. The artifact from the CO_2 primary peak is then removed by setting the remaining spectra to zero in the range of 2260 to 2399.

Finally, this leaves only CH_3COH and etOH remaining in the spectra. Unfortunately, these two components have broad, overlapping peaks that are impossible to isolate and do area matching with; however, now that there are only two components and all of the railing signals have been removed, the final two components can be calculated by using a least squares regression. The data fit using this algorithm is shown in Fig. 8-4. The modeled data built up from linear combinations of the calibration standards is displayed on top of the actual data, and it can be seen that even fine features are fit quite well.
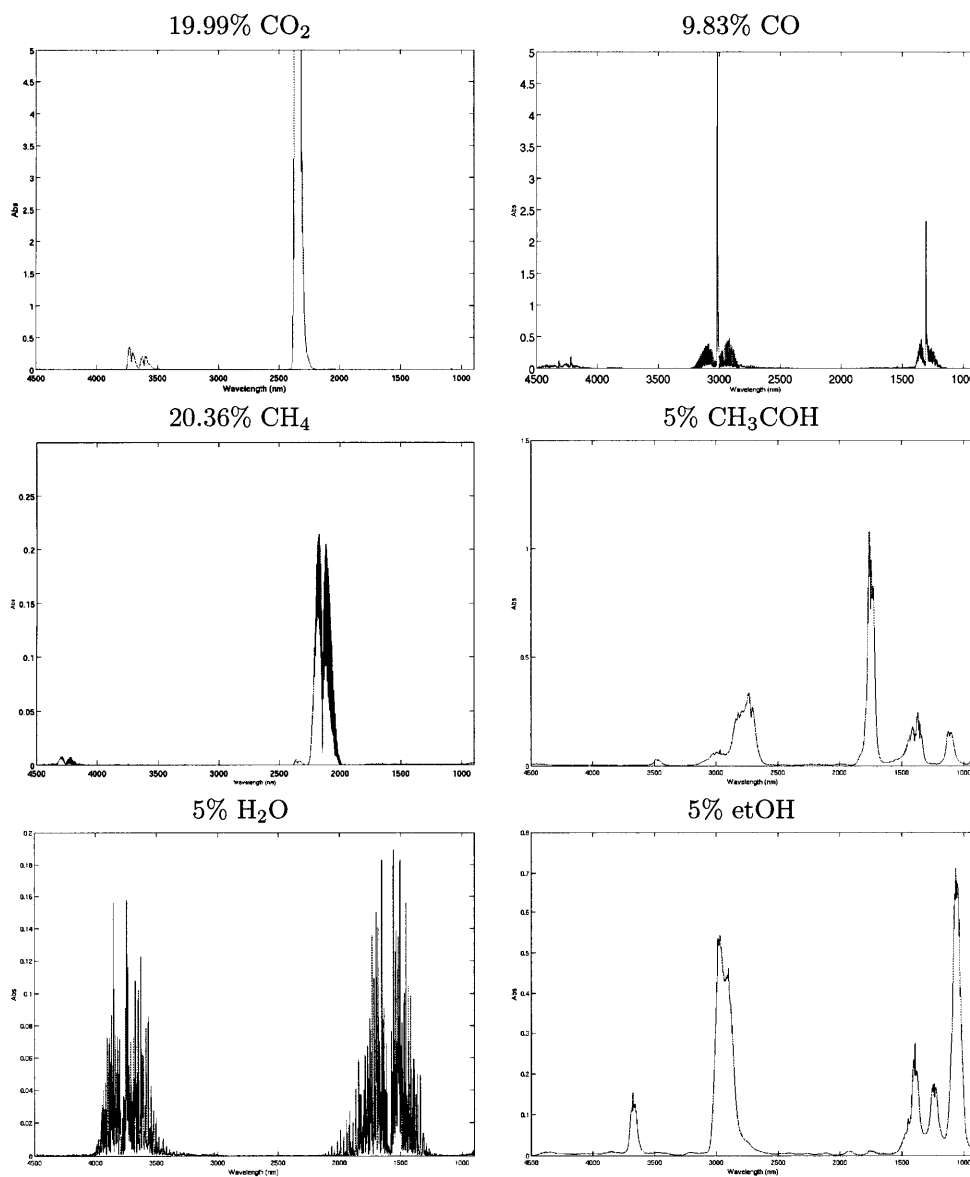
Figure 8-3: Calibration standards for FTIR made either from a calibration standard, or by mixing to a 5% molar fraction in nitrogen background using the reactor's heated manifold.
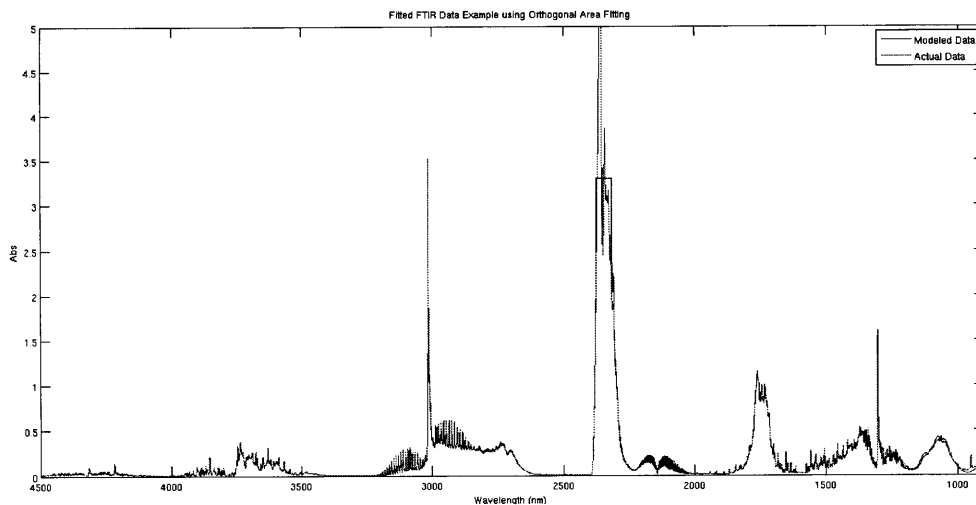
Figure 8-4: Example showing Orthogonal Area Fitting algorithm. The calibration standard was clipped in the area of 2300 nm for CO_2, but the peak was able to be fit anyway by removing water and methane peaks in the 3500-3800 nm range and using the smaller CO_2 peaks in that range instead. Note that even small details like the methane side bands are fit very closely.

8.2.5 FTIR Catalytic Results

The concentrations of CO_2, CH_4, CO, CH_3COH, H_2O, and ethanol were measured using FTIR, while the concentration of hydrogen was measured using a separate sensor.

Kugai *et al.* used a ratio of 4:1 H_2O:etOH and a ratio of 0.4:1 O_2:etOH. We used air instead of oxygen, so this is altered to 1.9:1 Air:etOH to acheive the same ratio of reactants. This makes the most natural place to start tests.

Experiments were run by taking a background measurement on the FTIR while under a flow of only air at 3.000 mmol/min with no ethanol or water being injected into the manifold at each temperature, and then adding in ethanol and water to bring the total flow rate up to 10.882 mmol/min (including nitrogen in the air). The flow was composed of 3.000 mmol/min of air, 6.306 mmol/min of water, and 1.576 mmol/min of ethanol. Assuming an ideal gas, the vapor at room temperature would be flowing at 244 mL/min, which is roughly the flow rate used by Kugai of 216 mL/min over 500 mg of catalyst.

After the background measurement was taken, the Jasco software was used to take one sample per minute for 31 samples. The resulting 31 datasets were each independently analyzed using orthogonal area matching, and the results were recorded. The concentration of hydrogen measured by the sensor was also recorded. This data was used to calculate the overall conversion efficiency by comparing the amount of carbon in products to the amount of carbon in ethanol present in the output stream. Carbon was used as a tracking element because hydrogen is being added or removed from the stream as water, which is not measured quantitatively in our reactor. Finally, CO_2, CH_4, CO, CH_3COH,

137

and H_2 concentrations are calculated and normalized so that they sum to 100% to account for the fluctuations in water concentration.

In the case of co-precipitated nanoparticles and nanowires, the initial results as a function of temperature showed a clear difference between the nanoparticles and nanowires formed at a total flow rate of 10.882 mmol/min. Fig. 8-5 shows the results for 500 mg of powder. This gives a total volume hourly space velocity of approximately 30000 hr^{-1} assuming a catalyst density of 1 gm/mL and taking the reactant volume as the volume as it would be at room temperature. However, because we are taking measurements over the catalyst at different temperatures where the reactant volume will be different from that at room temperature, we instead use the mass-based GHSV of 32.7 hr^{-1} with 272.6 mg/min of total gas flow including ethanol, water, oxygen, and nitrogen over 500 mg of catalyst. In general, a GHSV of between 20 and 50 should be similar to the flow rate used by Kugai, depending on the temperature at which he took his volume measurements.

8.2.6 FTIR Deactivation and Regeneration Tests

Using the FTIR and Hydrogen Sensor, the deactivation properties of the catalysts were tested. First, the deactivation was shown to occur mostly within the first hour of testing, and almost entirely within the first two hours of testing, as shown in Fig 8-6. After two hours, the conversion percentage remained fairly constant for the remaining 10 hours over which the experiment was run.

This result suggests that by running the catalyst on stream for about an hour, we should be able to get a reasonable picture of the long-term activity of the catalyst.

The second important feature to understand before carrying out catalytic tests is the regeneration capacity of the catalyst. In this case, it is clear that something is deactivating the catalyst fairly quickly, so it is especially important to know if the deactivation is a result of permanent microstructural changes in the catalyst, or due to some other effect such as coking or an undesirable change in oxidation state of the catalyst.

To test this, the reactor was run for an hour at various ratios of water:ethanol:air, and then run for an hour with only air. After each run, it is clear that the overall activity of the catalyst is mostly regenerated, and that it then deactivates again after some time on stream as shown in Fig 8-7.

This form of deactivation is likely not due to permanent microstructural changes due to the ready capacity for regeneration. Instead, the deactivation is being caused by either a buildup of coke which is blocking catalytic sites, or by a change in the oxidation state of the catalyst. It is more likely to be a buildup of coke because while the conversion percent decreases, the product distribution remains relatively unchanged over time; however, regardless of the source of the deactivation, operating the reactor in a "pulsed" mode where it is alternated between an air stream and a fuel stream will keep it running optimally.

138
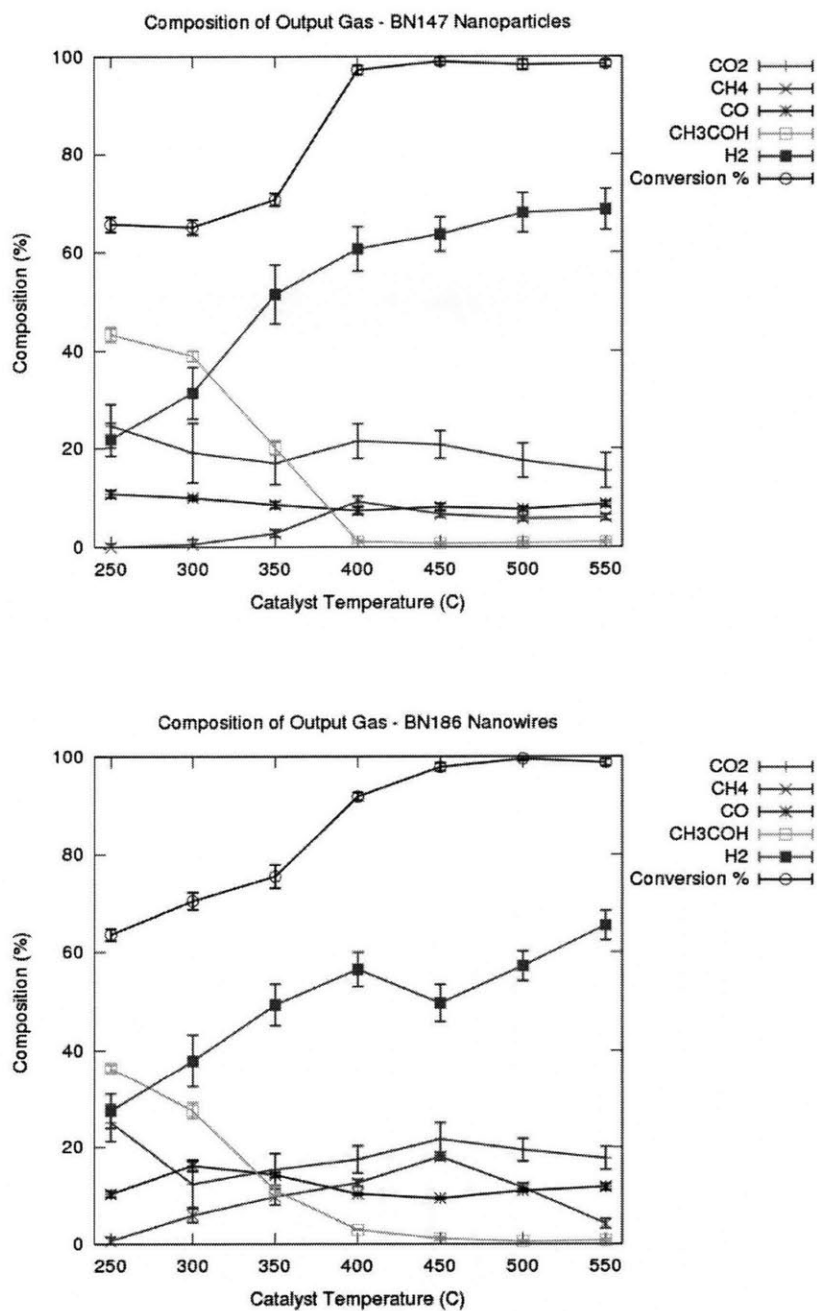
Figure 8-5: Gas output composition as a function of temperature for co-precipitated nanoparticles and nanowires templated on E3. Total flow rate is 10.882 mmol/min, and the amount of catalyst in both cases was 500 mg ($\sim$ 2.905 mmol assuming CeO_2), for a GHSV of 32.7 hr^{-1}. Values measured using FTIR/H2 Sensor
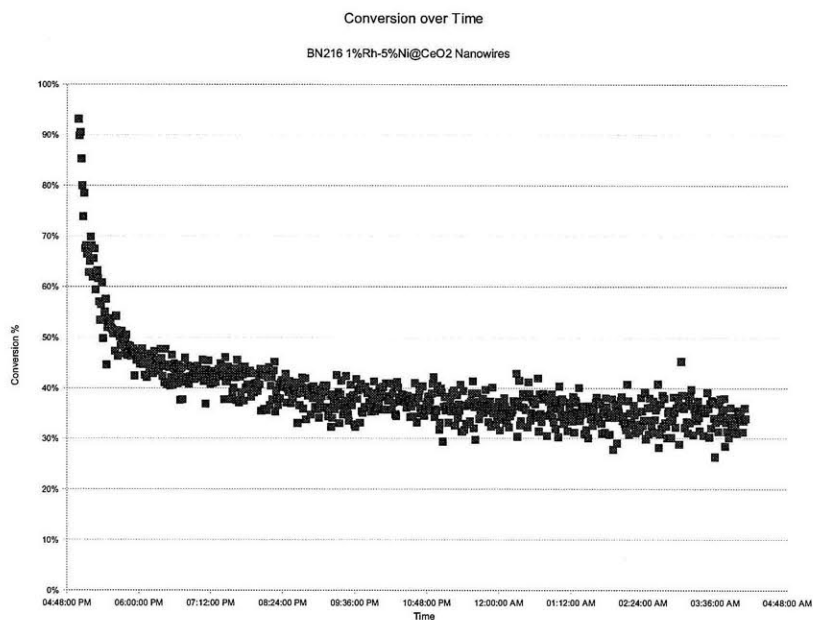
Figure 8-6: Although immediately after starting the reactor, the conversion is very high, the final conversion percent drops rapidly within the first two hours of operation at 300°C before settling at around 40% for long times. Measured using FTIR.
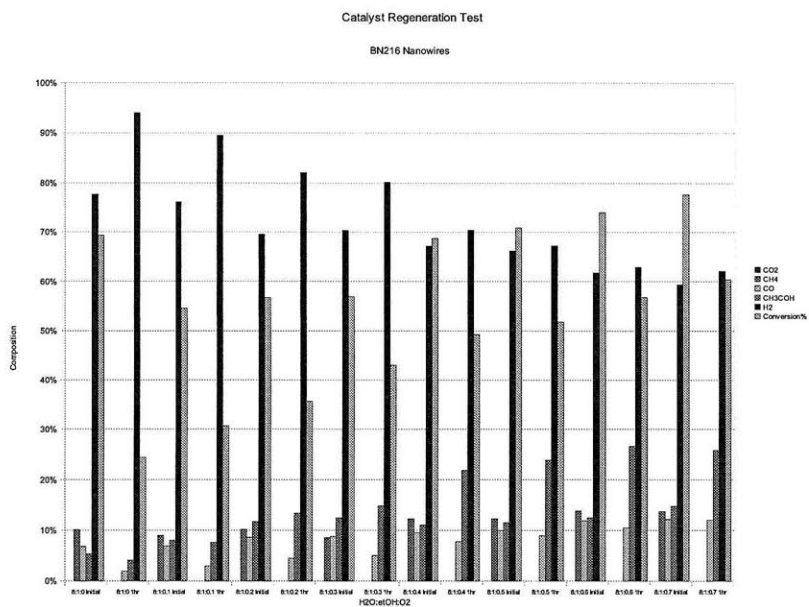
Figure 8-7: The activity and product distribution of the same catalyst sample with an hour of treatment by dry air between each new set of conditions. The catalyst shows clear signs of being reactivated and deactivated in cycles as it is put on stream. Measurements began on the far left and moved to the right over the course of the experiment. Measurements taken with FTIR and Hydrogen Sensor

Ethanol:Water Ratio Test

BN216 Nanowires (6m^2/gm)
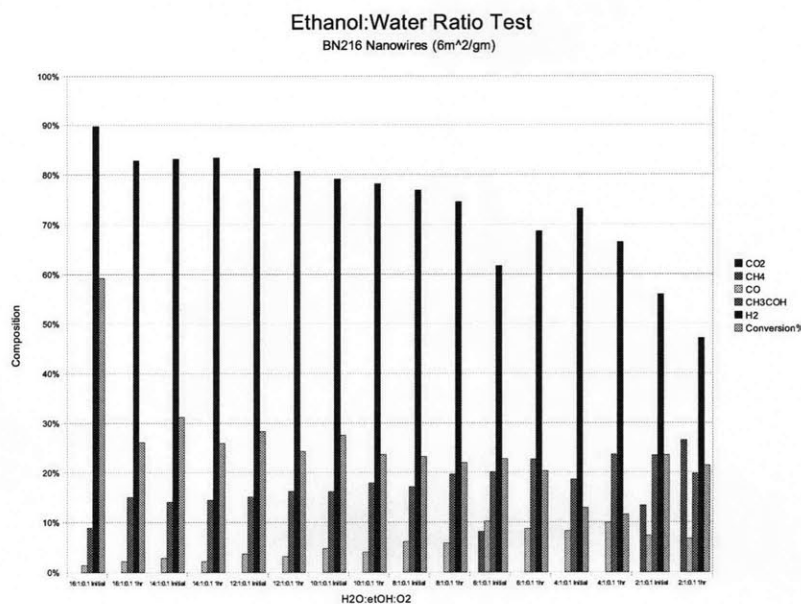
Figure 8-8: The gas composition over BN216 nanowires is shown as a function of the ratio of water to ethanol. At large ratios of water:ethanol (more than 8:1), no methane is visible using FTIR, and the hydrogen selectivity appears to be very good, and very little carbon dioxide or carbon monoxide are produced.

8.2.7   FTIR Reactant Ratio Tests

The results of the regeneration tests shown in Section 8-7 showed an interesting trend that suggests that decreasing the amount of air present while increasing the amount of water relative to ethanol may be beneficial. At high concentrations of water and low concentrations of air, the conversion percent was suppressed, but the hydrogen selectivity was enhanced simultaneously, CO production was surpressed to less than 2% of the output gas composition, and CO_2 was entirely eliminated. However, as is outlined in the next section, the absolute values of these measurements are questionable, although the overall trends are likely real.

This test was carried out again over a wider range of water ratios while keeping a 1:0.1 ratio of ethanol to oxygen. The results are shown in Fig 8-8. Overall, this again supports the result that higher amounts of water suppress carbon monoxide production while favoring the production of hydrogen. Almost no methane was seen in any of the samples at higher water ratios, meaning that more of the hydrogen from ethanol was being released as useful fuel.

8.3   Gas Chromatography Based Reactor

The overall goal of replacing the FTIR with a GC sensor is to allow the simultaneous detection of all products. This replacement was very successful, and the results in this section should be taken
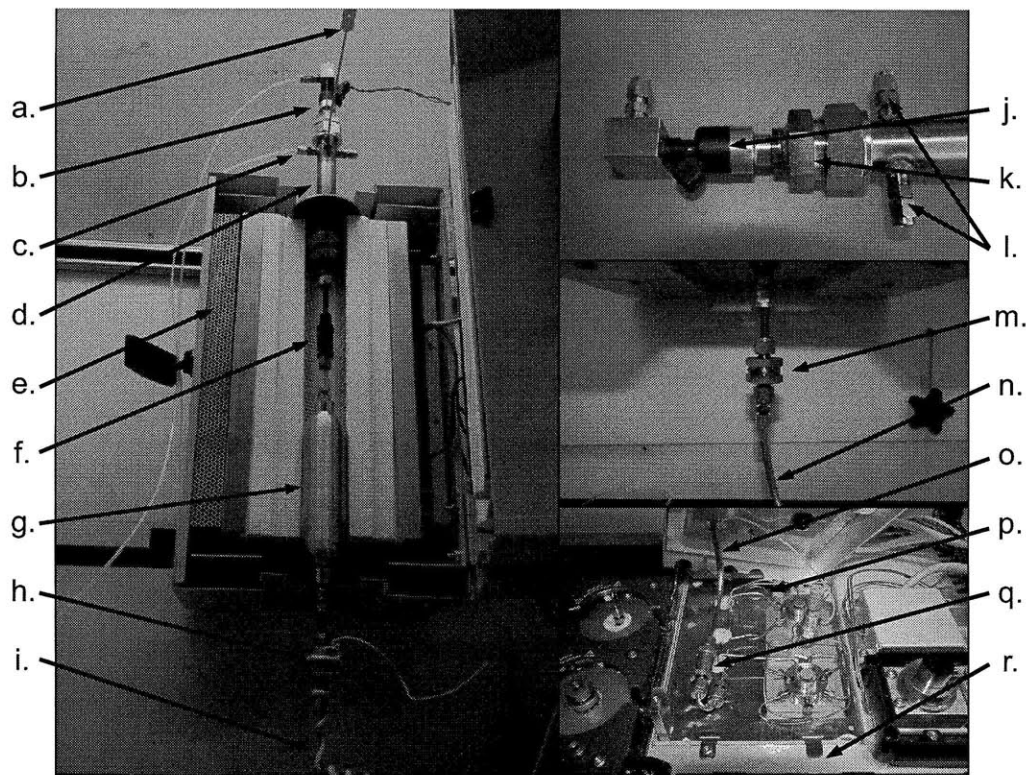
Figure 8-9: Photo of Reactor. (a) Thermocouple to measure input gas temperature. (b) Fuel injector to inject water-ethanol mixure. (c) Inlet for air and for argon. (d) Preheating chamber (subsequently covered with heat tape). (e) Tube furnace. (f) Catalyst chamber. (g) 150 mL integrator. (h) 0.5 μm particulate filter. (i) Copper sheathed 316 stainless steel tubing wrapped in heat rope. (j) Close up of fuel injector. (k) Close up of custom Swagelok Fitting. (l) Gas inlets. (m) Close up of particular filter. (n) Close up of copper sheathed tubing. (o) Entry to GC. (p) GC sample loop. (q) Particulate filter. (r) Agilent 7890A GC.

to be much more reliable than the FTIR results.

8.3.1   Gas Chromatography Based Reactor Design

Catalyst powders were loaded in an unpacked layer in a 316 stainless steel chamber (Swagelok Part SS-4F-05 In-Line Particulate Filter) (8-9(f)) where the filter element was replaced with a 12 mm fine porosity fritted borosilicate disc (ChemGlass Part CG-201-05) to a typical depth of $\sim$5 mm in the case of 1000 mg samples. In the case of very small samples (100 mg), a thin layer was placed on the borosilicate disc by gently tapping the catalyst chamber until the disc was no longer visible. The disc was replaced after each test, and the gas-hourly space velocity (GHSV) was changed by using varying amounts of catalyst powder while keeping the absolute flow rate constant to eliminate variations due to reactor activity or pressure changes due to increased flow rate. The GHSV was estimated by using an assumed catalyst density of 1 gm/mL, and the gas volume was converted to a standard volume at 298°K and 1 atm.

142

The entire catalyst chamber was heated to the desired reaction temperature using a tube furnace (HTF55122A 1-Zone 1200 °C Furnace with CC58114COMA-1 Digital Controller, Thermo Fisher Scientific) (8-9(e)). The preheating chamber was made out of 1" diameter 316 stainless steel tubing with custom machined Swagelok fittings (8-9(d,k)) to allow for the fuel injector (16 lb/hr Disc High-Z Fuel Injector, Racetronix Model 621040) (8-9(b,j)) to inject liquid directly into the preheating chamber. The fuel injector temperature was measured using a thermocouple on the Swagelok fitting, and heated with heat tape (McMASTER-CARR Part 4550T12) wrapped around the preheating chamber outside of the furnace controlled using a temperature controller (Omega CNI3233-C24) to 120°C.

The air mass flow controller in all experiments is set at 14 mL/min (2.94 mL/min O_2), Argon flow controller was set at approximately 100 mL/min, and ethanol was injected with the fuel injector using a 1.157 ms pulse every 2 seconds at 50 PSI and 24 VDC. This pulse length is equivalent to 2.91 uL per pulse based on fuel injector calibrations done by injecting known pulse lengths and counting the number of pulses required to inject 10 mL of liquid. The total molar ratio at STP for these amounts is 1.7:1:10:12 (Air:EtOH:Water:Argon) with a total flow rate of roughly 200 mL/min.

The internal temperature of the preheating chamber was monitored using a temperature probe placed just above the catalyst bed (8-9(a)) with a temperature controller (Omega CNI3233-C24), and the temperature of the input gas was typically close to the temperature of the furnace. The preheating chamber had two 1/8" Swagelok fittings (8-9(c,l)) to allow for argon and air to be added to the mixture using a mass flow controller (Alicat MC-1SLPM-D/5M 0-1 SLPM) for the air, and a manual flow controller for the argon backflow gas.

Below the reactor bed, the gas mixture was allowed to equilibrate in a 150 mL double-ended 316 stainless steel sample cylinder (Swagelok Part 316L-50DF4-150) placed inside the furnace to prevent condensation (8-9(g)). This volume represents a time to equilibration of roughly 7.5 minutes assuming approximately 10 times the replacement time to fully equilibrate at a new composition. The output gas is carried through a 0.5 μm 316 stainless steel filter (Swagelok Part SS-4FWS-05) (8-9(h,m)) to the GC via 1/8" 316 stainless steel tubing sheathed in 1/4" copper tubing wrapped with high temperature heat rope (McMASTER-CARR Part 3641K26) (8-9(i,n)) and using a temperature controller (Omega CNI3233-C24) set to 120°C to prevent condensation. The tubing enters the GC (8-9(o)) through a valve with a 250 μL sample loop (8-9(p)) held at 150°C after passing through another 0.5 μm 316 stainless steel filter (Swagelok Part SS-2F-05) (8-9(q) to prevent clogs in the GC valves. The equilibrated composition is fed continuously through an Agilent 7890A Gas Chromatographer (8-9(r))where the sample loop is switched onto the column every 35 min.

The sample is measured by the GC initially configured to Agilent Configuration 7890-0047, which meets ASTM D3612A specifications, with modified inlet temperature to avoid water condensation (150°C), and lengthened total run time to avoid overlap with any present higher molecular weight

hydrocarbons. This configuration uses an argon background with a flame ionization detector (FID) and a nickel methanizing catalyst for the detection of hydrocarbons, CO_2, and CO, and a thermal conductivity detector (TCD) for the detection of H_2, O_2, N_2, and H_2O.

The results were calibrated using custom mixed gas calibrations provided by Airgas. Hydrogen was calibrated to 6.063% H_2 in argon and 10 samples had a standard deviation of 0.051%. Carbon monoxide was calibrated to 9.568% CO in N_2 and 10 samples had a standard deviation of 0.023%. Methane was calibrated to 20.000% CH_4 in N_2 and 10 samples had a standard deviation of 0.035%. CO_2, O_2, and N_2 were calibrated using dry air. Water was calibrated by using a target 1:1 ratio injected and vaporized in the reactor with air for ten measurements with the total sum of products forced to 100%. This closed to a water amount of 47.85% with a standard deviation of 0.76% over 10 samples. Ethanol and acetaldehyde were calibrated by mixing with water to a known molar ratio and calibrating by liquid injection of the diluted sample and comparison to the water amount measured to avoid any homogeneous decomposition arising from flow through the reactor. Sample amounts are calculated from calibrations by measuring the area of the peaks and comparing to the areas of peaks at the calibration composition.

Bar graphs showing product distribution and activity are made by scaling the product distribution such that the total height is the total ethanol conversion while the internal product distribution is represented by the relative size of each component. Error bars are calculated by using the standard deviation of each scaled component amount over the 36 measurements, scaled proportionally by the amount each component is scaled. For each component, this error is estimated as

$$\sigma_A^{total} = \sqrt{(\sigma_A \cdot F)^2 + (\sigma_F \cdot A)^2} \tag{8.1}$$

where A is the fraction of total products for component A, σ_A is the standard deviation in the fraction of total products for component A over the 36 measurements, F is the total ethanol conversion percent, and σ_F is the standard deviation of the ethanol conversion percent over the 36 measurements.

Homogeneous decomposition was measured by injecting a 1:10 ethanol:water mixture into the reactor with no catalyst present. At 300°C, homogeneous decomposition showed 18.5% conversion of ethanol to acetaldehyde estimated as the ratio of measured acetaldehyde to the sum of the measured acetaldehyde and measured ethanol. Essentially no H_2 or CH_4 was measured. Catalysis is likely taking place in the tubing, which contains nickel, and on the stainless steel filter elements, so by placing the catalyst powder as early as possible in the flow path, subsequent dehydrogenation is limited.

144

8.3.2 Gas Chromatography Catalyst Synthesis

Ni-Rh@CeO$_2$ was formed by using the oxidation and hydrolysis of CeCl$_3$ with RhCl$_3$ and NiCl$_2$ in aqueous solution. 120 mL of water was either used as-is, or by diluting E3 M13 phage (AEEE expressed on the pVIII major coat protein) to a concentration of approximately 10^{12}/mL by adding $\sim$10-100 μL of phage solution at a spectroscopically measured approximate concentration of $\sim$10^{15}/mL. The diluted phage or phage-free water was mixed for 30 minutes in a 500 mL Ehrlenmyer flask at room temperature to ensure good dispersion. For comparison of different phage concentrations, the concentrated phage was decreased in concentration serially by factors of 10 to achieve an internally accurate phage ratio.

After mixing, 30 mL of 1 M metal chloride solution containing RhCl$_3$ (anhydrous, 99.9% Alfa Aesar), NiCl$_2$ (anhydrous, 98% Alfa Aesar), and CeCl$_3$ (heptahydrate, 99% Acros Organics) in a 1:10:89 molar ratio (RhCl$_3$:NiCl$_2$:CeCl$_3$) was added to either diluted M13 phage or phage-free water and allowed to equilibrate over 30 minutes at room temperature at 650 RPM.

After equilibration, nanoparticles were nucleated by the rapid addition of a mixture of 30 mL of 3 M NaOH (99%, Mallinckrodt Chemicals) and 60 μL of 30 wt% H$_2$O$_2$ (29.0-32.0% Reagent ACS, VWR). Immediately after addition, the solution turned dark brown-red and solids formed with gas evolution. The solution was stirred at 650 RPM for 30 minutes to allow the reaction to go to completion. After completion, the suspension was precipitated using centrifugation and the supernatant discarded. The precipitate was redissolved in water to wash residual NaCl and NaOH from the powder, and recentrifuged for a total of three washings. After washing, the precipitate was set out at room temperature in a petri dish in air until dry. After drying, the powders were finely ground and heat treated at 400°C for 2 hours until the final powder was produced.

8.3.3 Gas Chromatography Reactor Results

For catalytic tests, a pre-mixed ethanol/water mixture was injected into a preheater using a fuel injector, where it was mixed with air and argon to keep the total flow rate of gas at $\sim$200 mL/min in a ratio of 1.7:1:10:11 (air:ethanol:water:argon). After preheating to the catalyst temperature, the mixture was passed through a thin layer of catalyst of varying amounts between 100 and 1000 mg. The final output composition was sampled using a gas chromatography column. The results were used to calculate the concentrations of ethanol, water, nitrogen, oxygen, CO$_2$, hydrogen, CH$_4$, acetaldehyde, and CO with samples taken every 35 minutes. No other major products were detected. Overall conversion was calculated as the ratio of ethanol consumed to ethanol injected, estimated using the amount of inert nitrogen detected and the known molar ratio of nitrogen to ethanol at the inlet. Composition is calculated as the fraction of the products each component represents.

After using gas chromatography to take 36 samples over 21 hours at temperatures ranging from
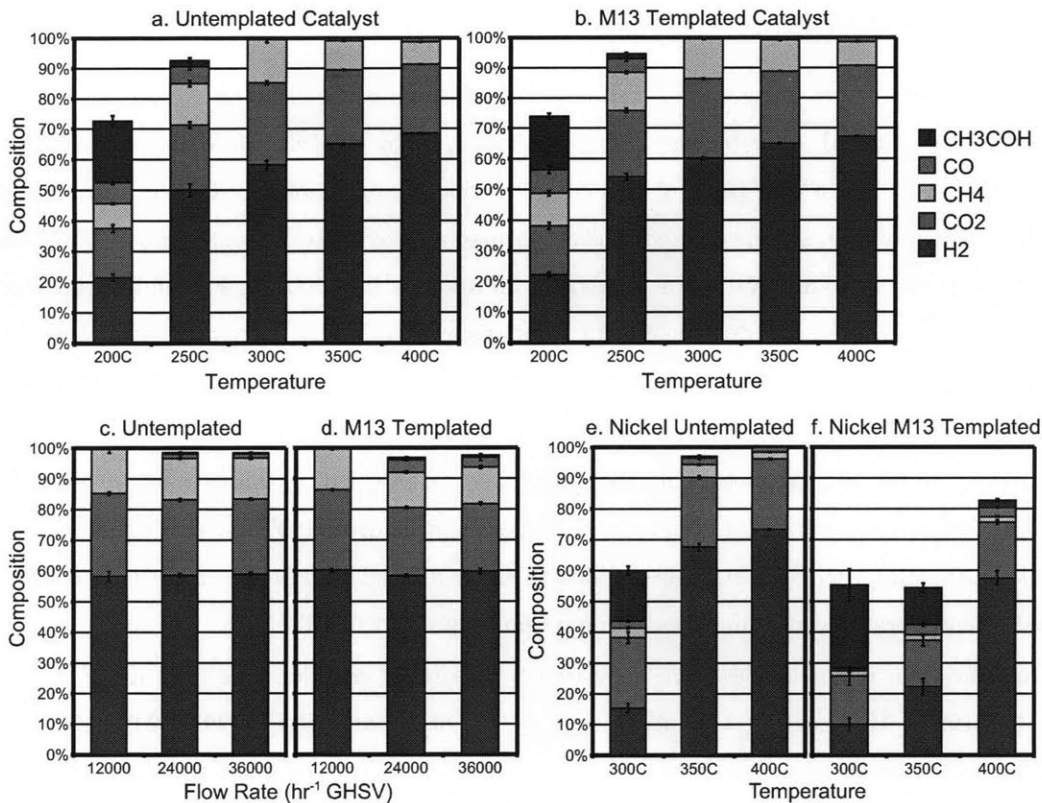
Figure 8-10: Catalytic results at 12000 hr^{-1} GHSV with 1%Rh-10%Ni@CeO$_2$ for temperatures between 200°C and 400°C with (a) no templating, and (b) 10^{12} M13/mL and 0.16 M metal chloride precursor. Catalytic results for varying flow rates between 12000 and 36000 hr^{-1} GHSV for (c) untemplated and (d) M13 templated 1%Rh-10%Ni@CeO$_2$ catalyst. 12000 hr^{-1} GHSV with (e) untemplated and (f) M13 templated 10%Ni@CeO$_2$ catalyst.

200°C-400°C for both nanoparticles and nanowires with 1000 mg of catalyst ($\sim$12000 hr^{-1} GHSV), it is seen that for both nanoparticles and for nanowires, complete conversion occurs at 300°C with approximately 60% H$_2$, less than 0.5% CO, and no acetaldehyde as shown in 8-10(a-b). The best results in literature under similar conditions used Rh-Ni@CeO$_2$ and Co@CeO$_2$ catalysts with 90+% conversion, but with 8-10% CO and 2-7% acetaldehyde, making the new catalysts preferable for use in fuel cells, where CO can act as a poison. [2, 12–26] The untemplated and M13-templated catalyst showed similar product distributions under these conditions.

Increasing the flow rate from 12000 hr^{-1} to 36000 hr^{-1} at 300°C resulted in some decrease in activity, but conversion remained above 95% and both catalysts show similar product distributions. Samples without rhodium were also tested with and without M13-templating, as shown in 8-10(c-d). Without the presence of rhodium, the M13-templated catalyst shows significantly degraded performance relative to the untemplated catalyst, suggesting that nickel may be less active due to the presence of M13.

Nanoparticle and nanowire catalysts were also tested at higher temperatures and flow rates to

146

investigate the long-term thermal stability. At 450°C, 100 mg of catalyst was tested ($\sim$120000 hr^{-1} GHSV), and nanowires showed steady performance over 52 hr with 70% H_2 and about 5% CH_4, 3% CO, and 1% acetaldehyde. At similar flow rates and temperatures, Rh-Ni@CeO_2 catalysts reported in literature showed 50% H_2 with 19% CH_4 while Co@CeO_2 catalysts showed 70% H_2 but with 9% CO and 2% acetaldehyde. [2,12–26]

Nanowires under these conditions showed better thermal stability than nanoparticles of identical composition through a combination of resistance to carbon buildup on rhodium and less nanocrystallite growth. While nanowires demonstrated steady output over a 52 hr measurement, nanoparticles showed decreased conversion over time as shown in 8-11(a-c). The decreased conversion is partially recovered by exposing the catalyst to air for a short time, indicating a surface deactivation most likely caused by carbon buildup. [72] However, a second 52 hr measurement of the reactivated nanoparticle catalyst shows more rapid deactivation, indicating that the degradation of the catalyst is also caused by long-term effects.

The regeneration of the nanoparticle catalyst is accompanied by a drop in acetaldehyde production and a corresponding increase in methane production while hydrogen, CO_2, and CO production remain steady. Deactivated rhodium results in the loss of catalytic sites which perform carbon-carbon bond cleavage, so the increase in acetaldehyde suggests that rhodium is being deactivated. However, the stability of carbon monoxide production throughout the test suggests that the nickel is comparatively less vulnerable to deactivation.

XRD of the catalyst samples put on stream for stability tests show that in both cases, impurity phases begin to appear (8-11(d-e)). In the case of M13 templated catalyst, small NiO peaks are seen after a 52 hr run at 450°C and 120000 hr^{-1} GHSV. In the case of the untemplated sample, several more impurity phases appear after two 52 hr runs at 450°C and 120000 hr^{-1} GHSV, corresponding to both NiO and RhO_2. These impurity phases suggest that phase separation plays a significant role in the deactivation of the catalyst over time. In the case of the M13 templated catalyst, the average particle size estimated from XRD peak broadening went from 3.9 nm to 16.5 nm while the untemplated catalyst grew from 4.4 nm to 14.3 nm.

We have shown in this work that in the prototypical ethanol reforming reaction, catalysts formed by biotemplating onto the M13 bacteriophage have significantly different physical properties from catalysts of identical composition formed without the M13 bacteriophage. In particular, the M13 templating process improves long-term stability, reduces vulnerability to surface deactivation, and results in smaller pores with a narrower pore size distribution. Initial performance of both nanoparticles and nanowires were similar, and both nanoparticles and nanowires performed better than catalysts reported in literature to date.
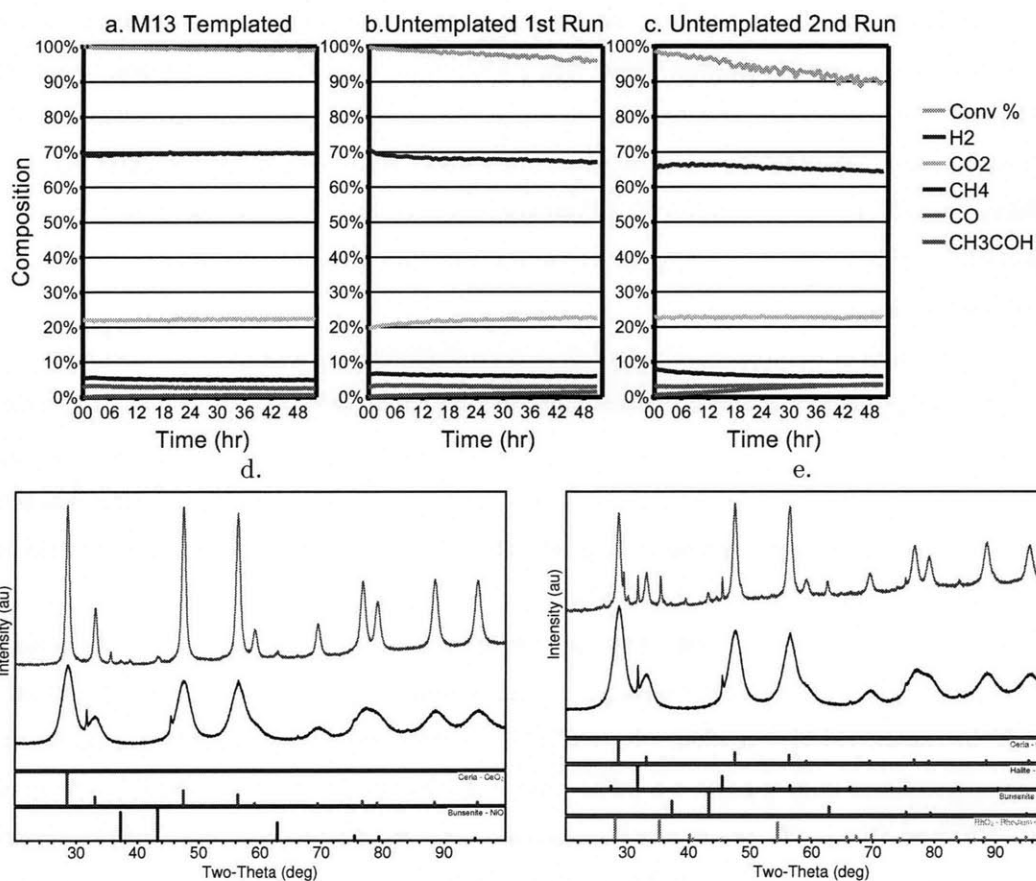
Figure 8-11: Long term deactivation tests at 120000 hr^{-1} and 450°C using 1%Rh-10%Ni@CeO$_2$. (a) With M13 templating, total conversion drops by only 1% over 52 hr. (b) Untemplated catalyst shows total conversion dropping by 4% and decreased hydrogen in the product fraction over 52 hr. (c) Faster deactivation is seen in a second 52 hr test of untemplated catalyst after regeneration under air for 1 hr, with total conversion dropping by 10%. (d) XRD of M13 templated catalyst after 52 hr on stream (top) compared to initial catalyst (bottom). (e) XRD of untemplated catalyst after two 52 hr measurements with 1 hr of regeneration under air (top) compared to initial catalyst (bottom).

Chapter 9

Conclusions and Future Research

In this work, we have shown that in the prototypical reaction of ethanol and water into hydrogen and carbon dioxide, catalyst nanoparticles of rhodium, nickel, and ceria templated onto genetically modified M13 phage via co-precipitation demonstrates excellent overall performance, and specifically demonstrates excellent resistance to deactivation as compared to precipitated nanoparticles without M13.

Both untemplated and M13 templated catalyst particles showed excellent performance at only $300°C$ and some activity at as low as $200°C$. At $300°C$, the catalysts showed 100% conversion, and produced an output stream composed of 60% H_2, less than 0.5% CO, and no acetaldehyde. For comparison, results in literature under similar conditions showed 90+% overall conversion, but with 8-10% CO and 2-7% acetaldehyde. The presence of CO in the output stream of the other reported catalysts makes the new result significantly more attractive for proton exchange membrane fuel cells in particular where CO acts as a poison.

The improved performance over catalysts in literature was present for both untemplated and M13 templated catalysts, suggesting that the majority of the gain in performance is due to improvements in basic materials resulting from the new synthesis methods developed in this work. However, in the critical area of catalyst stability and resistance to deactivation, phage templated catalysts showed clear superiority. Over a 52 hour test, templated catalysts showed no significant deactivation — overall conversion dropped from 100% to 99% over that time period while the product distribution was constant. However, over the same period, untemplated catalysts dropped in overall conversion by 4%, and the relative fraction of hydrogen in the product stream decreased while carbon dioxide and acetaldehyde production increased.

Regeneration of the untemplated catalyst was possible, showing that the deactivation was in part due to surface effects, most likely carbon deposition on the surface. However, regeneration by oxidation in air for one hour followed by a second 52 hour test did not show full recovery.

The second test instead showed a drop in overall conversion of 10% accompanied by a significant increase in acetaldehyde production (5% compared to zero in the templated sample), suggesting that the original deactivation was due to a combination of both surface deactivation and long-term deactivation due to particle growth and migration.

Looking at the product distribution for the stability tests showed also that the deactivation is occuring primarily on the rhodium — regeneration resulted in increased methane production at the expense of acetaldehyde which is characteristic of the regeneration of the capacity of rhodium to break carbon-carbon bonds. It remains unclear exactly why the templated catalyst powders show the ability to prevent rhodium deactivation by surface passivation.

In this work, we also discovered that a wide variety of metal oxide nanocrystals could be formed using our general synthesis methods, and learned that in the case of ceria oxygen vacancies are the driving force prevening particle growth. We learned that the oxygen vacancy concentration continues to increase as particle sizes get extremely small, and showed that the growth inhibition was not due to nitride, chloride, or hydroxide defects on the surface of the crystals.

Overall, this work demonstrates that while the biotemplating of CeO_2 catalysts in order to modify the microstructure, nanostructure, and stability is not necessarily a game-changing improvement on existing techniques for ethanol reforming catalysts, there are clear differences in the structure which may result in even more pronounced improvements in other systems. We recommend that this type of synthesis be adapted to other potential reactions, particularly ones where carbon and other elements commonly found in biological systems are desirable (or not harmful) — for example, in systems using carbide or nitride catalysts. This new technology should also be investigated for applications in areas where catalyst stability and resistance to deactivation, such as environmental catalysts or portable catalytic systems, are critical. Last, the synthetic techniques used to produce extremely small metal oxide nanocrystals should be adopted and used widely to produce more highly active catalysts even without the presence of M13 phage.

Bibliography

[1] Deluga, G. A.; Salge, J. R.; Schmidt, L. D.; Verykios, X. E. *Science* **2004**, *303*, 993.

[2] Kugai, J.; Subramani, V.; Song, C.; Engelhard, M. H.; Chin, Y.-H. *Journal of Catalysis* **2006**, *238*, 430-440.

[3] Deshpande, S.; Patil, S.; Kuchibhatla, S. V. N. T.; Seal, S. *Applied Physics Letters* **2005**, *87*, 133113.

[4] Zhang, F.; Wang, P.; Koberstein, J.; Khalid, S.; Chan, S. W. *Surface Science* **2004**, *563*, 74-82.

[5] US Department of Energy Hydrogen Program, "Comparison of Fuel Cell Technologies", Technical Report, US Department of Energy Hydrogen Program, 2008.

[6] Lide, D. R., Ed.; *CRC Handbook of Chemistry and Physics*; CRC Press: 90 ed.; 2010.

[7] Salge, J. R.; Deluga, G. A.; Schmidt, L. D. *Journal of Catalysis* **2005**, *235*, 69-78.

[8] Zerva, C.; Philippopoulos, C. J. *Applied Catalysis B: Environmental* **2006**, *67*, 105-112.

[9] Idriss, H. *Platinum Metals Rev* **2004**, *48*, 105-115.

[10] Sheng, P.-Y.; Yee, A.; Bowmaker, G. A.; Idriss, H. *Journal of Catalysis* **2002**, *208*, 393-403.

[11] Erdohelyi, A.; Rasko, J.; Kecskes, T.; Toth, M.; Domok, M.; Baan, K. *Catalysis Today* **2006**, *116*, 367-376.

[12] Kugai, J.; Velu, S.; Song, C. *Catalysis Letters* **2005**, *101*, 255.

[13] Llorca, J.; Homs, N.; Sales, J.; de la Piscina, P. R. *Journal of Catalysis* **2002**, *209*, 306-317.

[14] de Lima, S. M.; Colman, R.; Jacobs, G.; Davis, B. H.; Souza, K. R.; de Lima, A. F. F.; Appel, L. G.; Mattos, L. V.; Noronha, F. B. *Catalysis Today* **2009**, *146*, 110-123.

[15] Cai, W.; Wang, F.; Zhan, E.; Veen, A. C. V.; Mirodatos, C.; Shen, W. *Journal of Catalysis* **2008**, *257*, 96-107.

[16] Sheng, P. Y.; Chiu, W. W.; Yee, A.; Morrison, S. J.; Idriss, H. *Prepr. Pap.-Am. Chem. Soc., Div. Petr. Chem.* **2006,** *51,* 26.

[17] Wang, H.; Ye, J. L.; Liu, Y.; Li, Y. D.; Qin, Y. N. *Catalysis Today* **2007,** *129,* 305-312.

[18] Pereira, E. B.; Homs, N.; Marti, S.; Fierro, J. L. G.; de la Piscina, P. R. *Journal of Catalysis* **2008,** *257,* 206-214.

[19] Srisiriwat, N.; Therdthianwong, S.; Therdthianwong, A. *International Journal of Hydrogen Energy* **2009,** *34,* 2224-2234.

[20] Iulianelli, A.; Longo, T.; Liguori, S.; Seelam, P. K.; Keiski, R. L.; Basile, A. *International Journal of Hydrogen Energy* **2009,** *34,* 8558-8565.

[21] de Lima, S. M.; da Cruz, I. O.; Jacobs, G.; Davis, B. H.; Mattos, L. V.; Noronha, F. B. *Journal of Catalysis* **2008,** *257,* 356-368.

[22] de Lima, S. M.; da Silva, A. M.; da Costa, L. O. O.; Graham, U. M.; Jacobs, G.; Davis, B. H.; Mattos, L. V.; Noronha, F. B. *Journal of Catalysis* **2009,** *268,* 268-281.

[23] Youn, M. H.; Seo, J. G.; Cho, K. M.; Park, S.; Park, D. R.; Jung, J. C.; Song, I. K. *International Journal of Hydrogen Energy* **2008,** *33,* 5052-5059.

[24] Cai, W.; Wang, F.; Veen, A. C. V.; Provendier, H.; Mirodatos, C.; Shen, W. *Catalysis Today* **2008,** *138,* 152-156.

[25] Biswas, P.; Kunzru, D. *Chemical Engineering Journal* **2007,** *136,* 41-49.

[26] Biswas, P.; Kunzru, D. *Catalysis Letters* **2007,** *118,* 36.

[27] Pimentel, *Encyclopedia of Physical Sciences and Technology* 159-171.

[28] Energy Information Administration, "Production and end-use data, 2002", Technical Report, Energy Information Administration, 2002.

[29] Bourne, J.; Clark, R. *National Geographic Magazine* **2007,** 41.

[30] Chisti, Y. *Biotechnology Advances* **2007,** *25,* 294-306.

[31] noz, R. M.; Guieysse, B. *Water Research* **2006,** *40,* 2799-2815.

[32] Haag, A. L. *Nature* **2007,** *447,* 520-521.

[33] Gross, M. *Current Biology 18,* R46.

[34] Houtman, C. J.; Barteau, M. A. *Journal of Catalysis* **1991,** *130,* 528-546.

[35] Yee, A.; Morrison, S. J.; Idriss, H. *Catalysis Today* **2000,** *63,* 327-335.

[36] Wheeler, C.; Jhalani, A.; Klein, E. J.; Tummala, S.; Schmidt, L. D. *Journal of Catalysis* **2004,** *223,* 191-199.

[37] Esch, F.; Fabris, S.; Zhou, L.; Montini, T.; Africh, C.; Fornasiero, P.; Comelli, G.; Rosei, R. *Science* **2005,** *309,* 752.

[38] Trovarelli, A., Ed.; *Catalysis by Ceria and Related Materials;* Imperial College Press: 2002.

[39] Fu, Q.; Saltsburg, H.; Flytzani-Stepanopoulos, M. *Science* **2003,** *301,* 935.

[40] Liu, Z.; Jenkins, S.; King, D. *Physical Review Letters* **2005,** *94,* 196102.

[41] Fuchs, M.; Jenewein, B.; Penner, S.; Hayek, K.; Rupprechter, G.; Wang, D.; Schlogl, R.; Calvino, J. J.; Bernal, S. *Applied Catalysis A: General* **2005,** *294,* 279-289.

[42] Hirta, Y.; Harada, A.; Wang, X. *Ceramics International* **2005,** *31,* 1007-1013.

[43] Dutta, P.; Pal, S.; Seehra, M. S.; Shi, Y.; Eyring, E. M.; Ernst, R. D. *American Chemical Society* **2006,** *18,* 5144-5146.

[44] Romeo, M.; Bak, K.; Fallah, J. E.; Lenormand, F.; Hilaire, L. *Surface and Interface Analysis* **1992,** *20,* 508-512.

[45] Mullins, D. R.; Overbury, S. H.; Huntley, D. R. *Surface Science* **1998,** *409,* 307-319.

[46] Masui, T.; Fujiware, K.; Machida, K.; Adachi, G.; Sakata, T.; Mori, H. *Chem. Mater.* **1997,** *9,* 2197-2204.

[47] Hirano, M.; Kato, E. *J. Am. Ceram. Soc.* **1996,** *79,* 777-780.

[48] Yu, X.; Li, F.; Ye, X.; Xin, X. Q.; Xue, Z. L. *J. Am. Ceram. Soc.* **1999,** *83,* 964.

[49] Chen, P.; Chen, I. *J. Am. Ceram. Soc.* **1992,** *76,* 1577-1583.

[50] Sato, T.; Katakura, T.; Yin, S.; Fujimoto, T.; Yabe, S. *Solid State Ionics* **2004,** *172,* 377-382.

[51] Bodke, A. S.; Bharadwaj, S. S.; Schmidt, L. D. *Journal of Catalysis* **1998,** *179,* 138-149.

[52] Yamashita, M.; Kameyama, K.; Yabe, S.; Yoshida, S.; Fujishiro, Y.; Kawai, T.; Sato, T. *Journal of Materials Science* **2001,** *37,* 683-687.

[53] Nam, K. T.; Kim, D.-W.; Yoo, P. J.; Chiang, C. Y.; Meethong, N.; Hammond, P. T.; Chiang, Y. M.; Belcher, A. M. *Science* **2006,** *312,* 885.

[54] Mao, C.; Solis, D.; Reiss, B.; Kottmann, S. T.; Sweeney, R. Y.; Hayhurst, A.; Georgiou, G.; Iverson, B.; Belcher, A. M. *Science* **2004**, *303*, 213-217.

[55] Regalbuto, J., Ed.; *Catalyst Preparation Science and Engineering;* CRC Press: 2007.

[56] Holgado, J.; Alvarez, R.; Munuera, G. *Applied Surface Science* **2000**, *161*, 301-315.

[57] Trudeau, M.; Tschöpe, A.; Ying, J. *Surface and Interface Analysis* **1995**, *23*, 219-226.

[58] Ratke, L.; Voorhees, P. W. *Growth and coarsening: Ostwald ripening in material processing.;* Springer: 2002.

[59] Balluffi, R.; Allen, S.; Carter, C. *Kinetics of Materials;* John Wiley & Sons: 2005.

[60] Bluthardt, C.; Fink, C.; Flick, K.; Hagemeyer, A.; Schlichter, M.; Volpe, A. *Catalysis Today* **2008**, *137*, 132-143.

[61] Oskam, G. *J Sol-Gel Sci Techn* **2006**, *37*, 161-164.

[62] Jolivet, J.; Cassaignon, S.; Chanéac, C.; Chiche, D.; Tronc, E. *J Sol-Gel Sci Technol* **2008**, *46*, 299-305.

[63] Djerdj, I.; Arcon, D.; Jaglicic, Z.; Neiderberger, M. *Journal of Solid State Chemistry* **2008**, *181*, 1571-1581.

[64] Chaudret, B. *C.R. Physique* **2005**, *6*, 117-131.

[65] Niederberger, M.; Garnweitner, G. *Chem. Eur. J.* **2006**, *12*, 7282-7302.

[66] Ganguli, A.; Ahmad, T.; Vaidya, S.; Ahmed, J. *Pure and Applied Chemistry* **2008**, *80*, 2451-2477.

[67] Kim, D. Y.; Ju, S. H.; Koo, H. Y.; Hong, S. K.; Kang, Y. C. *Journal of Alloys and Compounds* **2006**, *417*, 254-258.

[68] Kim, J. H.; Hong, Y. C.; Uhm, H. S. *Surface & Coatings Technology* **2007**, *201*, 5114-5120.

[69] Liu, T.; Zhang, Y.; Shao, H.; Li, X. G. *Langmuir* **2003**, *19*, 7569-7572.

[70] Adschiri, T.; Hakuta, Y.; Sue, K.; Arai, K. *Journal of Nanoparticle Research* **2001**, *3*, 227-235.

[71] Neltner, B.; Speakman, S.; Belcher, A. *TBD* **2010**, .

[72] Wang, H.; Liu, Y.; Wang, L.; Qin, Y. N. *Chemical Engineering Journal* **2008**, *145*, 25-31.